"Generation of morphologically distinct astrocyte subtypes from human iPSCs reveals a link between glial shape, function and reactivity"

*Kelly O'Toole[1,2,3,+], Ludovica Guetta[1,2,3,+], Paulina Urbanaviciute[1,2], Pacharaporn Suklai[1,2,3], Chandler Wright[4], Theodore Fisher[4], Shane Liddelow[4-7], Raphaelle Luisier[8,9], Sarah J Marzi[1,2], Andrea Serio[1,2,3]**

1. Department of Basic and Clinical Neuroscience, Institute of Psychiatry Psychology & Neuroscience, King's College London, London, United Kingdom.

2. UK Dementia Research Institute at King's College London, London, United Kingdom.

3. The Francis Crick Institute, London (UK)

4. Neuroscience Institute, NYU Grossman School of Medicine, New York, USA

5. Department of Neuroscience and Physiology, NYU Grossman School of Medicine, New York, USA

6. Department of Ophthalmology, NYU Grossman School of Medicine, New York, USA

7. Parekh Center for Interdisciplinary Neurology, NYU Grossman School of Medicine, New York, USA

8. Idiap Research Institute, Martigny, Switzerland,

9. SIB Swiss Institute of Bioinformatics, Lausanne, Switzerland

+ = these authors have contributed equally and are here listed in chronological order based on their contributions.

* = corresponding author (andrea.serio@kcl.ac.uk / andrea.serio@crick.ac.uk)

Keywords: astrocytes, glial cell biology, cellular shape, *in vitro* modelling, iPSCs

CRediT (Contributor Roles Taxonomy) Statement

Kelly O'Toole: conceptualization, methodology, validation, formal analysis, investigation, visualization, writing – review & editing.

Ludovica Guetta: conceptualization, methodology, validation, formal analysis, investigation, writing-original draft, writing – review & editing, visualization.

Paulina Urbanaviciute: software, formal analysis, data curation, visualization, writing – review & editing.
Pacharaporn Suklai: validation, investigation, formal analysis, visualization.
Chandler Wright: validation, formal analysis, investigation, writing – review & editing.
Theodore Fisher: validation, formal analysis, investigation, writing – review & editing.
Shane Liddelow: conceptualization, supervision, funding acquisition, validation, writing – review & editing.
Raphaelle Luisier: software, formal analysis, data curation, visualization, writing – review & editing.
Sarah J Marzi: software, formal analysis, data curation, visualization, writing – review & editing.
Andrea Serio: conceptualization, writing-original draft, writing – review & editing, supervision, project administration, visualization, funding acquisition.

Abstract

Astrocyte morphology *in vivo* is heterogeneous across different subtypes and dynamically changes in response to various stimuli. However, several questions on the mechanistic links between shape and function remain unanswered. Here, we developed an efficient protocol to generate pure populations of morphologically distinct human astrocytes *in vitro*, which we used for a systematic analysis of shape-function relationships. We performed a structural, molecular, and functional characterization of these populations and highlighted how their distinct morphologies mirror distinct functional and transcriptional patterns at the population level. We were also able to both correlate gene expression profiles of these morphologically distinct astrocyte subtypes with *in vivo* astrocytes in the human brain, and to validate our findings with primary isolated murine astrocytes in vitro. Moreover, we show that the observed morphological differences are correlated with changes in key cytoskeletal proteins, which offers a potential link to the observed functional differences. Finally, we demonstrated that different morphological subtypes of astrocytes have distinct reactivity responses to a common stimulus. This study offers a glimpse into the shape-function dynamics of human astrocytes, highlighting potential mechanistic links between cytoskeletal usage and astrocyte function, while also providing tools and datasets that will be useful for further studies into human glial biology in health and disease.

Introduction

Every cell is configured to acquire an optimal shape which is tailored to its specific function and tasks within an organism or tissue. This, in turn, can influence cellular metabolism and homeostasis. This link between shape and function is a fundamental aspect of cellular biology[1–3], and has profound implications in our understanding of pathological mechanisms[4]. Moreover, this is a dynamic relationship, as morphology can change not only across cell types, but also over space and time; different subtypes of the same cell populations can vary widely depending on their regional specification, like neurons and muscle cells, and their shape can change significantly in response to different stimuli and conditions[5,6].

Astrocytes[7,8] have a highly ramified morphology, that changes across each regional and functional subtype[7–10]. These glial cells play a crucial role in the development and function of the central nervous system (CNS)[11], and their diversity of form allows them to perform a plethora of key functions: tiling the brain and spinal cord in vast astrocytic networks, contacting other cell types, sensing and responding to their local microenvironment, and even acting as master regulators of metabolism for the brain and spinal cord[9,10]. The complexity of astrocyte morphology dynamically responds to injury, inflammation, and various neurological disorders[1213]something wrong with this ref. The observed correlations between altered astrocyte shape and pathological processes and the mechanisms underlying astrocyte shape changes in neurodegenerative disorders remain poorly understood.

Recent advances in induced pluripotent stem cell (iPSC) reprogramming[14], *in vitro* differentiation and screening [15], sequencing[16], and organoids[17] have provided a plethora of ways to more accurately model human astrocytes in health and disease. These improvements have been critical for understanding the pathogenesis of various neurodegenerative disorders[18–20]. However, lots of unanswered questions remain on how astrocyte morphology is determined, as *in vitro* astrocytes often lack the distinctive complexity of their *in vivo* counterparts[21], and in some protocols the cultures present high morphological variability[22]. Some of these limitations are partly due to the low efficiency of astrocyte differentiation protocols, which often use undefined factors (e.g. serum), or mixes of cytokines and growth factors with diverging effects (e.g. epidermal growth factor [EGF], fibroblastic growth factor-2 [FGF2], bone morphogenic [BMP4], ciliary neurotrophic factor [CNTF]).

In response to these challenges, we developed a highly efficient, chemically defined protocol to generate pure populations of functional astrocytes from human iPSC cultures, in a reliable and scalable manner. Our approach uses a minimal set of cytokines, optimised to generate distinct morphological subtypes of astrocytes *in vitro*. This system allowed us to obtain pure populations of human astrocytes with distinct morphologies, which we characterised at the

population, cellular, and subcellular level, demonstrating that morphology correlates with subtle differences in functionality, as well as distinct transcriptional profiles.

These insights will be key to both enhance our understanding of mechanisms underlying astrocyte functionality and better model disease *in vitro*.

Results

BMP4 and CNTF based differentiation produces human astrocytes with distinct morphologies

To investigate the links between morphology and function in human astrocytes we first sought to establish a reproducible protocol that would generate astrocytes with distinct morphologies in a controlled fashion, starting from common glial progenitors.

We adapted a previously developed protocol to derive progenitor cells committed to the astrocytic fate (astrocyte progenitor cells, APCs) starting from iPSC populations[19]. (**Figure 1A**). These APCs are derived in completely defined conditions and can be propagated as homogeneous monolayers for several passages in a combination of FGF2 and EGF (**Figure 1B**), offering an ideal system for large scale studies. These astrocyte progenitors express *NES* (Nestin) and *NF1A*[23,24] (**Figure 1B**), and importantly, once expanded, can be differentiated into high purity (>95%) astrocytes that retain important astrocyte functions (e.g. glutamate uptake, ability to support synaptogenesis). These and have already been employed to assess different disease phenotypes[19], demonstrating that they can mimic several aspects of astrocyte biology. Using this system, we initially aimed to test whether exposing the same population of iPSC-derived APCs to known astrogenic factors might produce morphologically distinct terminally differentiated astrocytes. Based on previous evidence from both *ex vivo*[25,26] and mouse in vitro models[16] , we selected BMP4 and CNTF as potential “polarizing” factors for astrocyte morphology.

We adapted the established protocol[19] to include a differentiation with medium supplemented with either BMP4 or CNTF for two weeks (**Figure 1A**). We found that both protocols produce non-proliferative (**Figure S1A and S1B**) cells that are immunoreactive for key astrocytic markers, such as Aldh1l1 and S100β[27,28] (**Figure 1C**). However, the resultant populations of astrocytes have distinct morphologies which are homogeneous within each population. Specifically, BMP4-differentiated astrocytes display larger and more spread-out cell bodies with a rounder shape compared to CNTF-differentiated astrocytes, which are characterized by small cell bodies with long thin processes (**Figure 1C**).

To better quantify these morphological differences and define the timescale of development of astrocyte morphology, we performed high content live imaging of astrocyte progenitors

134 sparsely transfected with GFP under the *EEF1A1* promoter at different timepoints (Days 0, 1,
135 7, 14, and 21) during the differentiation process. We compared astrocytes differentiated with
136 BMP4, CNTF, both cytokines together, or base medium devoid of any cytokine (**Figure 1D**).
137 To assess the morphological heterogeneity across these conditions in an unbiased manner,
138 we established a computational pipeline for semi-automated single-cell profiling based on
139 discrete morphological features over the time-course of terminal differentiation. We first
140 applied singular value decomposition (SVD) to the matrix of single-cell measurements (52
141 measurements across 5,376 cells) to identify major orthogonal temporal dynamics of
142 morphological changes associated with terminal differentiation of astrocytes exposed to
143 different cytokines[29]. Our analysis reveals that the first 20 components capture 90% of the
144 variance in the data (**Figure 1E**). Using linear mixed modelling, we found significant
145 associations between principal component (PC) 1 (41% of variance), PC2 (6.4% of variance),
146 and PC5 (4% of variance) with the different cytokine combinations over time (**Figure 1F)**.
147 Notably, our results indicate that exposure to BMP4, irrespective of CNTF treatment, leads to
148 diverging differentiation trajectories. In contrast, astrocytes cultured with CNTF or basal
149 medium show similar progressive changes over time, with the exception of a notable
150 difference observed at day 21. Further analysis of the morphological parameters most
151 contributing and correlating with PC1, PC2, and PC5 revealed that measurements describing
152 rounder and more extended morphologies (e.g., median radius and extent) most positively
153 contribute to PC1, whereas measurements such as cell perimeter and compactness, which
154 describe more complex, ramified morphologies, most contribute negatively to PC1 (**Figure**
155 **S1C**). This indicates that the terminal differentiation of astrocytes in the absence of BMP4
156 leads to a progressive reduction in roundness and extent, along with a progressive increase
157 in ramification (**Figure 1G)**.

158 To evaluate the difference in morphology between BMP4 and CNTF, we selected median
159 radius and perimeter (**Figure 1G and S1D**) which show opposite direction of change. The
160 cells treated with BMP4 or with the combination of both cytokines show a gradual increase in
161 median radius over three weeks of differentiation, but no change in perimeter – suggesting an
162 overall simplification of morphology with time. Conversely, CNTF and basal medium astrocytes
163 show an increase in their perimeter as they differentiate but no appreciable in median radius
164 – suggesting a switch to a more complex cell morphology (**Figure S1D**).

165 Overall, this demonstrates that BMP4 and CNTF specifically influence human astrocyte
166 morphology *in vitro* producing homogeneous populations with opposing cell shapes. In
167 addition, we show that the effect of BMP4 can overpower that of CNTF suggesting it is a
168 stronger morphogen (**Figure 1E-F and S1D**), while addition of CNTF maintains a base non-
169 divergent morphological differentiation as astrocytes supplemented with CNTF mimic those

170 grown in basal differentiation medium alone, with the exception of slight differences in cell
171 body shape (**Figure S1E-F**).

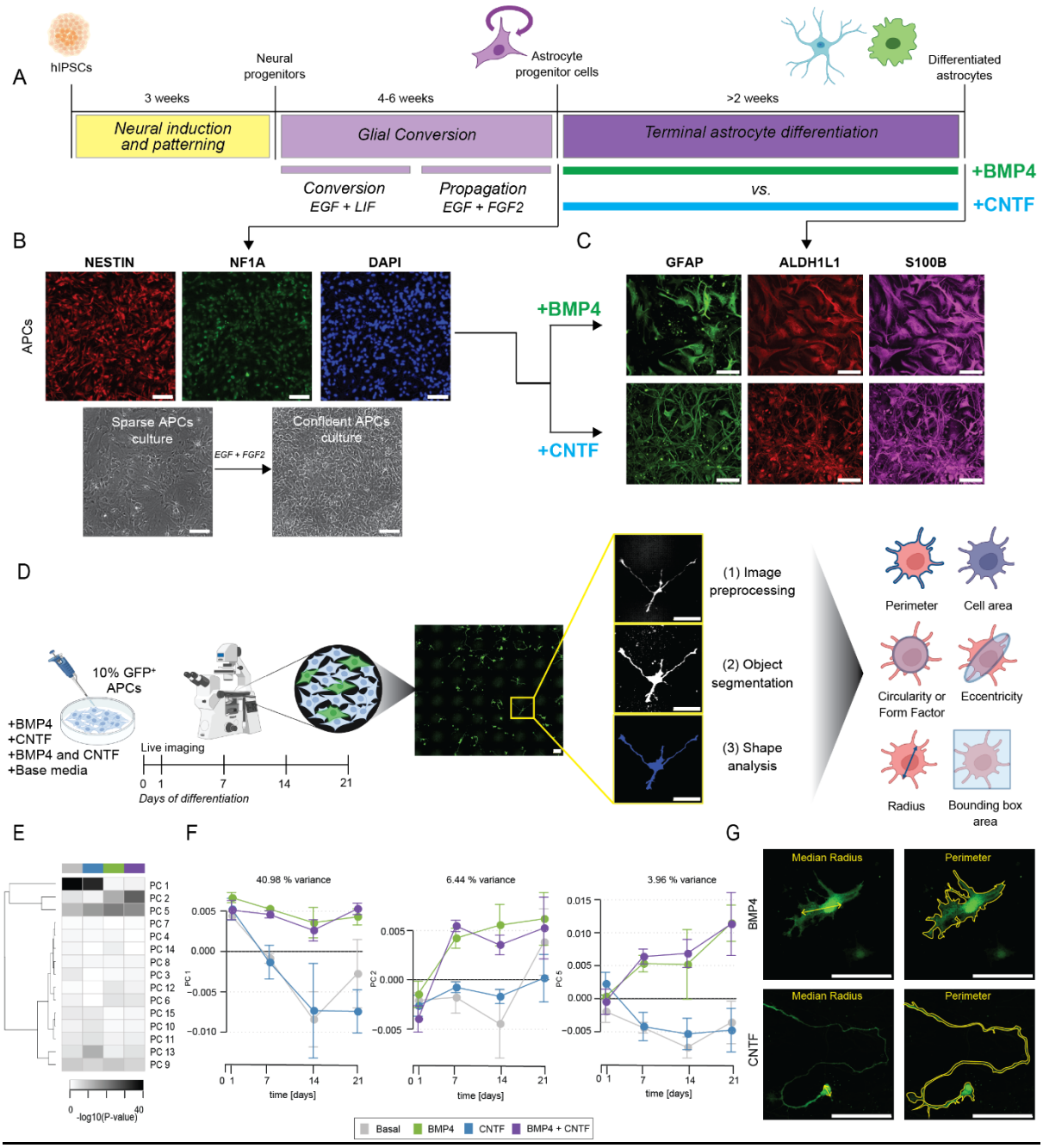

172

173 ***Figure 1 – BMP4 and CNTF produce human astrocyte subtypes with distinct***
174 ***morphologies.*** *A) Schematic overview of the protocols for the generation of human iPSC-*
175 *derived astrocytes terminally differentiated with BMP4 or CNTF. Astrocyte progenitors are*
176 *generated and propagated as previously described (Serio et al, 2013) and then terminally*
177 *differentiated for two weeks in the presence of BMP4 or CNTF. B) Representative images of*
178 *astrocyte progenitors stained for NESTIN, NF1A and nuclei (DAPI) and brightfield pictures*
179 *showing sparse and confluent progenitor cultures. Scale bar: 100 µm. C) Representative*
180 *images of differentiated BMP4 and CNTF astrocytes stained for astrocytic markers GFAP,*
181 *ALDH1L1 and S100β. Scale bar: 100 µm. D) Pipeline for the analysis of astrocyte*
182 *morphological characteristics. Astrocyte progenitor cells (APCs) are sparsely transfected with*

*green fluorescent protein (GFP) under the EEF1A1 promoter, differentiated with BMP4, CNTF, base media or a combination of cytokines and then imaged live over differentiation. The images acquired are pre-processed, followed by object segmentation using pixel classification. Morphometric analysis is then performed on these objects to obtain key morphometric parameters. Scale bar: 50 µm. E) Principal component analysis of astrocyte morphological variations. The principal components cluster with unsupervised hierarchal clustering according to cytokine groups. F) Representation of the top 3 principal components (PC1, PC2, PC5) which explain over 50% of the variance and fluctuate over the days of differentiation for the different cytokine groups. Data represents averages of wells from 1 control line in 1 experimental block, with 7 technical replicates (n=7 wells). G) Graphical representations (yellow) of shape descriptors, median radius, and perimeter, superimposed onto BMP4 and CNTF GFP$^+$ astrocytes. Scale bar: 100 µm.*Astrocyte shape is committed during the initial phases of differentiation

We next sought to investigate whether the distinct morphological phenotypes obtained with BMP4 and CNTF are the result of the commitment to a specific developmental program, and therefore stable once acquired, or plastic and changing based on a constant supply of cytokines.

We therefore performed medium switch experiments (**Figure 2A**), in which we first swapped 2-week differentiated astrocytes to the opposite cytokine regimen for an additional week of differentiation, to test whether this would alter their final morphology to resemble that of the opposite subtype. We found that cytokine switching did not correlate with a switch of morphologies between the two subtypes, with BMP4 astrocytes showing no significant alteration in any of the shape descriptors we evaluated. While CNTF astrocytes showed minimal changes in median radius and compactness compared to their non-switched counterpart, this did not alter the overall architecture of the cells, nor induce them to adopt the same morphology as BMP4 astrocytes (**Figure 2B**). These results suggest that astrocytes in our model commit to a specific morphology by two weeks of differentiation, albeit with the potential of morphological malleability at earlier timepoints through exposure to different cytokines.

To test this hypothesis, we repeated the medium-switching experiment after one week of differentiation. BMP4 astrocytes switched to CNTF medium showed no significant differences from non-switched BMP4 controls, while CNTF astrocytes switched to BMP4 exhibited increased extent and reduced compactness (**Figure 2C**). Qualitatively, it seems that Qualitative assessment suggests that these differences primarily result from to the reduced process length observed in comparison to non-switched CNTF (**Figure 2D**). These alterations impact overall perimeter and associated descriptors without altering the global architecture, defined by a smaller cell body and elongated, thin processes.

These experiments indicate that the contrasting morphologies of BMP4 and CNTF astrocytes, characterised by opposing extent and perimeter (i.e. high extent/low perimeter for BMP4 and low extent/high perimeter for CNTF), are largely committed established after 1-week of differentiation. While minor adjustments can be made, each subtype broadly maintains its morphology irrespective of culture conditions (**Figure 2E**). Notably, BMP4 appears to exert a dominant effect, consistent with observations from astrocytes differentiating in the presence of both cytokines (**Figure 1E-F and S1D**).

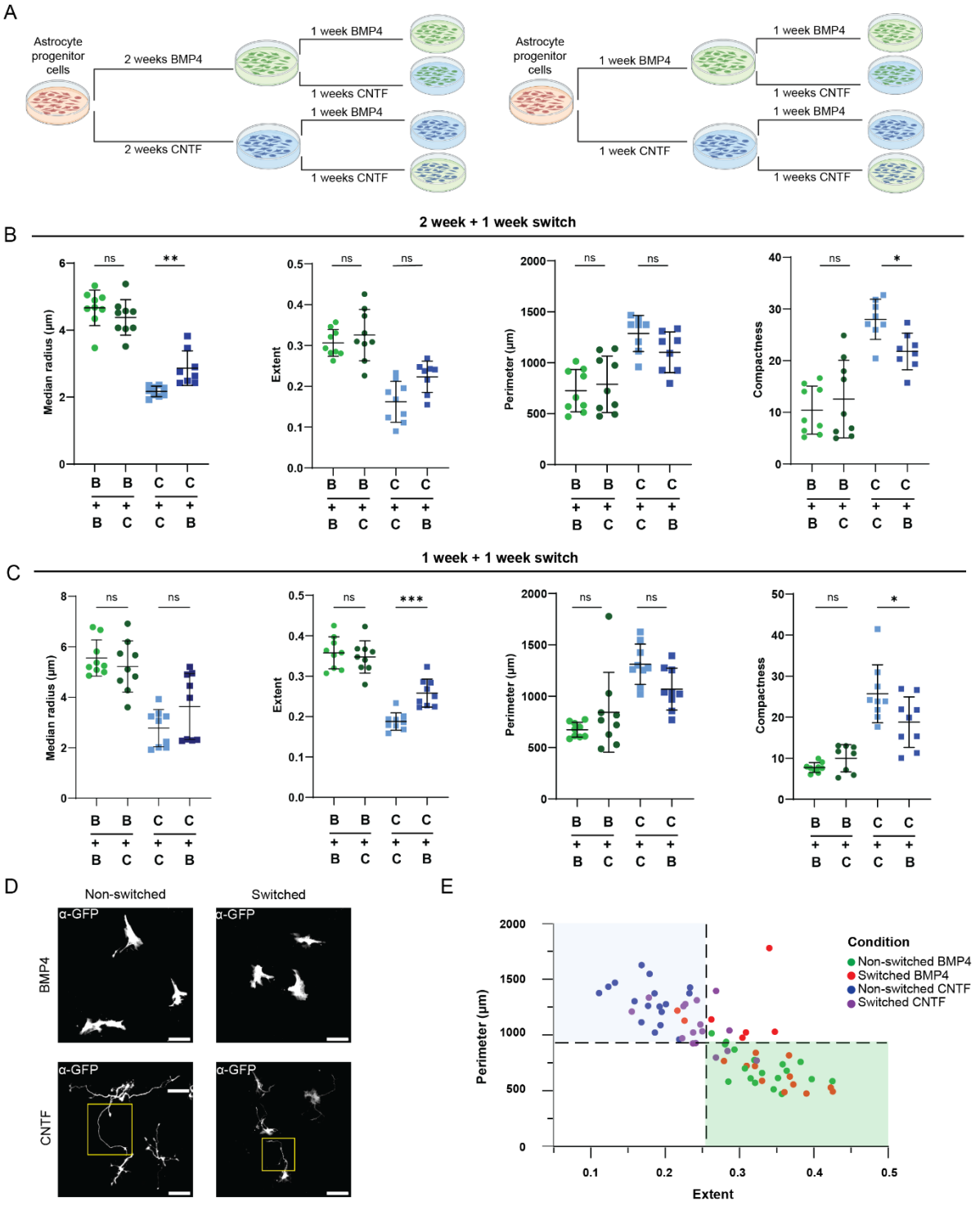

229 ***Figure 2 – Astrocyte morphology is largely committed during the first week of***
230 ***differentiation.*** *A) Schematic overview of the experimental set up for cytokine switching*
231 *experiments, with astrocytes differentiating for 1 or 2 weeks with BMP4 switched to CNTF and*
232 *astrocytes differentiating for 1 or 2 weeks with CNTF switched to BMP4, in all cases for one*
233 *additional week. B-C) Quantification of morphological differences between BMP4 and CNTF*
234 *GFP$^+$ astrocytes differentiated for either 2 weeks (B) or 1 week (C) with one cytokine and then*
235 *'switched' (B+C or C+B) or 'non-switched' (B+B or C+C). One-way ANOVA or Kruskall-Wallis*
236 *test with Dunn's multiple comparisons to test for significance between switched and non-*
237 *switched pairs. Data represents technical replicate well averages of astrocytes from 2 control*
238 *lines from 2 independent experiment blocks (n=7-9 wells) mean ± SD. ****p<0.0001,*
239 *****p<0.001, **p<0.01, *p<0.05, ns: non-significant. B+B: BMP4 + BMP4; B+C: BMP4 + CNTF;*
240 *C+C: CNTF+CNTF; C+B: CNTF+BMP4. D) Representative fluorescent images (20x) of non-*
241 *switched BMP4 (B+B) and switched BMP4 (B+C) astrocytes, and non-switched CNTF (C+C)*
242 *and switched CNTF (C+B) astrocytes. Inset in CNTF panels highlights the process length*
243 *differences between non-switched and switched CNTF astrocytes. Scale bar: 100µm. E) 2D*
244 *scatter plot of perimeter versus extent to visualise the correlation between these two shape*
245 *descriptors, with the data points representing well averages of BMP4 and CNTF non-switched*
246 *versus switched astrocytes. The dotted line on the y-axis is the median of control non-switched*
247 *CNTF astrocytes and the dotted line on the x-axis is the median of control non- switched BMP4*
248 *astrocytes. The top left quadrant contains cells with a 'CNTF' phenotype, and the bottom right*
249 *quadrant contains cells with a 'BMP4' phenotype. Data points represent well averages of 2*
250 *control lines across 4 experimental blocks, from both switching experiments.*

251

252 *BMP4 and CNTF astrocytes show distinct homeostatic capabilities*

253 We next sought to determine whether the distinct morphologies of CNTF and BMP4 astrocytes
254 also translate into distinct functional properties.

255 Calcium signalling via intercellular calcium waves (ICWs) is key in regulating astrocytic
256 network-level communication[30], as well as modulating interactions with neurons[31]. As ICWs
257 rely on calcium microdomains within astrocytic processes for propagation[32,33], we
258 hypothesized that the difference in morphology between BMP4 and CNTF astrocytes may
259 also correlated with different calcium wave dynamics. To test this, we stimulated BMP4 and
260 CNTF astrocyte populations with adenosine triphosphate (ATP; 5mM) and used Fluo-4AM
261 calcium dye to visualize the calcium signalling response over a period of 160 seconds (**Figure**
262 **S3A**). CNTF astrocytes responded more swiftly to ATP administration compared to BMP4,
263 during imaging (**Figure 3A**), indicating different kinetics associated with the two subtypes,
264 which we confirmed by peak analysis (**Figure 3B**). Following ATP stimulation, CNTF
265 astrocytes exhibited a significantly shorter time to peak, whereas BMP4 astrocytes displayed
266 significantly higher and broader peak responses (**Figure 3C**). This indicates that, while BMP4
267 astrocytes are slower in responding, they show a higher and sustained concentration of
268 calcium within the cell during the spiking activity. Interestingly, this difference in ICW kinetics

269 does appears independent of Connexin-43 protein levels, which are comparable between the
270 two astrocyte populations (**Figure 3D** and **S3B**). However, one possible explanation that we
271 cannot exclude is that CNTF astrocytes might simply respond faster to the bath application of
272 ATP, independently of connexin-based propagation.

273 Glutamate reuptake is another key homeostatic function of astrocytes and is considered a
274 hallmark for the characterization of differentiated astrocytes *in vitro*[34]. To test whether our two
275 astrocyte subtypes differed in their glutamate reuptake ability, we employed a fluorometric
276 glutamate uptake assay that measures the depletion of glutamate from the culture medium
277 over time, starting from a known concentration (100 μM) (**Figure 3E**). We used a selective
278 glutamate transport inhibitor L-trans-pyrrolidine-2,4-dicarboxylate (PDC)[35] as a negative
279 control. We observed that, while both BMP4 and CNTF astrocytes are capable of glutamate
280 uptake, the rate is twice as high for CNTF astrocytes than for astrocytes differentiated with
281 BMP4 (c.a. 33 μM/hr and 15μM/hr, respectively) (**Figure 3E**). This difference also corresponds
282 to differences in protein levels of the glutamate transporter excitatory amino acid transporter
283 1 (EAAT1), which are significantly higher in CNTF astrocytes (**Figure 3F**).

284

285 *BMP and CNTF differentiated astrocyte morphologies are not altered by neuron contact*

286 Astrocytes have a bidirectional relationship with neurons *in vivo*, which is known to influence
287 the morphology, homeostasis, and function of both cell types[36,37]. For this reason, we
288 investigated the morphologies and functional properties of both BMP4 and CNTF astrocytes
289 when co-cultured with neurons. First, we wanted to test whether their morphology would be
290 altered by the presence of neurons, using our established imaging pipeline with GFP^+ BMP4
291 and CNTF astrocytes. When co-cultured with neurons[38], CNTF and BMP4 astrocytes
292 displayed subtle morphological differences (not reflected in previously defined parameters)
293 but retained their distinct base cell shapes (**Figure S3C, Figure 3G**). Importantly, co-culture
294 with neurons significantly upregulated excitatory amino acid transporter 2 (EAAT2) levels in
295 both BMP- and CNTF-differentiated astrocytes compared to monoculture (**Figure S3D**),
296 suggesting that both these distinct subtypes can respond productively to neurons.

297 Astrocytes also have a key role in promoting neuronal synapse formation[39,40]. We therefore
298 tested whether BMP4 and CNTF astrocytes differ in their ability to stimulate synaptogenesis
299 when co-cultured with neurons. To do this we differentiated cortical neuron progenitors[38],
300 either alone or in the presence of BMP4 or CNTF differentiated astrocytes. To assess the co-
301 localization of synapses, we stained for re- and post-synaptic proteins synaptophysin (SYN)
302 and post-synaptic density-95 (PSD95), along with MAP2 to demarcate dendrites (**Figure**
303 **S3E**), and quantified the number of $SYN^+/PSD95^+$ puncta per $100\mu m^2$ of MAP2 dendrites. Our

results indicate that BMP4 and CNTF astrocytes both significantly promote synaptogenesis to a similar extent within our system (**Figure 3H**).

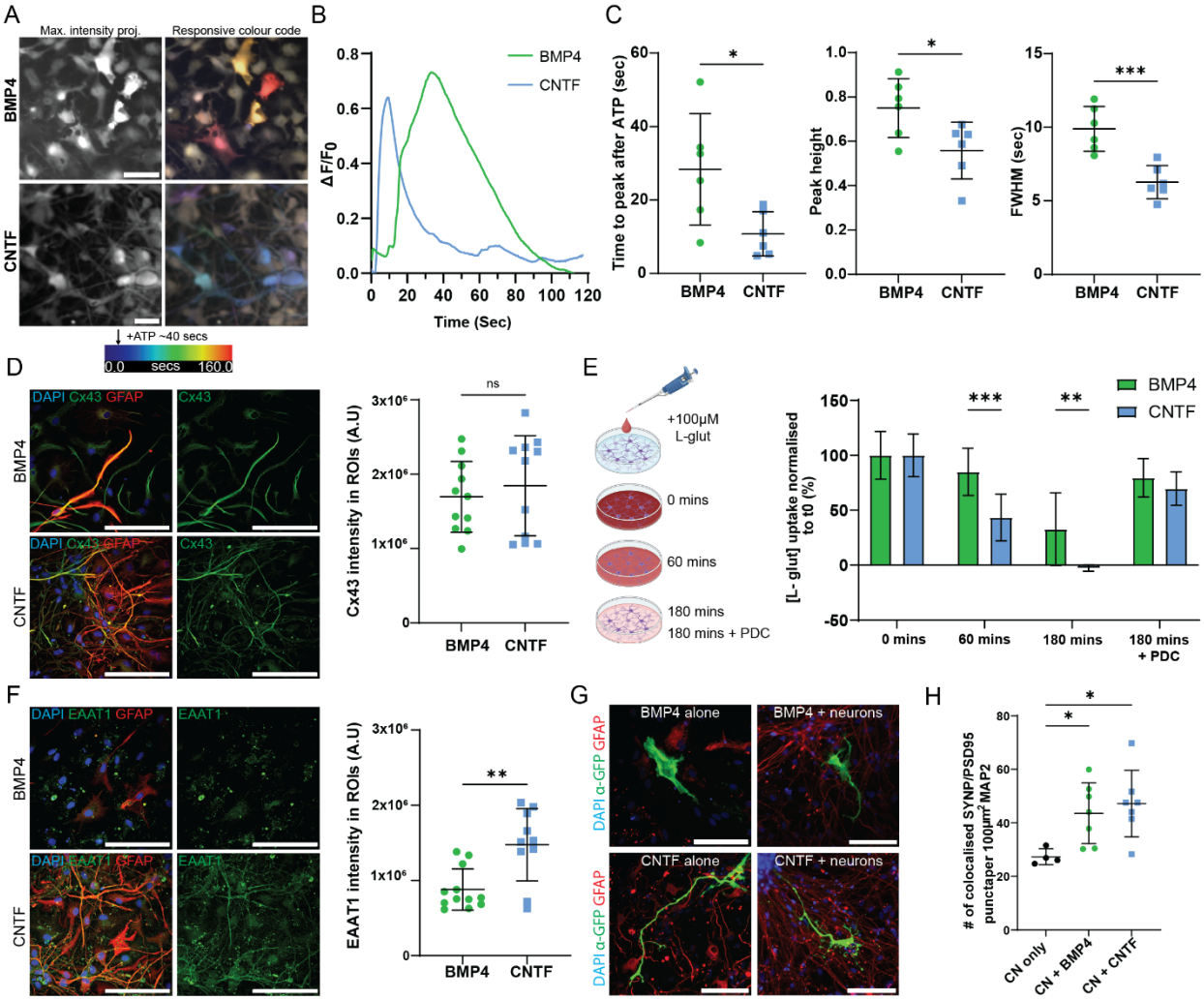

Figure 3 – BMP4 and CNTF astrocytes display different homeostatic functional profiles. *A-C) BMP4 and CNTF astrocytes have different calcium wave kinetics. A) Temporal colour-coding analysis. Time lapse images of astrocytes loaded with calcium-sensitive indicator Fluo4-AM and stimulated with ATP to initiate ATP-responsive calcium waves were taken. Stacks were processed with temporal color-coding to show at what frame after ATP application (frame 50) the highest peak in intensity occurs for each cell. White indicates cells that did not change intensity, whilst cells coloured in blue spiked earlier than those coloured in yellow-red. Scale bar: 100 μm. B-C) Quantification of calcium spike characteristics (FWHM: full width half maximum). Data represents well averages of 2 control lines from 2 experimental blocks with 6 technical replicates total, median ± IQR. Unpaired t-tests or Mann-Whitney tests were used to test for significance. ****p<0.0001, ***p<0.001, *p<0.05. D) Representative images of BMP4 and CNTF astrocytes stained for connexin-43 (CX43), nucleus (DAPI) and intermediate filaments (GFAP) and quantification of CX43 fluorescence intensity within regions of interest (ROIs). Data points represent well averages of 2 control lines from 2 experimental blocks with 10 technical replicates (n=10-11 wells), mean ± SD. Unpaired t-test was used to test for significance. **p<0.01, ns: non-significant. Scale bar: 100 μm. E-F) CNTF astrocytes have faster glutamate uptake dynamics. E) In vitro fluorometric glutamate (L-glut) uptake assay*

*protocol was performed using inhibitor L-trans-pyrrolidine- 2,4-dicarboxylate (PDC) to block glutamate flux through glutamate transporters in the 180-minute incubation. Quantification of fluorescence corresponding to known concentrations of glutamate was performed and normalised to the number of cells and to baseline (t0) control. Data points represent well averages of 2 control lines from 2 experimental blocks with 7-8 technical replicates (n=7-8 wells), mean ± SD. Two-way ANOVA with Šídák's multiple comparisons to test for significance between BMP4 versus CNTF astrocytes at different timepoints. F) Representative images of BMP4 and CNTF astrocytes stained for glutamate transporter (EAAT1), nucleus (DAPI) and intermediate filaments (GFAP) and quantification of EAAT1 fluorescence intensity within regions of interest (ROIs). Data points represent well averages of 2 control lines from 2 experimental blocks with 10 technical replicates (n=10-11 wells), mean ± SD. Unpaired t-test was used to test for significance. **p<0.01, ns: non-significant. Scale bar: 100µm. G) Representative fluorescent images of GFP$^+$ BMP4 and CNTF astrocytes cultured alone or with human stem-cell- derived motor neurons (BMP4 + neurons, CNTF + neurons) and stained with α-GFP, nuclear staining (DAPI) and neuronal tubulin (β3-Tub) or astrocyte intermediate filaments (GFAP). Scalebar: 100 µm. H) Quantification of the number of colocalised SYN and PSD95 puncta per 100 µm^2 MAP2 positive dendrite areas in cortical neurons cultured alone (CN only) or in the presence of BMP4 (CN+BMP4 ACs) or CNTF (CN+CNTF ACs) astrocytes. Datapoints represent well averages of 2 control lines (for astrocytes) for 2 experimental blocks with 4- 8 technical replicates (n=4-8 wells). One-way ANOVA with Dunn's multiple comparisons to test for significance, mean ± SD, ***p<0.001, *p<0.05.*

346 *BMP4 and CNTF astrocytes constitute transcriptionally distinct subtypes*

347 Having established that BMP4 and CNTF astrocytes are functionally and morphologically
348 distinct subtypes, we investigated their transcriptomic profiles to elucidate the molecular basis
349 of these differences.

350 We then performed bulk RNA-sequencing (RNA-seq) on astrocyte progenitors under basal
351 conditions, as well as BMP4- and CNTF astrocytes differentiated for 2 and 3-weeks (**Figure**
352 **4A**) to compare their transcriptional profiles. Our analysis revealed minimal differences
353 between 2- and 3-weeks differentiated astrocytes, for both BMP4 and CNTF (**Figure S4**).
354 Therefore, we focused our analysis on 3-week differentiated astrocytes (**Figure 4A**). Principal
355 component analysis (PCA) highlighted that both astrocytes subtypes are transcriptionally
356 distinct from progenitors and from each other (**Figure 4B**), with 2162 differentially expressed
357 genes (DEGs) between BMP4 and CNTF astrocytes (**Figure 4C**). Importantly, comparing
358 these DEGs, we were able to confirm at the gene expression level (**Figure S5**) what we
359 previously observed at the protein level (**Figure 3D and 3F**) for *Slc1a3* (EAAT1) and *Cx43*
360 (Connexin-43). When we compared the differentially expressed genes (DEGs) between
361 progenitors and each subtype, we found that around a half of all DEGs are shared between
362 both differentiation protocols, while the other half is uniquely altered between astrocytes
363 differentiated with either BMP4 or CNTF cytokines (**Figure 4D**). This suggests that, while the
364 process of differentiation from progenitors involves common mechanisms, BMP4 and CNTF
365 astrocytes also undergo unique changes that contribute to forming their distinct identities and,
366 potentially, their divergent morphologies.

367 To determine the biological pathways underlying the specialization of BMP4 and CNTF
368 astrocytes, we performed gene set enrichment analysis (**Figure 4E and S6-S11**).

369 As expected, compared with astrocyte progenitors, in both BMP4- and CNTF-differentiated
370 astrocytes the main downregulated gene sets are related to cell division and DNA replication,
371 which suggests that both differentiation processes give rise to post-mitotic cells (**Figure 4E**).

372 Comparing the two differentiated subtypes, we observed that gene sets with the highest
373 normalized enrichment score (NES) for CNTF astrocytes compared to BMP4 astrocytes were
374 overwhelmingly associated with the microtubule cytoskeleton. On the other hand, gene sets
375 enriched in BMP4 differentiated astrocytes were related to development and morphogenesis,
376 which is in accordance with the functions carried out by BMPs in these processes.

377 Next, we wanted to compare the transcriptional profile of BMP4- and CNTF-differentiated
378 astrocytes generated using our *in vitro* system with recently published single cell RNA profiling
379 datasets of different cell types isolated directly from the human brain[41,42] and found that both

380 show a strong correlation with human astrocytes (Pearson's correlation coefficient r=0.5 and
381 0.61 for BMP4- and CNTF-differentiated astrocyte DEGs with adjusted p-value<0.05,
382 respectively) (**Figure S12A-B and S13A-B**). In addition, the comparison with a recently
383 generated dataset comprising single nuclei RNA-seq data from white and grey matter
384 astrocytes[43] revealed that both subtypes show a more significant correlation with white matter
385 astrocytes, with CNTF astrocytes displaying higher correlation to some of the specific white
386 matter astrocyte clusters identified, namely ciliated astrocytes (**Figure S14A-C**).

387

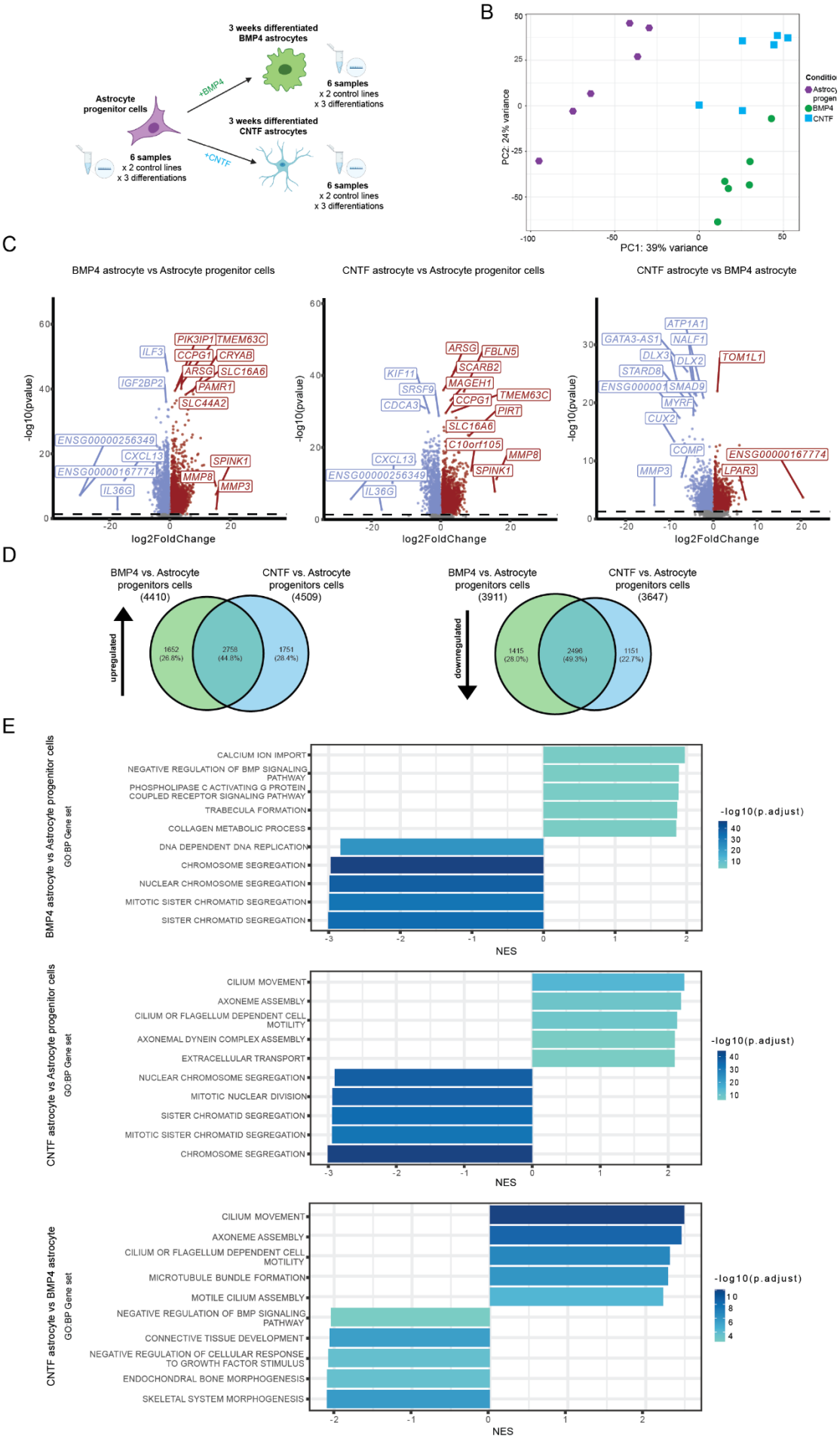
B
3 weeks differentiated BMP4 astrocytes
6 samples
x 2 control lines
x 3 differentiations
Astrocyte progenitor cells
+BMP4
3 weeks differentiated CNTF astrocytes
+CNTF
6 samples
x 2 control lines
x 3 differentiations
6 samples
x 2 control lines
x 3 differentiations
PC2: 24% variance
PC1: 39% variance
Conditio
Astrocy progen
BMP4
CNTF
C
BMP4 astrocyte vs Astrocyte progenitor cells
CNTF astrocyte vs Astrocyte progenitor cells
CNTF astrocyte vs BMP4 astrocyte
-log10(pvalue)
log2FoldChange
PIK3IP1
TMEM63C
CCPG1
CRYAB
ARSG
SLC16A6
PAMR1
SLC44A2
ILF3
IGF2BP2
ENSG00000256349
CXCL13
ENSG00000167774
IL36G
MMP8
SPINK1
MMP3
FBLN5
SCARB2
KIF11
SRSF9
MAGEH1
CDCA3
PIRT
C10orf105
ATP1A1
GATA3-AS1
NALF1
DLX3
DLX2
TOM1L1
STARD8
ENSG00000167774
LPAR3
D
BMP4 vs. Astrocyte progenitors cells (4410)
CNTF vs. Astrocyte progenitors cells (4509)
upregulated
1652 (26.8%)
2758 (44.8%)
1751 (28.4%)
BMP4 vs. Astrocyte progenitors cells (3911)
CNTF vs. Astrocyte progenitors cells (3647)
downregulated
1415 (28.0%)
2496 (49.3%)
1151 (22.7%)
E
BMP4 astrocyte vs Astrocyte progenitor cells
GO:BP Gene set
CALCIUM ION IMPORT
NEGATIVE REGULATION OF BMP SIGNALING PATHWAY
PHOSPHOLIPASE C ACTIVATING G PROTEIN COUPLED RECEPTOR SIGNALING PATHWAY
TRABECULA FORMATION
COLLAGEN METABOLIC PROCESS
DNA DEPENDENT DNA REPLICATION
CHROMOSOME SEGREGATION
NUCLEAR CHROMOSOME SEGREGATION
MITOTIC SISTER CHROMATID SEGREGATION
SISTER CHROMATID SEGREGATION
NES
-log10(p.adjust)
CNTF astrocyte vs Astrocyte progenitor cells
CILIUM MOVEMENT
AXONEME ASSEMBLY
CILIUM OR FLAGELLUM DEPENDENT CELL MOTILITY
AXONEMAL DYNEIN COMPLEX ASSEMBLY
EXTRACELLULAR TRANSPORT
NUCLEAR CHROMOSOME SEGREGATION
MITOTIC NUCLEAR DIVISION
SISTER CHROMATID SEGREGATION
MITOTIC SISTER CHROMATID SEGREGATION
CHROMOSOME SEGREGATION
CNTF astrocyte vs BMP4 astrocyte
CILIUM MOVEMENT
AXONEME ASSEMBLY
CILIUM OR FLAGELLUM DEPENDENT CELL MOTILITY
MICROTUBULE BUNDLE FORMATION
MOTILE CILIUM ASSEMBLY
NEGATIVE REGULATION OF BMP SIGNALING PATHWAY
CONNECTIVE TISSUE DEVELOPMENT
NEGATIVE REGULATION OF CELLULAR RESPONSE TO GROWTH FACTOR STIMULUS
ENDOCHONDRAL BONE MORPHOGENESIS
SKELETAL SYSTEM MORPHOGENESIS

389 ***Figure 4 – Transcriptional profile differences between BMP4 and CNTF astrocyte***
390 ***subtypes.*** *A) Schematic of the experimental protocol for bulk RNA sequencing of astrocyte*
391 *progenitors and 3-week differentiated BMP4 and CNTF astrocytes. For each timepoint, 6*
392 *samples were analysed, coming from 2 control lines with 3 independent differentiations*
393 *performed for each line. B) Principal component analysis of transcripts from astrocyte*
394 *progenitors and BMP4 and CNTF differentiated astrocytes. C) Pairwise comparison volcano*
395 *plots with top differentially downregulated (blue) and upregulated (red) genes (adjusted p-*
396 *value<0.05) for BMP4 astrocytes versus Astrocyte progenitors, CNTF astrocytes vs. Astrocyte*
397 *progenitors, and CNTF astrocytes versus BMP4 astrocytes. The significance (-$\log_{10}$ p-value)*
398 *is plotted on the Y axis while the fold change ($\log_2$ fold change) is plotted on the X axis. D)*
399 *Venn diagrams showing the percentages of common and subtype-specific genes that are*
400 *upregulated or downregulated during the transition between progenitors and differentiated*
401 *BMP4 and CNTF astrocytes. E) Bar plot showing the top 5 gene sets upregulated and*
402 *downregulated in BMP4 astrocytes versus astrocyte progenitors, CNTF astrocytes versus*
403 *astrocyte progenitors, and CNTF astrocytes versus BMP4 astrocytes. Gene sets were derived*
404 *from the Biological Process (BP) ontology. Gene sets are ordered according to the absolute*
405 *effect size (NES) and coloured by significance (-$\log_{10}$ p-value adjusted).*

406

407 *Effect of BMP4 and CNTF on primary isolated mouse astrocytes*

408 After analysing the differential gene expression profiles of our human astrocytes differentiated
409 with BMP4 and CNTF, we evaluated whether these growth factors have similar effects on
410 primary rodent astrocytes. We isolated astrocytes from the neocortex of postnatal day (P) 2-3
411 mouse pups according to a previously described protocol[44]. After early-stage differentiation,
412 immature astrocytes were treated for 7 days with BMP4 or CNTF. We used the previously
413 validated astrocyte trophic factor heparin-binding EGF-like growth factor (HBEGF)[44,45], or left
414 cells untreated as controls (**Figure 5A**).

415 Brightfield imaging on Day 7 of treatment revealed similar patterns of morphology to human
416 astrocytes (**Figure 5B**). We found that BMP4-treated mouse astrocytes often had rounder
417 morphologies, with shorter processes extending from a large soma. CNTF-treated astrocytes
418 adopted less round morphologies with longer processes extending from relatively smaller
419 somas. We found that there was more heterogeneity within these mouse astrocytes than the
420 human astrocytes, likely owing to the fact that astrocytes obtained by acute isolation represent
421 a more heterogenous population at baseline than would stem cell derived astrocytes.

422 We next performed bulk RNA-seq to evaluate transcriptomic changes between BMP4 and
423 CNTF-treated astrocytes. PCA analysis revealed that both BMP4 and CNTF-treated
424 astrocytes were transcriptionally distinct from one another and from untreated astrocytes
425 (**Figure 5C**). Interestingly, CNTF and HBEGF-treated astrocytes were transcriptionally similar.
426 Before performing differential expression analysis, we confirmed the purity of our cultures by

427 evaluating robust expression of various astrocytic marker genes, as well as low-to-no
428 expression of marker genes for other potential contaminating cell types (**Figure 5D**).
429 Importantly, even untreated mouse astrocytes were highly pure, suggesting that they are
430 already committed to an astrocyte fate after purification which parallels human astrocyte
431 progenitors.

432

433 Differential gene expression analysis detailed transcriptomic differences between BMP4 and
434 CNTF-treated astrocytes (**Figure 5E**). We find found 2649 DEGs between BMP4 and CNTF-
435 treated astrocytes (log2FoldChange < -0.6; p-value < 0.05). To investigate similarities from
436 between human to mouse astrocytes, we looked at SLC1A3lc1a3 Slc1a3 and GjaJAja1
437 expression levels across conditions (**Figure S15**). We saw higher expression of SLC1A3lc1a3
438 Slc1a3 in CNTF-treated astrocytes than BMP4-treated astrocytes, which corroborates the
439 functional glutamate uptake assay, immunostaining and sequencing results in human
440 astrocytes (**Figure 3E-F and S5**). Gja1 expression was similar across treatments, also
441 corroborating the immunostaining and sequencing of human astrocytes (**Figure 3D and**
442 **Figure S5**).

443

444 Finally, to investigate the biological pathways being differentially regulated by BMP4 and
445 CNTF, we performed GO biological pathway gene set enrichment analysis (**Figure 5F**). Like
446 human astrocytes, mouse astrocytes treated with CNTF were enriched for pathways involving
447 microtubule and cilium movement. On the other hand, BMP4-treated mouse astrocytes were
448 enriched for pathways involving the extracellular matrix, possibly pointing to a role for BMP4
449 astrocytes in establishing the extracellular milieu. In summary, these data show that many of
450 the upregulated gene and pathways that respond to developmental BMP4 and CNTF
451 treatment in mouse astrocytes areis evolutionarily conserved in human. Morphologies
452 between human and mouse astrocytes were similar, and CNTF-treated astrocytes in both
453 humans and mice upregulate transcripts associated with cilium and microtubule movement,
454 which is related to their relatively more process-bearing morphology. in both human and
455 mouse astrocytes.

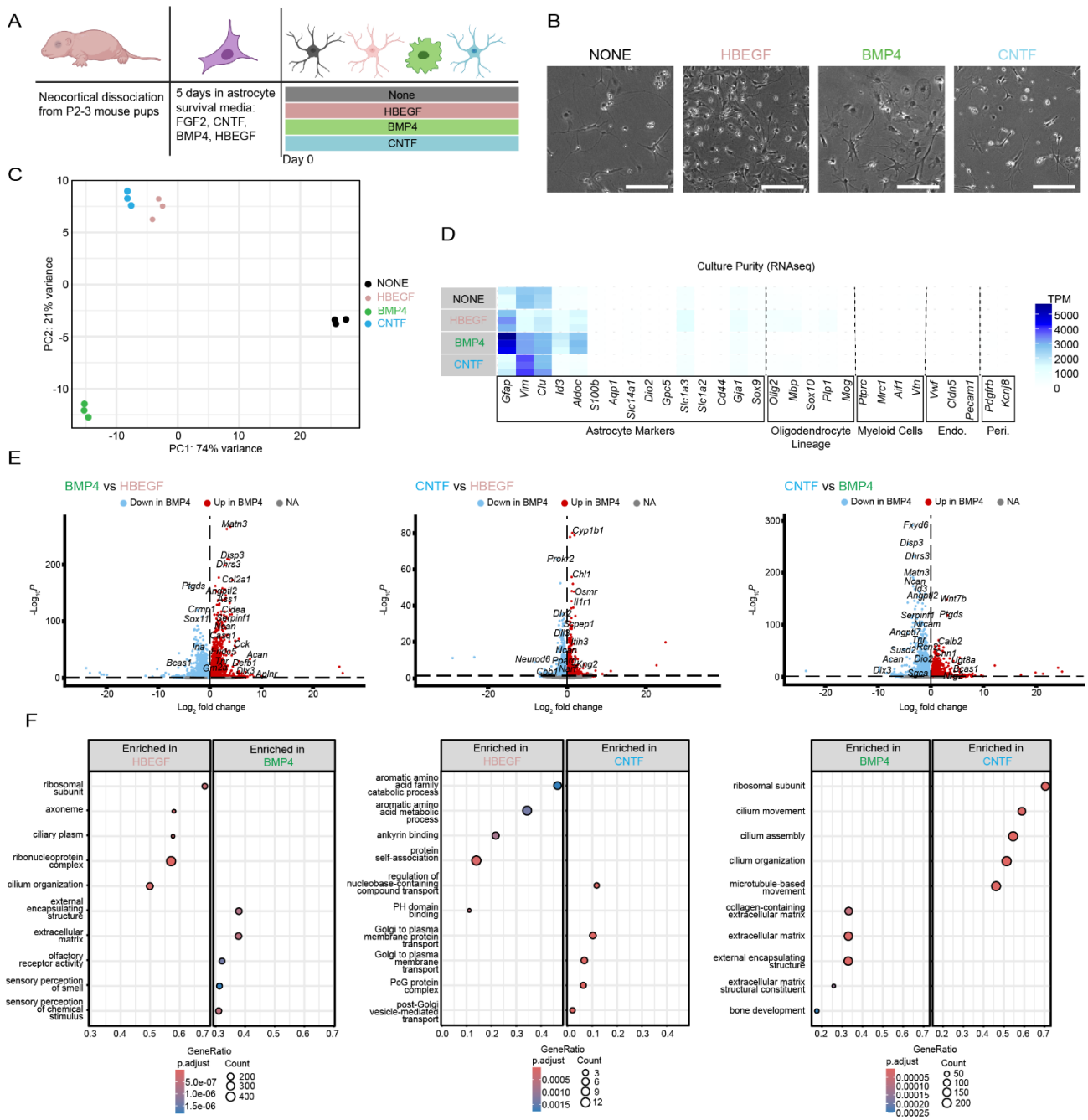

Figure 5 – Effects of BMP4 and CNTF on mouse primary astrocytes. *A) Schematic for generation of mouse astrocytes. B) Representative brightfield images of astrocytes treated for each condition at 7 days; scale bar is 20 µm. C) Dimensionality reduction by principal components 1 and 2 of sequenced samples. Each dot represents an individual technical replicate and experimental conditions are grouped by color (n=3 technical replicates/condition). D) Heatmap of transcript per million (TPM) expression of various CNS cell type marker genes across experimental conditions. Known cell type markers are grouped along X axis by cell type (n=3 technical replicates/condition). Rows are representative of individual technical replicates. E) Volcano plots of differentially expressed genes between respective treatment conditions. Positive log_2 fold change is representative of enrichment while negative log_2 fold change is representative of de-enrichment. F) Dot plotting of GO biological process gene set enrichment. Gene ratio describes the ratio of significantly changed*

469 *genes to the total genes in each pathway set. Dot size represents the total number of enriched*
470 *or de-enriched genes while color is representative of adjusted p-value.*

471

472 *The morphology of BMP4 and CNTF astrocytes relies on distinct cytoskeletal components*

473 Based on the transcriptomic analysis results and our previous observations on their
474 morphology, we hypothesised that a different cytoskeletal organization might underpin the
475 distinct phenotypes of our astrocyte subtypes. To test this, we first investigated the role of the
476 actin cytoskeleton in determining astrocyte morphology in our system. We exposed GFP^+
477 BMP4- and CNTF- differentiated astrocytes for 2 hours to either latrunculin B[46] (LAT B; 1 μM)
478 or Rho-associated, coiled-coil containing protein kinase (ROCK) inhibitor Y27632
479 dihydrochloride[47] (Y27632; 25 μM), which both interfere directly or indirectly with actin
480 polymerization and contractility, and performed single-cell morphology profiling using our
481 semi-automated pipeline.

482 We found that BMP4 astrocytes treated with Y27632 displayed a more ramified morphology,
483 with processes emanating from the cell body (**Figure 6A**), although the overall size remained
484 unchanged, while DMSO-treated controls remained unaffected (**Figure S16A**). Conversely,
485 treatment with LAT B caused a decrease in area, as well as the acquisition of a more irregular
486 and ramified shape (**Figure 6A**). The same effects were also evident in the quantification of
487 the key shape descriptors (**Figure 6B and S16B**). Interestingly, CNTF astrocytes treated with
488 either drug remained mostly unchanged, suggesting that actin disruption does not affect their
489 overall architecture (**Figure 6A-B and S16B**). The same effects observed on cultures sparsely
490 transfected with GFP were also verified at the population level, by immunostaining for the
491 tubulin cytoskeleton, which is presumed to be unaffected by these interventions (**Figure**
492 **S16C**).

493 To assess potential differences between the reliance of BMP4 and CNTF astrocyte
494 morphological features on microtubular cytoskeletal components, we exposed differentiated
495 astrocytes to increasing concentrations of the microtubule destabilising drug vincristine[48] (VIN;
496 1, 10, 50 and 100 nM). VIN was effective in altering the microtubular architecture for both
497 BMP4 and CNTF astrocyte subtypes (**Figure 6D**), however, only CNTF astrocytes showed a
498 radical alteration in their overall architecture. BMP4 cells were largely unchanged (**Figure 6C**
499 **top**), with only a decrease in area with concentrations of VIN above 10 nM (**Figure 6E**). As
500 the effect size of this is quite small and none of the other shape descriptors displayed
501 significant differences, we concluded that the overall architecture of BMP4 astrocytes is not
502 overly reliant on the microtubule network, but rather on actin contractility (**Figure 5E and**
503 **S16D**).

504 Conversely, we found that in CNTF astrocytes VIN causes a concentration-dependent
505 shortening of the cell processes, which constitute the main morphological hallmark of these
506 cells (**Figure 6C, bottom**). This was then validated by the quantification of morphometric
507 parameters which showed that these cells display a reduction in area, compactness, and
508 perimeter at all VIN concentrations except for 1 nM, while the median radius was only altered
509 in the 50 nM condition (**Figure 6E and S16D**).

510 Our combined investigation of cytoskeletal components, supported by the RNA-seq data and
511 morphological analysis, indicates that BMP4 astrocytes rely mostly on actin polymerization
512 and contractility for their shape, while CNTF astrocytes likely owe their morphology to a stable
513 polymerized microtubule network.

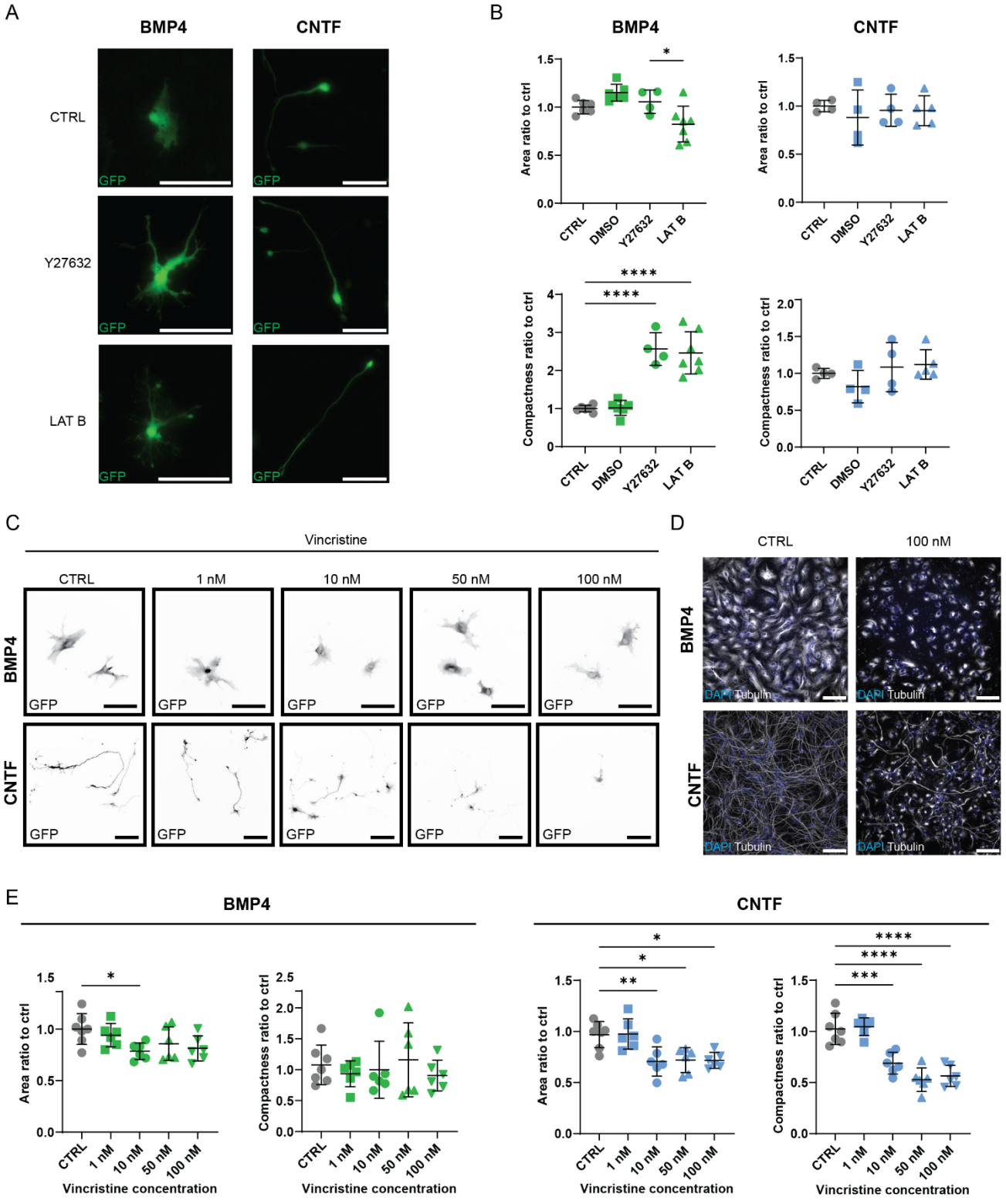

514

515 ***Figure 6 – The morphology of BMP4 and CNTF astrocytes relies differently on the actin***
516 ***and microtubule cytoskeleton.*** *A-B) Actin inhibition significantly affects the morphology of*
517 *BMP4 astrocytes but not that of CNTF astrocytes. A) Representative images of GFP⁺ BMP4*
518 *and CNTF astrocytes, either untreated (CTRL) or treated with actin inhibitors Y27632*
519 *dihydrochloride (Y27632; 25 µM) or latrunculin B (LAT B; 1 µM) for 2 hours before live imaging.*
520 *Scale bar: 100 µm. B) Quantification of shape changes in the presence of actin inhibitors*
521 *analysing area and compactness expressed as a ratio compared to control (ctrl, black). Data*

522 *represents well averages of technical replicates of 2 control lines from 2 experimental blocks*
523 *(n=4-5 wells total), mean ± SD. Ordinary one-way ANOVAs with Tukey's post-hoc was used to*
524 *test for significance. *p<0.05, **p<0.01, ****p<0.0001 ns or no comparisons shown: non-*
525 *significant. C-E) Microtubule destabilisation significantly affects the morphology of CNTF*
526 *astrocytes but not that of BMP4 astrocytes. C) Representative images of GFP$^+$ BMP4 and*
527 *CNTF astrocytes either left untreated (CTRL) or treated with increasing concentrations of*
528 *vincristine (1, 10, 50 and 100 nM). Scale bar: 100 µm. D) Representative images of BMP4 and*
529 *CNTF astrocytes, either untreated (ctrl) or treated with 100 nM vincristine, stained with nuclear*
530 *(DAPI, blue) and microtubule cytoskeletal markers (Tubulin, white). Scale bar: 100 µm. E)*
531 *Quantification of shape changes in the presence of vincristine analysing area and*
532 *compactness, expressed as a ratio compared to control (ctrl, black). Data represents well*
533 *averages of technical replicates of 2 control lines from 2 experimental blocks (n=6-7 wells*
534 *total), mean ± SD. Ordinary one-way ANOVAs with Tukey's post-hoc was used to test for*
535 *significance.*

536 *The distinct morphology of BMP4 and CNTF astrocytes correlates with different distribution*
537 *and motility features of their mitochondria*

538 While astrocytes use glycolysis for most energy production[49], they also heavily rely on
539 mitochondria for calcium storage and signaling, as well as fatty acid and neurotransmitter
540 metabolism[50–52]. Astrocyte mitochondria are located in cytoplasmic microdomains throughout
541 the cell, including in the finer processes[53], in order to meet local energy demands and upkeep
542 ionic balance[56].

543 While the propagation and modulation of astrocytic ICWs is mainly mediated by the
544 endoplasmic reticulum (ER)[54], mitochondria also actively participate in local Ca^{2+} dynamics
545 both by releasing and sequestering Ca^{2+} [52]. Given the observed differences in ICW dynamics
546 between the astrocyte subtypes, and the fact that mitochondrial transport is microtubule-
547 bound[55], we reasoned that the observed differences between the cytoskeletal organization of
548 BMP4 and CNTF astrocytes may indicate a potential difference in distribution and motility of
549 mitochondria between these cells.

550 To evaluate mitochondrial distribution within single cells, we transfected BMP4 and CNTF
551 astrocytes with both a cytoplasmic RFP and a mitochondrial targeted fluorophore (mito-
552 dendra2)[56] before fixing them and staining the nuclei with DAPI. We then segmented each cell
553 into 25 µm bins automatically marked radially around the nuclei (**Figure 7A**) and quantified the
554 proportion of fluorescence intensity as a proxy of mitochondrial distribution in the different
555 compartments (**Figure 7B**). While BMP4 cells maintain over 60% of their mitochondria in the
556 perinuclear space (i.e. 0-25 µm from nucleus edge), in CNTF astrocytes less than half of the
557 mitochondria are localized within this perinuclear space. Instead, there seems to be numerous
558 hotspots of Mitodendra2 signal distributed along the cell processes (**Figure 7B&C**).
559 Additionally, BMP4 cells overall show a higher number of mitochondria occupying their

560 cytoplasm per unit area, which may be due to a difference in either content or size of the
561 mitochondria between the two subtypes (**Figure 7D**).

562 We next sought to test whether the distribution of mitochondria in the two subtypes could be
563 linked to their motility within the astrocytes. To do this, we performed live imaging on BMP4
564 and CNTF astrocytes co-transfected with RFP and mito-dendra2 and stained with Hoechst
565 33342 to visualize the nucleus (**Figure 7E-F**). Mitochondrial movements were recorded over
566 2 minutes at 0.1 frame/sec across 25 μm^2 regions of interest (ROIs) drawn either in the
567 perinuclear region (0-25 µm from the nucleus, **Figure 7E** inset 1&3), in a non-perinuclear area
568 (25-100 µm from the nucleus, **Figure 7E,** inset 2&4), or in the case of CNTF astrocytes, in an
569 area at the end of a process (0-50 µm from the process end, **Figure 7E** inset 5). Analysis of
570 these ROIs across different cells and replicated revealed that, while BMP4 astrocytes show no
571 difference in mitochondrial motility between the perinuclear and non-perinuclear regions,
572 CNTF astrocytes show a two-fold increase in the fraction of motile mitochondria at the end of
573 the processes compared to either their perinuclear or non-perinuclear areas (**Figure 7G**).

574 Taken together, these results show that distribution and motility of mitochondria differs
575 substantially between the two subtypes, potentially indicating a distinct organisation of the
576 subcellular domains in CNTF astrocytes. In particular, the higher presence of mitochondrial
577 hotspots in the periphery of CNTF astrocytes matches our findings regarding their dependence
578 on a stable microtubule network (**Figure 5D-E**) and it may hint towards one of the mechanisms
579 behind the faster ICW dynamics in these cells (**Figure 3A-B**).

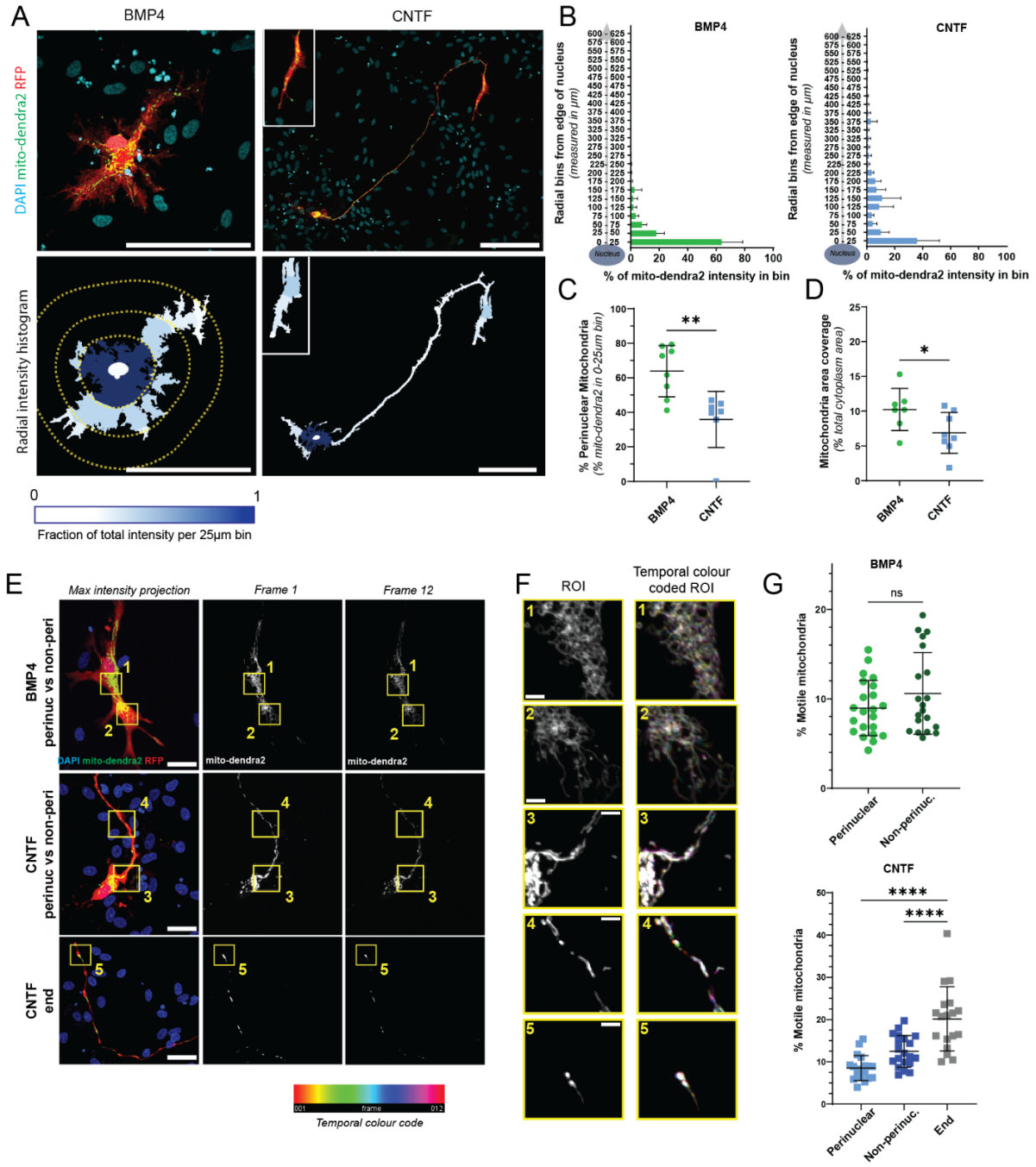

Figure 7 – Mitochondrial distribution and motility differ between BMP4 and CNTF astrocytes. *A) BMP4 and CNTF 2-weeks differentiated astrocytes were co-transfected with cytoplasmic RFP (red) and mito-dendra2 (green), fixed and immunostained with a nuclear marker (DAPI, blue). The co-transfection shows the distribution of mitochondria within single cells, highlighting the hotspots of mitochondria throughout the processes (zoom inset, CNTF astrocyte). Quantification was performed by measuring mito-dendra2 intensity in 25 µm radial bins around the nucleus (marked with DAPI) within whole single cells, segmented using RFP. The fractional contribution of mito-dendra2 intensity within each bin throughout the entire cell is coloured coded in a gradient from white (0) to dark blue (1). B) Quantification of the fraction of mito-dendra2 intensity per 25 µm radial bin around the nucleus expressed as a percentage in both BMP4 and CNTF astrocytes. C) Quantification of the fraction of mito-dendra2 signal contained within the first radial bin (0-25 µm) as a percentage of the total for BMP4 astrocytes*

*(BMP4 perinuc.) and CNTF astrocytes (CNTF perinuc.). D) Quantification of mitochondria (mito-dendra2) area coverage expressed as percentage of the whole cytoplasm area (RFP) in BMP4 and CNTF astrocytes. Data represents well averages of technical replicates of 2 control lines from 2 experimental blocks (n=6-8 wells), mean ± SD. Unpaired t-tests were used to test for significance. **p<0.01, *p<0.05. E) BMP4 and CNTF astrocytes were co-transfected with free-floating RFP (red) and mito-dendra2 (green) and live dyed with Hoescht 33342 (blue). Maximum intensity projections show regions of BMP4 and CNTF astrocytes, with representative time lapse images of beginning (frame 1) and end (frame 12) of videos for mitochondrial motility analysis over 2 minutes of imaging (mito-dendra2, white). Scale bar: 100 µm. Yellow zoom insets 1 and 2 show perinuclear and non-perinuclear regions, whilst yellow zoom insets 3 for CNTF astrocytes shows the end of the process used as regions of interest (ROIs) for analysis (25 µm x 25 µm ROIs). F) Temporal colour coded ROIs show stationary mitochondria as white, whilst coloured pixels indicate the frame in which there was the most recent change in motility. Scale bar: 5 µm. G) Quantification of the percentage of motile mitochondria within each subcellular compartment for BMP4 astrocytes (perinuclear vs non-perinuclear) and CNTF astrocytes (perinuclear vs non-perinuclear vs end of process). Data represents averages of percent change from each slice for each cell, of 2 control lines from 2 experimental blocks (n=18-23 cells from 7-8 wells), mean ± SD. Mann-Whitney U test was used to test for significance for BMP4 cells and ordinary one-way ANOVA with Tukey's post-hoc used to test for significance for CNTF cells. ****p<0.0001, ns: non-significant.*

<u>BMP4 and CNTF astrocytes have distinct transcriptional and functional reactive phenotypes</u>

Astrocytes respond to a wide range of pathophysiological stimuli, inflammation, and injury by undergoing a profound transformation in their morphological, functional and molecular profile which is commonly referred to as 'reactivity'[57]. As astrocyte reactivity can generate a wide range of phenotypic outcomes[58], we were interested in understanding whether it would differentially impact the two human astrocyte subtypes. We therefore treated 2-week differentiated BMP4 and CNTF astrocytes for an additional week in the presence or absence of an established cocktail of factors known to induce astrocyte reactivity comprising of TNF, IL-1α, and C1q (TIC)[59], and performed bulk RNA-seq comparing treated and untreated astrocytes (**Figure 8A**). We found that, in both cases, reactivity induced a significant transcriptomic transformation, with the upregulation of known pro-inflammatory genes (e.g. *IL36*, *CXCL13*, and *CSF3*) in the treated astrocytes compared to their untreated counterpart (**Figure 8B-C**),

However, when directly comparing the expression profiles of reactive BMP and CTNF astrocytes (**Figure 8D-E**), we observed that, in addition to a significant number of these common pan-reactive markers, there were also many DEGs that were unique to either astrocyte reactive subtype (**Figure 8E**). For example, we noted differences in the expression of genes such as *MMP3* (upregulated in CNTF, but not in BMP4 reactive astrocytes) and *ACAN* (upregulated in BMP4, but not in CNTF reactive astrocytes), among others (**Figure 8D**). Interestingly, there was a higher number of CNTF-specific DEGs (55.8% of upregulated genes

633 and 59.2% of downregulated genes), while common DEGs represent 34.9% and 28.5% of up-
634 and downregulated genes, respectively. This indicates that the majority of genes that change
635 their expression during reactivity are CNTF-specific, followed by a lower percentage of genes
636 that are shared among both substates, with the lowest percentage constituted of BMP4-
637 specific DEGs (**Figure 8E**).

638 To better understand which biological pathways might be involved in the respective reactive
639 transition of BMP4 and CNTF astrocytes, we also performed gene set enrichment analysis
640 (**Figure 8F and Figure S10A-C**). This analysis indicated that, as expected, the majority of
641 gene sets upregulated in both cell types upon exposure to TIC is related to immune regulation
642 and, in particular, the modulation of immune cell migration.

643 When focusing on the comparison between reactive CNTF and reactive BMP4 astrocytes, we
644 observed that gene sets specifically enriched in CNTF reactive astrocytes seem to be
645 associated with antiviral responses which may point towards a specialized function of CNTF
646 astrocytes in this context. On the other hand, gene sets enriched in reactive BMP4 astrocytes
647 compared to reactive CNTF astrocytes were linked with morphogenesis, cell signalling and
648 extracellular matrix (ECM) production. We also observed that, when transitioning to a reactive
649 state, CNTF astrocytes seem to downregulate the same gene sets linked to the tubulin
650 cytoskeleton which were driving their differentiation from progenitors, suggesting a potential
651 morphological change.

652 Overall, the transcriptomic analysis suggests that BMP4 and CNTF astrocytes, beyond the
653 already shown functional differences in homeostatic conditions, might also acquire distinct
654 reactive states. We therefore wanted to verify whether the observed divergence in gene
655 expression translated into unique morphological and functional reactive profiles.

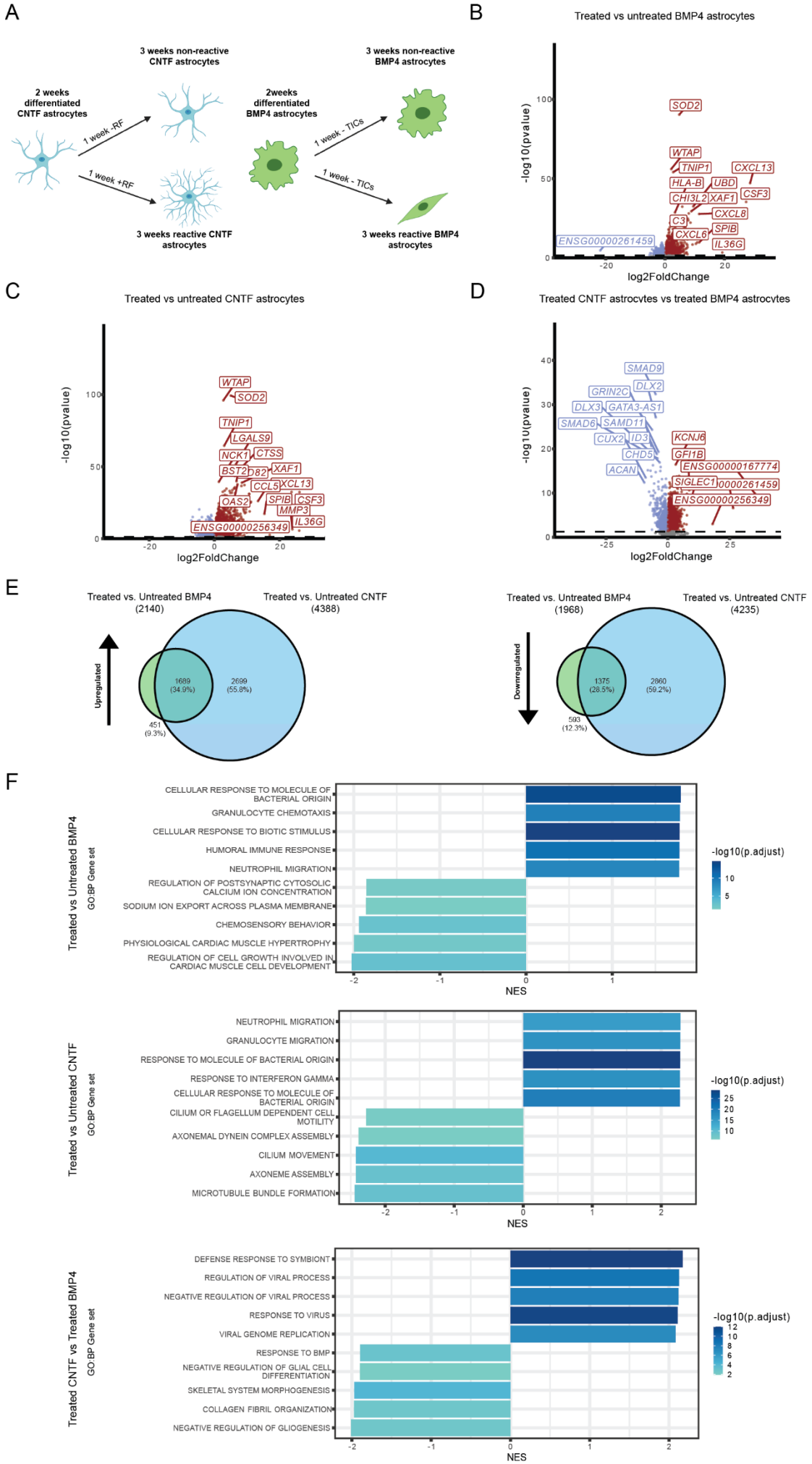
A
2 weeks differentiated CNTF astrocytes
1 week -RF
1 week +RF
3 weeks non-reactive CNTF astrocytes
3 weeks reactive CNTF astrocytes
2weeks differentiated BMP4 astrocytes
1 week - TICs
1 week - TICs
3 weeks non-reactive BMP4 astrocytes
3 weeks reactive BMP4 astrocytes
B
Treated vs untreated BMP4 astrocytes
-log10(pvalue)
log2FoldChange
SOD2
WTAP
TNIP1
CXCL13
HLA-B
UBD
CHI3L2
XAF1
CSF3
CXCL8
C3
SPIB
CXCL6
IL36G
ENSG00000261459
C
Treated vs untreated CNTF astrocytes
-log10(pvalue)
log2FoldChange
WTAP
SOD2
TNIP1
LGALS9
NCK1
CTSS
BST2
D82
XAF1
CCL5
XCL13
OAS2
SPIB
CSF3
MMP3
IL36G
ENSG00000256349
D
Treated CNTF astrocytes vs treated BMP4 astrocytes
-log10(pvalue)
log2FoldChange
SMAD9
DLX2
GRIN2C
DLX3
GATA3-AS1
SMAD6
SAMD11
CUX2
ID3
CHD5
ACAN
KCNJ6
GFI1B
ENSG00000167774
SIGLEC1
ENSG00000261459
ENSG00000256349
E
Treated vs. Untreated BMP4 (2140)
Treated vs. Untreated CNTF (4388)
Upregulated
1689 (34.9%)
2699 (55.8%)
451 (9.3%)
Treated vs. Untreated BMP4 (1968)
Treated vs. Untreated CNTF (4235)
Downregulated
1375 (28.5%)
2860 (59.2%)
593 (12.3%)
F
Treated vs Untreated BMP4
GO:BP Gene set
CELLULAR RESPONSE TO MOLECULE OF BACTERIAL ORIGIN
GRANULOCYTE CHEMOTAXIS
CELLULAR RESPONSE TO BIOTIC STIMULUS
HUMORAL IMMUNE RESPONSE
NEUTROPHIL MIGRATION
REGULATION OF POSTSYNAPTIC CYTOSOLIC CALCIUM ION CONCENTRATION
SODIUM ION EXPORT ACROSS PLASMA MEMBRANE
CHEMOSENSORY BEHAVIOR
PHYSIOLOGICAL CARDIAC MUSCLE HYPERTROPHY
REGULATION OF CELL GROWTH INVOLVED IN CARDIAC MUSCLE CELL DEVELOPMENT
NES
-log10(p.adjust)
Treated vs Untreated CNTF
GO:BP Gene set
NEUTROPHIL MIGRATION
GRANULOCYTE MIGRATION
RESPONSE TO MOLECULE OF BACTERIAL ORIGIN
RESPONSE TO INTERFERON GAMMA
CELLULAR RESPONSE TO MOLECULE OF BACTERIAL ORIGIN
CILIUM OR FLAGELLUM DEPENDENT CELL MOTILITY
AXONEMAL DYNEIN COMPLEX ASSEMBLY
CILIUM MOVEMENT
AXONEME ASSEMBLY
MICROTUBULE BUNDLE FORMATION
NES
-log10(p.adjust)
Treated CNTF vs Treated BMP4
GO:BP Gene set
DEFENSE RESPONSE TO SYMBIONT
REGULATION OF VIRAL PROCESS
NEGATIVE REGULATION OF VIRAL PROCESS
RESPONSE TO VIRUS
VIRAL GENOME REPLICATION
RESPONSE TO BMP
NEGATIVE REGULATION OF GLIAL CELL DIFFERENTIATION
SKELETAL SYSTEM MORPHOGENESIS
COLLAGEN FIBRIL ORGANIZATION
NEGATIVE REGULATION OF GLIOGENESIS
NES
-log10(p.adjust)

656

657 ***Figure 8 – The induction of reactivity causes distinct transcriptomic changes in BMP4***
658 ***and CNTF astrocytes.*** *A) Schematic of the experimental protocol for bulk RNA-sequencing*
659 *of astrocytes differentiated for three weeks with BMP4 or CNTF and with or without treatment*
660 *with known reactivity factors (TNF, IL-1α, C1q; TIC) during the third week of culture. For each*
661 *timepoint, six samples were analysed, coming from two control lines with three independent*
662 *differentiations performed for each line. B-D) Pairwise comparison volcano plots for treated*
663 *BMP4 astrocytes vs. untreated BMP4 astrocytes (B), treated CNTF astrocytes vs. untreated*
664 *CNTF astrocytes (C), and treated CNTF astrocytes versus treated BMP4 astrocytes (D). The*
665 *significance (-$\log_{10}$ p-value) is plotted on the Y axis while the fold change ($\log_2$ fold change) is*
666 *plotted on the X axis. Downregulated genes ($\log_2$FoldChange<-0.6; p-value<0.05) are*
667 *coloured in blue, while upregulated genes ($\log_2$FoldChange>0.6; p-value<0.05) are coloured*
668 *in red. E) Venn diagrams showing the percentages of common and subtype-specific genes*
669 *that are upregulated or downregulated in response to the induction of reactivity in BMP4 and*
670 *CNTF astrocytes. F) Bar plot showing the top five gene sets upregulated and downregulated*
671 *in treated BMP4 astrocytes vs. untreated BMP4 astrocytes, treated CNTF astrocytes vs.*
672 *untreated CNTF astrocytes, and treated CNTF astrocytes vs. treated BMP4 astrocytes. Gene*
673 *sets were derived from the Biological Process (BP) ontology. Gene sets are ordered according*
674 *to the absolute effect size (NES) and coloured by significance (-$\log_{10}$ p-value adjusted).*

675

676 As the baseline morphology of these two subtypes of astrocytes is very different, we first
677 wanted to test whether the induction of reactivity would make them diverge further or converge
678 to one common “reactive shape”.

679 Interestingly, when we performed the same morphological characterisation from **Figure 1** with
680 TIC versus control treated GFP^{+} BMP4 and CNTF astrocytes, we found that both subtypes
681 presented morphological alterations. However, while BMP4 astrocytes maintained the same
682 base morphology (i.e. perimeter and extent did not vary significantly at the single-cell level),
683 CNTF reactive astrocytes showed significantly reduced perimeter and increased extent
684 compared to their non-reactive counterparts, which points towards them having larger and
685 rounder cell bodies with shorter processes (**Figure 9Ai and B**). At the population level, we
686 also confirmed that in both subtypes the reactive transformation leads to a significant
687 rearrangement of the actin cytoskeleton (**Figure 9A ii**). This is particularly evident in BMP4
688 cultures which, when treated, seem to orient in patches around the culture and adopt a
689 “palisading” phenotype[60].

690 In addition to evaluating morphology, we also sought to investigate protein changes upon
691 reactivity induction in BMP4 and CNTF astrocytes. Complement factor 3 protein (C3) has
692 widely been reported as a marker of TIC-induced astrocytes [59,61,62 63]. We therefore
693 immunostained for C3 in our reactive and non-reactive BMP4 and CNTF astrocytes (**Figure**
694 **9C**). Protein levels revealed significant differences between the two subtypes. Specifically, in
695 BMP4 reactive astrocytes, C3 expression was highly heterogeneous across the culture, while
696 reactive CNTF astrocytes display a significant increase in C3 levels compared to both
697 untreated CNTF astrocytes and BMP4 conditions (**Figure 9C**).

698 This further validated that BMP4 and CNTF reactive astrocytes might represent different
699 reactive substates, even when stimulated with the same TIC cytokine cocktail, and motivated
700 us to assess their behaviour in an *in vitro* injury model. We performed a live imaging-based
701 scratch assay[64] (**Figure 9D i**) to assess whether BMP4 and CNTF astrocytes, either under
702 basal conditions or treated with TIC to induce reactivity, would respond differently to the
703 scratch and display differences in their ability to heal an *in vitro* ‘wound’.

704 We observed that reactive BMP4 astrocytes display a higher ability to fill the damaged area of
705 the culture by Day 7 after scratching compared to any other condition we evaluated, including
706 reactive CNTF astrocytes (**Figure 9D ii-iii**). Specifically, CNTF astrocytes would not close the
707 gap in the time-period we analyzed, and the pre-treatment with TICs did not significantly affect
708 their performance. Conversely, BMP4 astrocytes, which already in basal conditions show a
709 slightly higher area filled post-scratch, display a marked and significant increase in repair
710 capabilities in response to the induction of reactivity (**Figure 9D iii**).

711 This suggests that treating BMP4 astrocytes with TIC may produce a reactive substate that is
712 more responsive to injury and more migratory than the CNTF counterpart; however, whether
713 this response is protective or deleterious to neurons is a question that will require further
714 investigation.

715

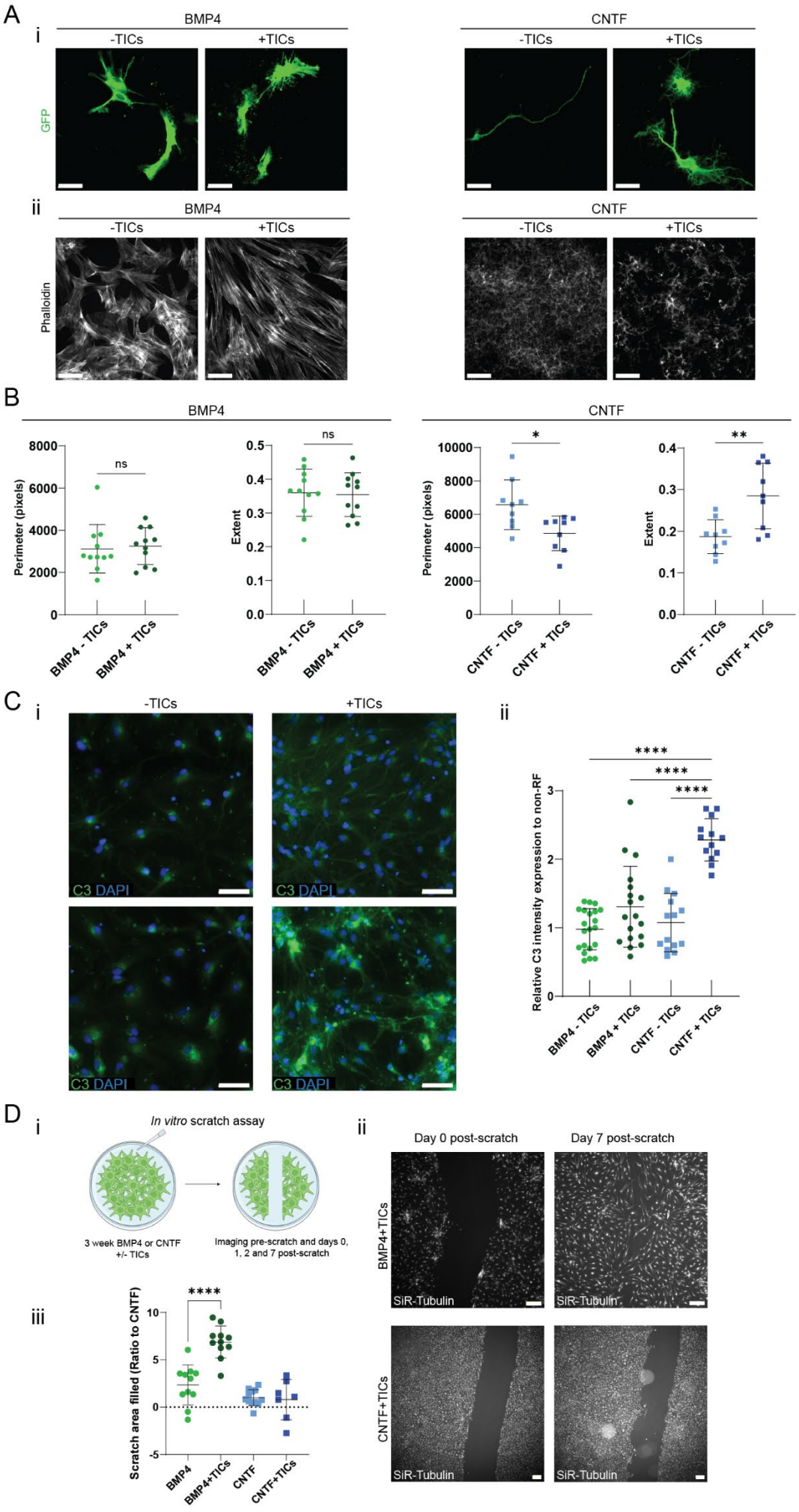
A
i
BMP4
-TICs
+TICs
CNTF
-TICs
+TICs
GFP
ii
BMP4
-TICs
+TICs
CNTF
-TICs
+TICs
Phalloidin
B
BMP4
CNTF
Perimeter (pixels)
Extent
ns
*
**
BMP4 - TICs
BMP4 + TICs
CNTF - TICs
CNTF + TICs
C
i
-TICs
+TICs
C3 DAPI
ii
Relative C3 intensity expression to non-RF
****
D
i
In vitro scratch assay
3 week BMP4 or CNTF +/- TICs
Imaging pre-scratch and days 0, 1, 2 and 7 post-scratch
ii
Day 0 post-scratch
Day 7 post-scratch
BMP4+TICs
CNTF+TICs
SiR-Tubulin
iii
Scratch area filled (Ratio to CNTF)
BMP4
BMP4+TICs
CNTF
CNTF+TICs

716 ***Figure 9 – BMP4 and CNTF acquire distinct reactive phenotypes when treated with***
717 ***inflammatory stimuli.*** *A) Representative images of BMP4 and CNTF astrocytes cultured for*
718 *an additional week in the absence (-TIC) or presence (+TIC) of reactivity inducing factors (TIC;*
719 *TNF, IL-1α, C1q). GFP⁺ astrocytes (i) (green) were used to visualise a change in overall cell*
720 *shape, whilst non-transfected astrocytes were immunostained with phalloidin (ii) to visualize*
721 *actin organization at the population level. Scale bar: 100 µm. B) Quantification of changes in*
722 *GFP shape in BMP4 and CNTF astrocytes in the presence or absence of reactivity factors (-*
723 *TIC and +TIC, respectively). Unpaired t-test to test for significance. Data represents technical*
724 *replicate well averages of astrocytes from two control lines from two independent experiment*
725 *blocks (n=9-11 wells) mean ± S. **p<0.01, *p<0.05, ns: non- significant. C) (i) Representative*
726 *images of BMP4 and CNTF astrocytes cultured for an additional week in the absence (-TIC)*
727 *or presence (+TIC) of reactivity inducing factors (TIC; TNF, IL-1α, C1q) immunostained with*
728 *nuclear marker (DAPI) and Complement Component 3 (C3) to assess C3 protein changes*
729 *upon reactivity induction. Scale bar: 100 µm. (ii) Quantification of C3 intensity per field of view*
730 *normalised to median of non-reactive (non-TIC) control for each cytokine group. Ordinary one-*
731 *way ANOVA with Šídák's multiple comparisons to test for significance. Data represents fields*
732 *of views from two control lines from two independent experiment blocks (n=13-21 f.o.v.'s) mean*
733 *± SD. ****p<0.0001. D) (i) Schematic of experimental protocol for in vitro scratch assay of*
734 *differentiated astrocytes. (ii) Representative images of the scratch area of reactive BMP4*
735 *(BMP4+TIC) and reactive CNTF (CNTF+TIC) immediately after scratch and 7 days after*
736 *scratch. Scale bar: 200 µm. (iii) Quantification of astrocyte wound healing response expressed*
737 *as percentage of scratch area filled at day 7 compared to day 0 for both the cytokine groups*
738 *+/- reactivity factors (TICs) and normalized to CNTF. Ordinary one-way ANOVA with Tukey's*
739 *multiple comparisons to test for significance. Data represents well averages from two control*
740 *lines from two independent experiment blocks (n=8 wells/condition) mean ± SD. ****p<0.0001.*

741

742 **Discussion**

743 Morphology has long been recognized as a fundamental property of astrocytes, contributing
744 to their ability to contact their targets and carry out their modulatory functions in a co-ordinated
745 manner. Many recent studies have contributed to mapping the vast heterogeneity of forms and
746 functions that different subtypes of astrocytes acquire in the human brain[65–67], and the use of
747 human astrocytes *in vitro* for neurobiology and neurodegeneration studies has grown
748 steadily[68,69]. However, morphological diversity has been rarely recapitulated in *in vitro* models,
749 which generally have either one fixed shape, or present a great variability of morphologies
750 across different experiment, lines and laboratories.

751 Here we describe how to obtain morphologically distinct human astrocyte subtypes *in vitro*
752 from iPSCs with defined differentiation protocols and show how these represent an ideal
753 platform to systematically explore the mechanistic links between astrocyte morphology and
754 their function.

755 We first show how exposure of human glial restricted progenitors to either CNTF or BMP4
756 based differentiation media leads to differentiation of astrocyte populations that exhibit all the

757 functional characteristics of mature astrocytes (e.g. glutamate uptake, promotion of synapse
758 formation, intercellular calcium waves, response to reactivity induction) but are fundamentally
759 different in their overall cellular morphology. We developed and employed an unbiased image
760 analysis pipeline to perform a morphological analysis of the salient features that define each
761 subtype, which would also be adaptable in the future for a wider study on different cytokine
762 combinations. Importantly, we show that the morphology acquired is not dependent on
763 medium exposure after initial commitment and cannot be easily switched from one subtype to
764 the other. Moreover, we show that the difference in astrocyte shape correlates with distinct
765 functional profiles and – importantly – is attributable to the reliance of the two subtypes on
766 different elements of the cytoskeleton to acquire and retain their shape.

767 Our results indicate that the distinct organization and usage of the actin and tubulin
768 cytoskeleton not only directly underlies the morphological difference, but also provides a
769 mechanistic link between the structural and functional profiles of astrocytes. For example, we
770 show that CNTF astrocytes have faster and more frequent calcium waves, which travel
771 through their intricate arborised long processes; this would also imply the need for a more
772 structured way of meeting metabolic demands within those processes, which matches our
773 results showing that mitochondria in CNTF astrocytes are more delocalised and actively
774 transported in the processes. In turn, this also correlates with the reliance of CNTF astrocytes
775 on a stable microtubule cytoskeleton, and the upregulation of microtubule related stabilisers
776 and transporters. Correspondingly, for BMP4 astrocytes, we find the morphological data (i.e.
777 multiple dynamic short processes) correlates with the cytoskeleton analysis (i.e. reliance on
778 actin filaments more than microtubules), which is consistent with both the expression profile
779 and – importantly – the cellular function (e.g. migratory behavior in response to reactivity).

780 One important aspect of this study that further highlights the need to consider shape-function
781 links in the context of *in vitro* modelling of astrocytes, is the striking difference in the reactivity
782 profile of the two astrocyte subtypes. When exposed to reactivity inducing cytokines[63], both
783 subtypes strongly upregulated reactivity associated gene families, albeit with subtle
784 differences. Both subtypes also changed their morphology, with CNTF acquiring a more
785 ramified morphology with bigger cell bodies, while reactive BMP4 astrocytes featured a
786 polarised, palisading morphology. It is interesting to note that genes coding for matrix
787 metalloproteinase (MMPs) enzymes appear among the most differentially expressed in both
788 transitions from progenitors to differentiated cells (for example *MMP3* for BMP4, *MMP8* for
789 CNTF), as well as in the transition between untreated and treated CNTF astrocytes (*MMP3*),
790 potentially pointing towards an important role of ECM remodelling in driving this process
791 (**Figure 4C-D and Figure 7C**).

792 The most striking feature we observed was the opposite behavior these reactive astrocytes
793 have in response to injury, with the reactivity response of BMP- and CNTF-differentiated
794 astrocytes to the well-defined TIC neurotoxicity-inducing cytokines being markedly different.

795 While our results highlight the links between shape, function and reactivity in human astrocyte,
796 our *in vitro* model is by its nature reductionist and more simplified compared to the *in vivo*
797 setting. On the one hand, this allows us to retain a much higher level of control on each
798 separate component that might influence astrocyte shape and function, but on the other, there
799 are important non-cell autonomous and environmental effects that we cannot fully account for.
800 Firstly, our astrocytes are differentiated and grown in isolation, while *in vivo* astrogenic signals
801 and other cues would be derived from the surrounding neuronal populations[70]. This means
802 that our analysis, except in the case of specific co-culture experiments, does not account for
803 the presence of neurons and other glial cells that are known to modulate the activity of
804 astrocytes[71], so we cannot account for potential regional and subtype specific developmental
805 cues that might be missing from our culture.

806 Comparison of our *in vitro* BMP- and CNTF-differentiated astrocyte RNA-seq data with other
807 published human adult brain astrocyte datasets[41,42] indicated that both astrocyte subtypes
808 exhibited a degree of transcriptional similarity with acutely purified human brain astrocytes. Of
809 note, similarities were additionally observed with vascular smooth muscle cells (SMCs) and
810 fibroblasts for BMP4-astrocytes and ependymal cells for CNTF-astrocytes. This may be due
811 to overlap between pathways activated by BMP4 and CNTF that are also upregulated in these
812 cell types, such as ECM component secretion and modelling by fibroblasts[72] activated by
813 BMP4, and cilium regulation and movement by ciliated ependymal cells[73] also activated by
814 CNTF. For this comparison, we used single-cell RNA-seq datasets, which may be an additional
815 caveat in a comparative analysis with the bulk RNA-seq generated in this study – as they
816 provide lower sequencing depth. Taken together, this validates the signature of our *in vitro*
817 generated astrocyte subtypes as *bona fide* human astroglia, while further supporting the idea
818 that each subtype displays unique transcriptional features which are consistent with our
819 morphological and functional analyses.

820 To further scrutinize the *in vitro* validity of our human astrocyte model, we also investigated
821 the effects of BMP4 and CNTF on primary isolated mouse neocortical astrocytes[44]. Based on
822 morphological and transcriptomic analyses, the growth factors had similar effects on the
823 mouse astrocytes. CNTF drove a similar transcriptomic profile in mouse astrocytes as HBEGF,
824 the gold standard for *in vitro* rodent astrocyte culture, while BMP4-treated mouse astrocytes
825 displayed extensive gene expression differences from both CNTF- and HBEGF-treated
826 astrocytes. When comparing enriched gene sets, we also found similarities between

827 astrocytes differentiated from human and mouse. CNTF-treated astrocytes were enriched for
828 pathways associated with cilium and microtubule movement. BMP4-treated astrocytes were
829 interestingly enriched for ECM regulation, a known function of astrocytes (reviewed in Wiese
830 et al[74]). Taken together, our investigation of rodent astrocytes revealed commonalities in BMP4
831 and CNTF signaling, further validating our human astrocyte *in vitro* model and the differential
832 effect that CNTF and BMP4 have on astrocytes. It is also important to note that other
833 combinations of cytokines have been shown to have different degrees of potency in driving
834 astrogliogenesis *in vitro*[70] , however, to our knowledge there are no systematic reports on their
835 effect on astrocyte morphology.

836 Another important caveat of our approach is that most of our experiments are performed in
837 2D and on ECM-coated tissue culture plastic, therefore our cells lack the tri-dimensional
838 structure they would have *in vivo*, and they adhere to a substrate with a much higher stiffness
839 than the physiological range. Future studies should address these limitations and test if and
840 how the observed phenotypes translate in a 3D environment.

841 In conclusion, we report an important step in demonstrating the key links between shape and
842 function in astrocyte cultures, and how including cell shape dynamics within *in vitro* modelling
843 approaches for astrocytes could be highly beneficial to better recapitulate human astrocyte
844 biology in health and disease. We show that different morphogens drive transcriptomic,
845 morphological, and functional differences in human astrocytes, and provide evidence that they
846 respond differently to the same reactivity inducing factors – a long-standing question in the
847 field of astrocyte biology. Moving forward, it will be compelling to discern what other astrocyte
848 differentiation factors may alter astrocyte morphologies and importantly impact how these
849 subtypes of cells function and respond to stimuli in the human adult brain.

850

Supplementary information

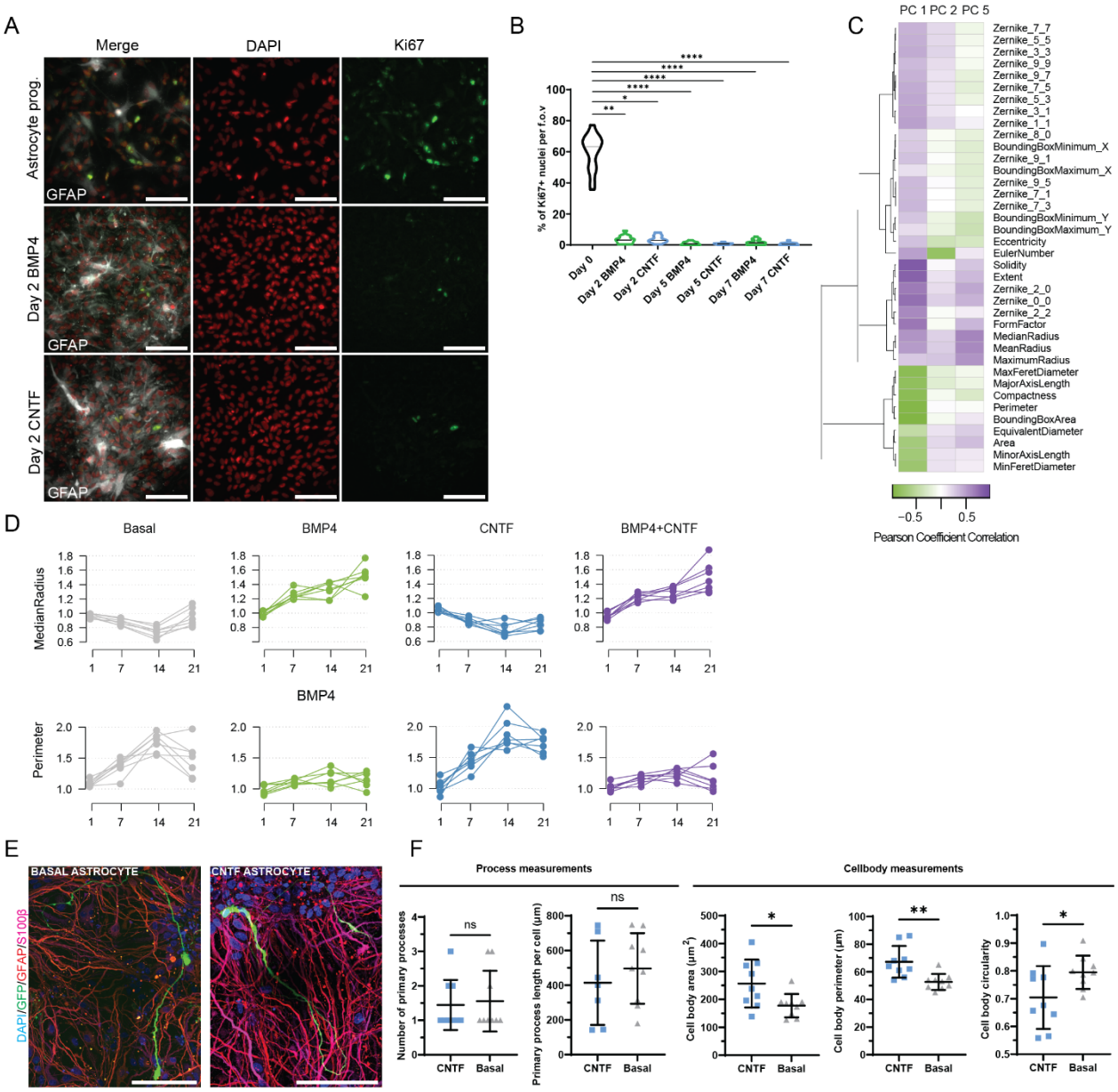

Figure 1 (supplementary) *- A) Representative images of astrocytes stained at multiple stages of differentiation with DAPI for nuclei detection and Ki67 for proliferating cells. (B) Quantification of DAPI/Ki67+ astrocytes from Day 2 to Day 7 of differentiation. Data from one control line within one experimental block of 6-10 technical well replicates, expressed as median ± IQR. Kruskal-wallis test with Dunn's multiple comparisons to test significance. ****p<0.0001, ***p<0.001, **p<0.01, *p<0.05. Scale bar: 100 µm. C) Pearson correlation coefficients for principal components clustered according to shape descriptors. Purple indicates positive correlations whilst green indicates negative correlations. D) Plots of key shape descriptors changing over time for the different cytokine groups basal, BMP4, CNTF and BMP4 plus CNTF. Data points are averages of wells from one control line in one experimental block with seven technical replicates (n=7 wells). E) Representative fluorescent images of basal and CNTF differentiated astrocytes labelled with nuclear marker (DAPI), GFP and astrocyte differentiation markers (GFAP, S100β). Scale bar: 100 µm. F) Quantification of*

866 *process and cell body measurements in basal and CNTF differentiated astrocytes. Data points*
867 *represent single cells (n=7-9 cells) from one control line in one experimental block from three*
868 *technical replicates, mean ± SD. Unpaired t-tests and Mann-Whitney test (number of*
869 *processes quantification) was used to test significance ****P<0.0001, ***P<0T.001, **P<0.01,*
870 **P<0.05, ns: non-significant.*

871

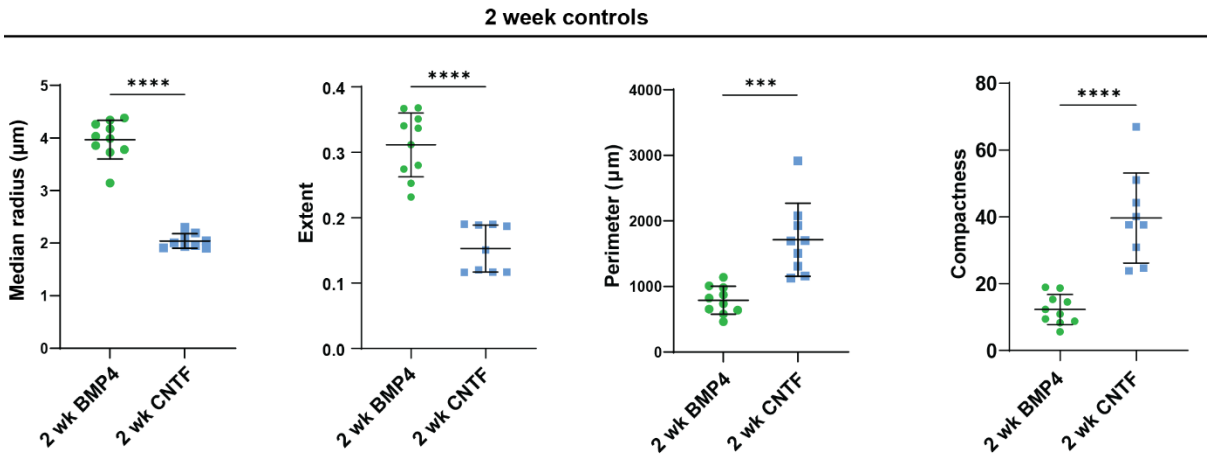

872

873 ***<u>Figure 2 (supplementary) -</u>*** *Quantification of key shape descriptors in BMP4 and CNTF*
874 *differentiated astrocytes, used as a control for cytokine switching experiments. One-way*
875 *ANOVA or Kruskall-Wallis test with Dunn's multiple comparisons to test for significance*
876 *between switched and non-switched pairs. Data represents technical replicate well averages*
877 *of astrocytes from two control lines from two independent experiment blocks (n=7-9 wells)*
878 *mean ± SD. ****p<0.0001, ***p<0.001, **p<0.01, *p<0.05, ns: non-significant. B+B: BMP4 +*
879 *BMP4; B+C: BMP4 + CNTF; C+C: CNTF + CNTF; C+B: CNTF + BMP4.*

880

881

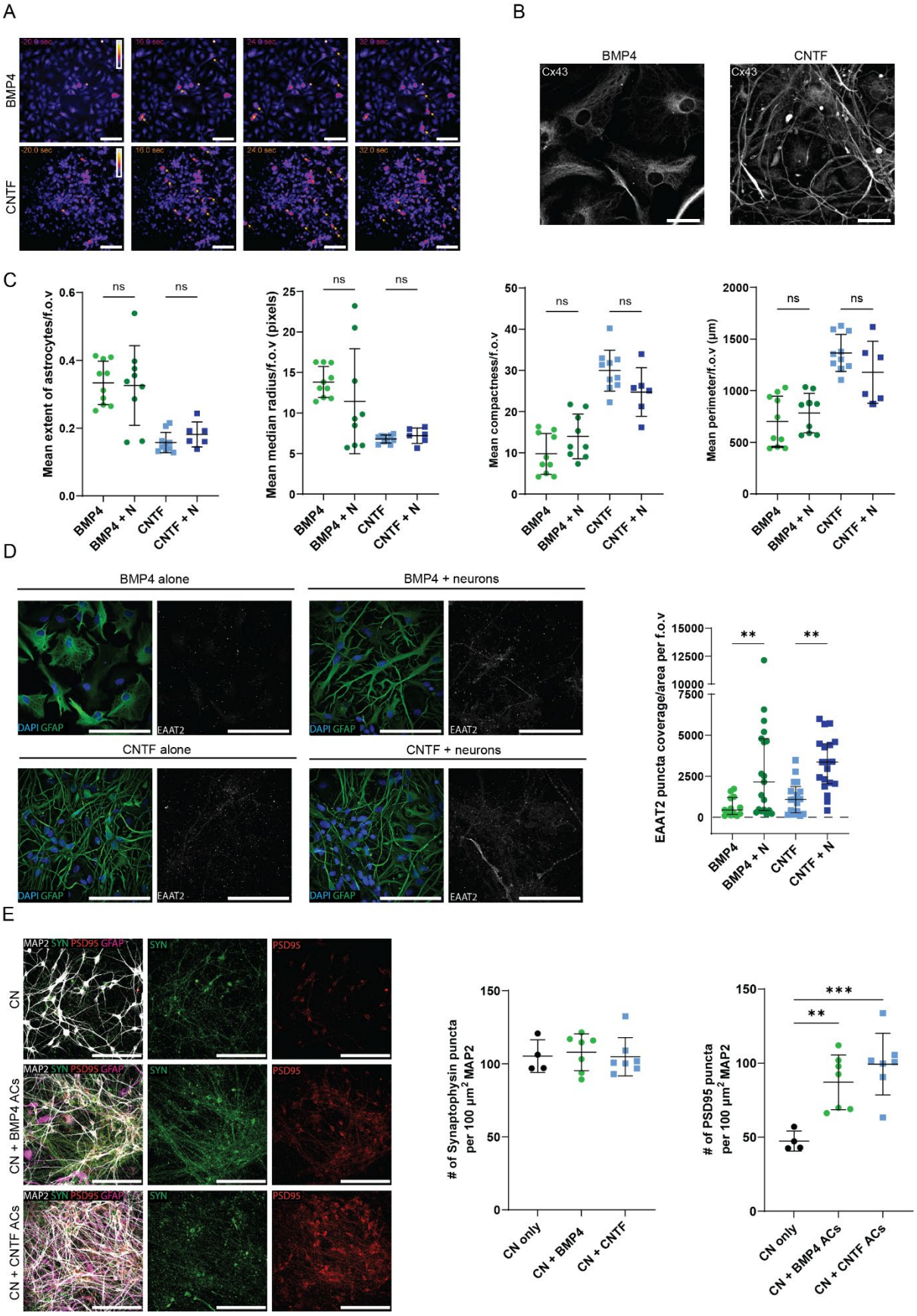

Figure 3 (supplementary) - *A) Example time lapse images of astrocytes labelled with Fluo4-AM and stimulated with ATP to initiate ATP-responsive calcium waves. Yellow arrows indicate*

885 *astrocytes which show a peak in their fluorescence intensity during the imaging period,*
886 *indicating calcium spiking behaviour. B) Representative images of BMP4 and CNTF*
887 *astrocytes immunostained for connexin 43 (CX43). Scale bar: 25 µm. C) Quantification of*
888 *astrocyte morphology with and without neuronal co-culture (BMP4+N: BMP4 plus neurons;*
889 *CNTF+N: CNTF plus neurons) from GFP^{+} astrocytes. One way ANOVA or Kruskal-Wallis with*
890 *Šídák's multiple comparisons to test for significance between BMP4 astrocytes +/- neurons*
891 *and CNTF astrocytes +/- neurons. Data points represent well averages of two control lines*
892 *from two experimental blocks with 6-9 technical replicates (n = 6-9 wells), mean ± SD, ns: non-*
893 *significant. Scale bar: 100 µm. D) Representative fluorescent images of BMP4 and CNTF*
894 *astrocytes either cultured alone or in the presence of differentiated human stem-cell derived*
895 *motor neurons and labelled with nuclear (DAPI), intermediate filament (GFAP) and glutamate*
896 *transporter markers (EAAT2). Scale bar: 100 µm. Quantification of EAAT2 puncta coverage*
897 *per unit area in the absence or presence of motor neurons was performed. Data points*
898 *represent field of views from two control lines from two experimental blocks with six technical*
899 *replicates (n = 15-18 fields of view (f.o.v)). One-way ANOVA with Šídák's multiple comparisons*
900 *to test for significance between BMP4 astrocytes +/- neurons and CNTF astrocytes +/-*
901 *neurons, mean ± SD, **p<0.01. E) images of cortical neurons cultured alone (CN or in the*
902 *presence of BMP4 (CN+BMP4 ACs) or CNTF (CN+CNTF ACs) astrocytes. Cortical neurons*
903 *were stained for dendrites (MAP2) and pre- and post- synaptic elements with synaptophysin*
904 *(SYN) and postsynaptic density-95 (PSD95), respectively. BMP4 and CNTF astrocytes were*
905 *stained for their intermediate filaments (GFAP). Quantification of the number of SYN and*
906 *PSD95 puncta per 100 µm^{2} MAP2 positive dendrite areas was performed comparing cortical*
907 *neurons cultured alone (CN only) or in the presence of BMP4 (CN+BMP4 ACs) or CNTF*
908 *(CN+CNTF ACs) astrocytes. Datapoints represent well averages of two control lines (for*
909 *astrocytes) for two experimental blocks with 4-8 technical replicates (n=4-8 wells). One-way*
910 *ANOVA with Dunn's multiple comparisons to test for significance, mean ± SD, ***p<0.001,*
911 **p<0.05.*

912

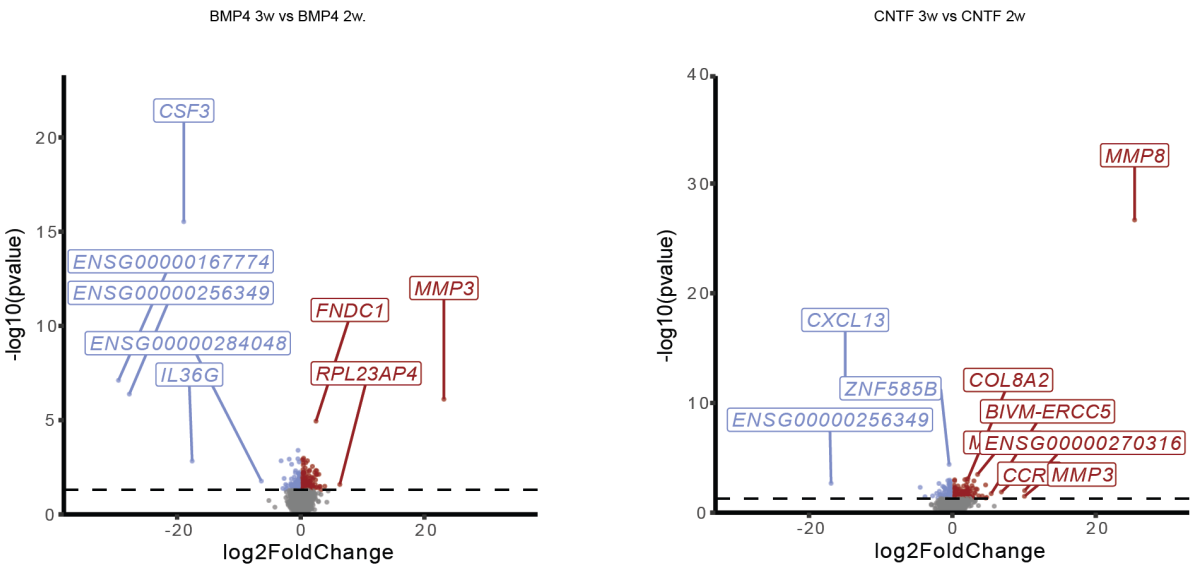

Figure 4 (supplementary) *- Pairwise comparison volcano plots for 3-week differentiated BMP4 astrocytes versus 2-week differentiated BMP4 astrocytes and 3-week differentiated CNTF astrocytes versus 2-week differentiated CNTF astrocytes.*

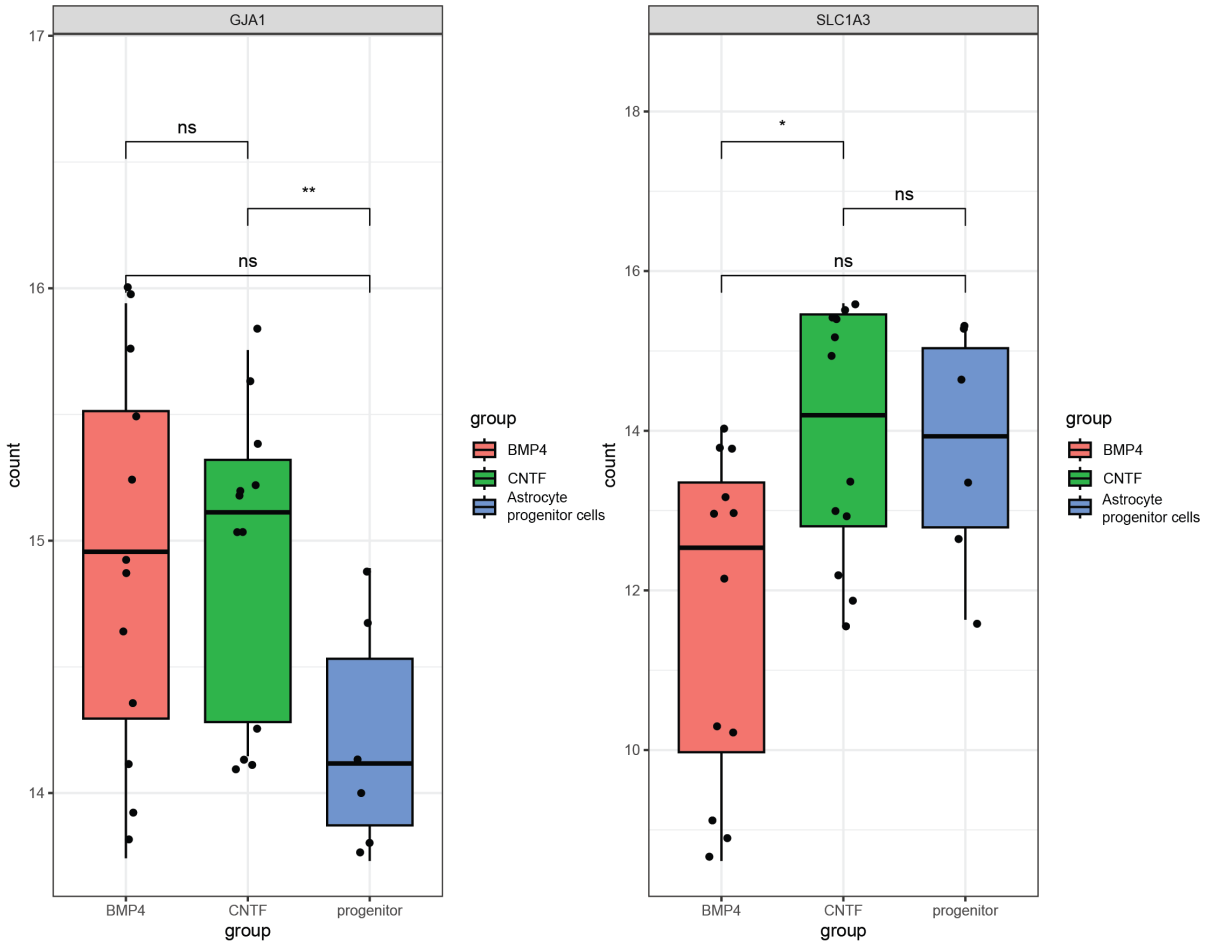

919 ***Figure 5 (supplementary) –*** *Box plots comparing the transformed expression counts of GJA1*
920 *(which encodes for CX43) and SLC1A3 (which encodes for EAAT1) between BMP4*
921 *differentiated astrocytes, CNTF differentiated astrocytes and astrocyte progenitor cells.*
922 *Statistical significance for pairwise comparisons derived using Wilcoxon test (**p<0.01,*
923 **p<0.05, ns: non-significant)*

924

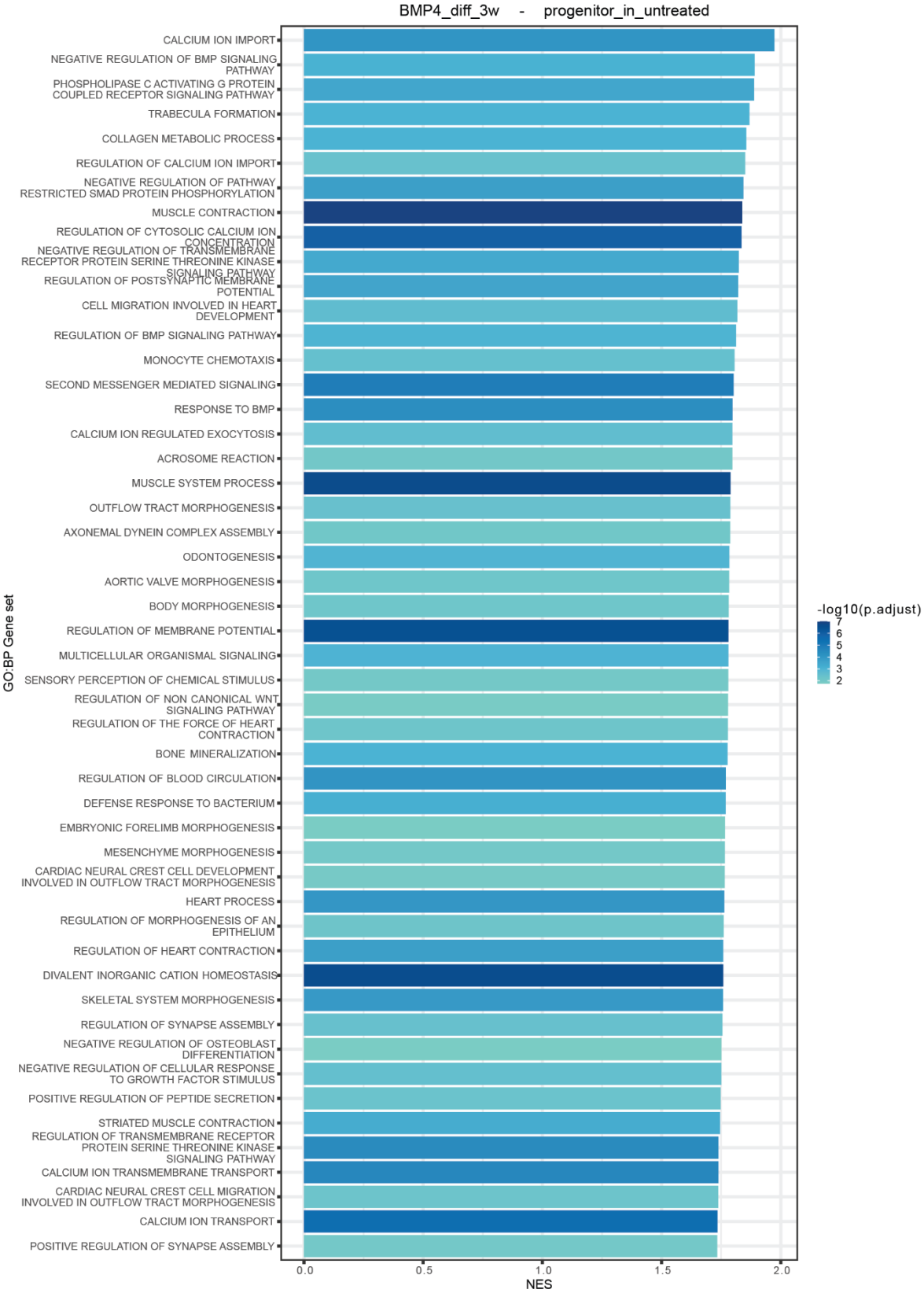

Figure 6 (supplementary) *– Bar plot showing top 50 gene sets upregulated in BMP4 astrocytes versus astrocyte progenitor cells. Gene sets were derived from the Biological*

Process (BP) ontology. Gene sets are ordered according to the absolute effect size (NES) and colored by significance (-log$_{10}$ p-value adjusted).

931 ***Figure 7 (supplementary)*** – Bar plot showing top 50 gene sets downregulated in BMP4
932 astrocytes versus astrocyte progenitor cells. Gene sets were derived from the Biological
933 Process (BP) ontology. Gene sets are ordered according to the absolute effect size (NES)
934 and coloured by significance (-$\log_{10}$ p-value adjusted).

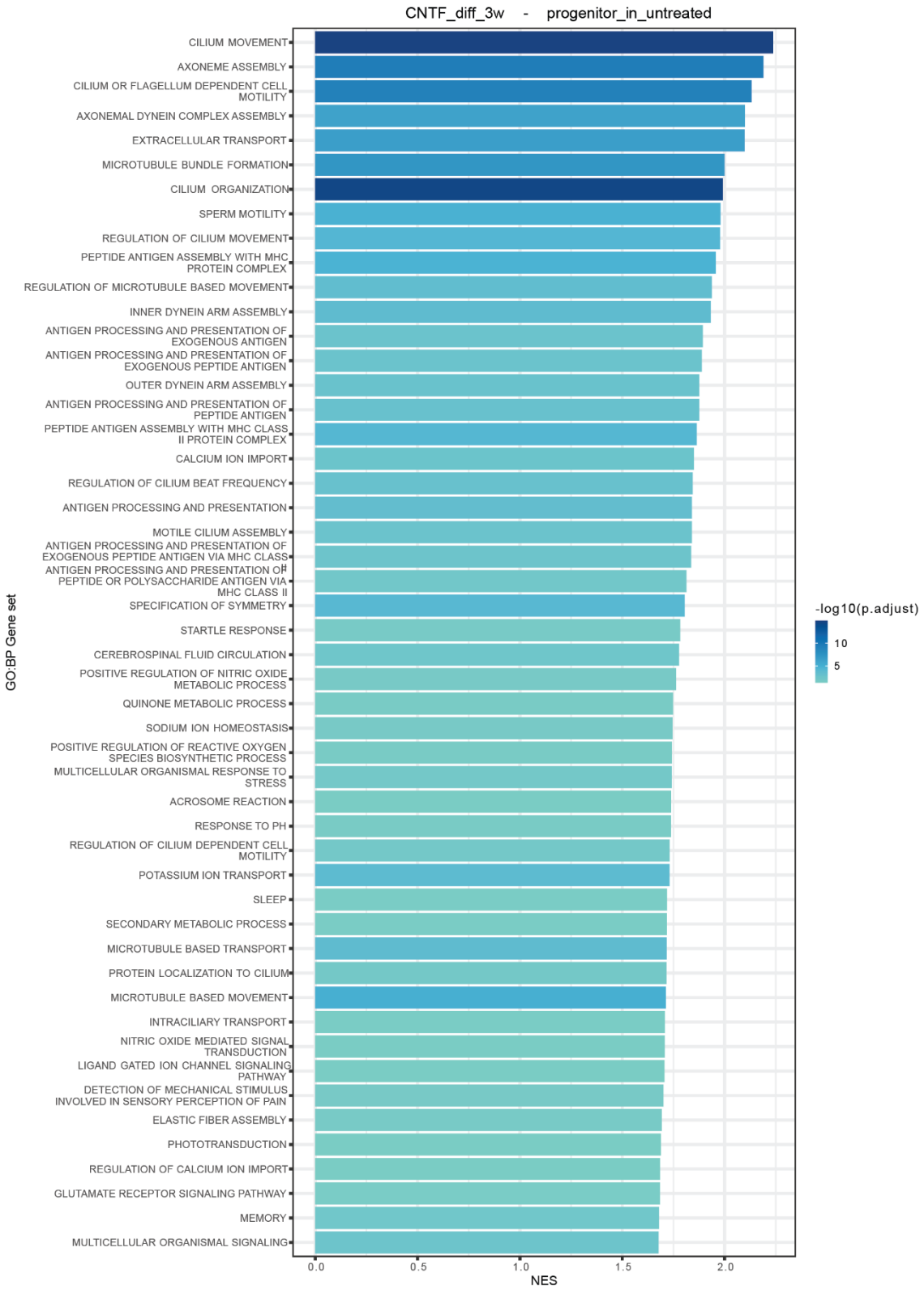

935

936 ***Figure 8 (supplementary)*** *– Bar plot showing top 50 gene sets upregulated in CNTF*
937 *astrocytes versus astrocyte progenitors. Gene sets were derived from the Biological Process*
938 *(BP) ontology. Gene sets are ordered according to the absolute effect size (NES) and colored*
939 *by significance (-log$_{10}$ p-value adjusted).*

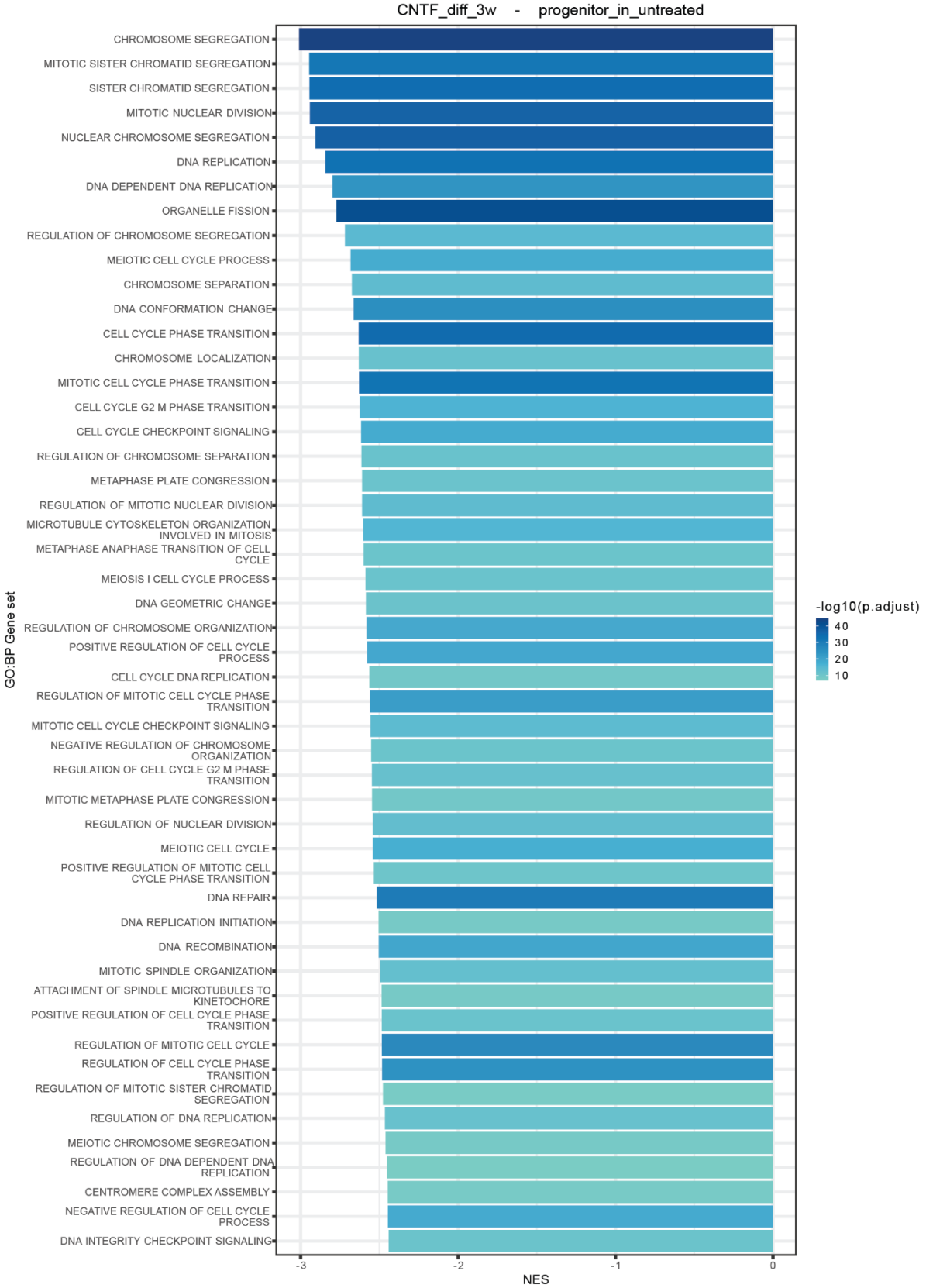

940 ***Figure 9 (supplementary)*** *– Bar plot showing top 50 gene sets downregulated in CNTF*
941 *astrocytes versus astrocyte progenitors. Gene sets were derived from the Biological Process*
942 *(BP) ontology. Gene sets are ordered according to the absolute effect size (NES) and colored*
943 *by significance (-$\log_{10}$ p-value adjusted).*

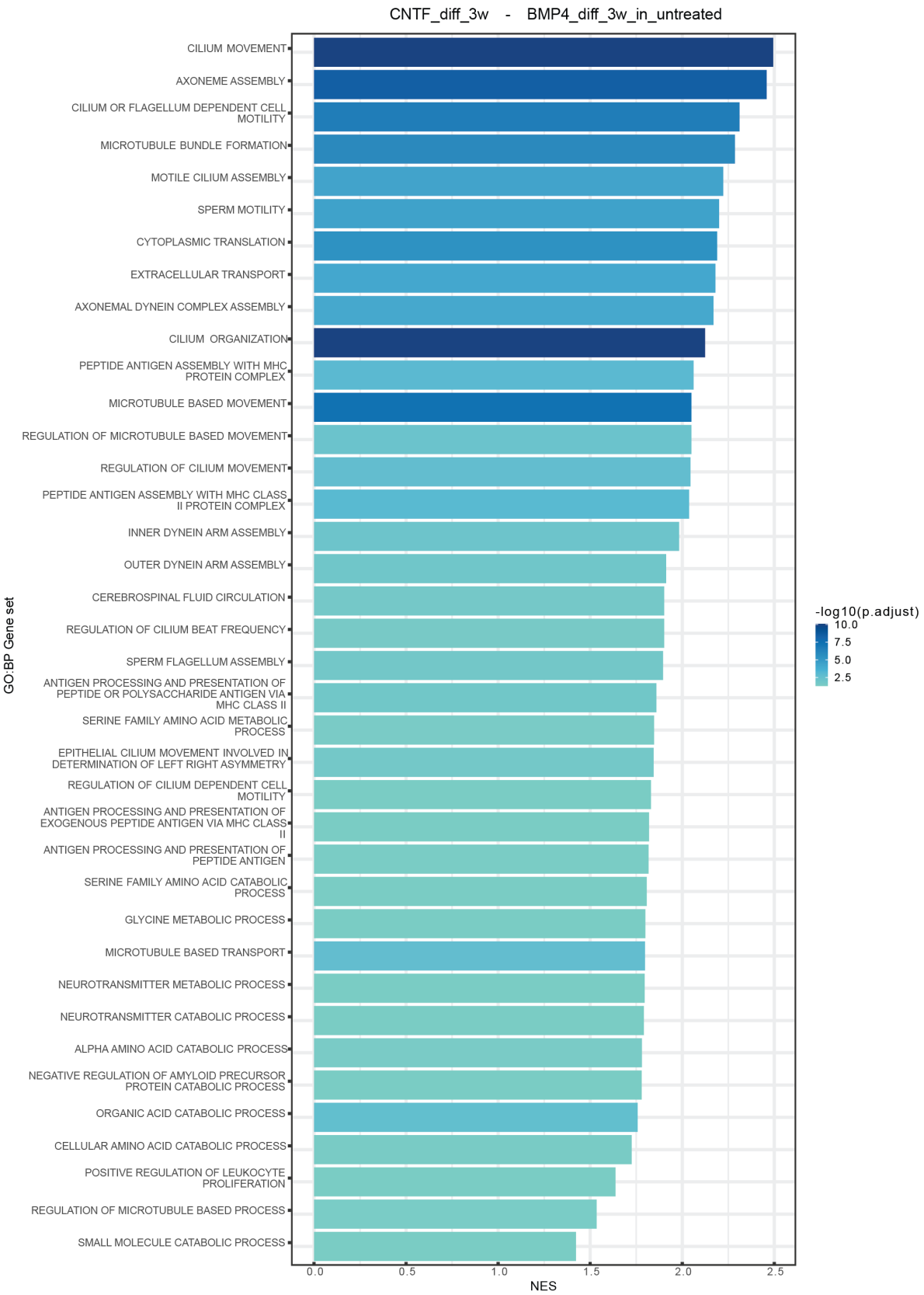

Figure 10 (supplementary) *–Bar plot showing top 50 gene sets upregulated in CNTF astrocytes versus BMP4 astrocytes. Gene sets were derived from the Biological Process (BP)*

947 *ontology. Gene sets are ordered according to the absolute effect size (NES) and colored by*
948 *significance (-log$_{10}$ p-value adjusted).*

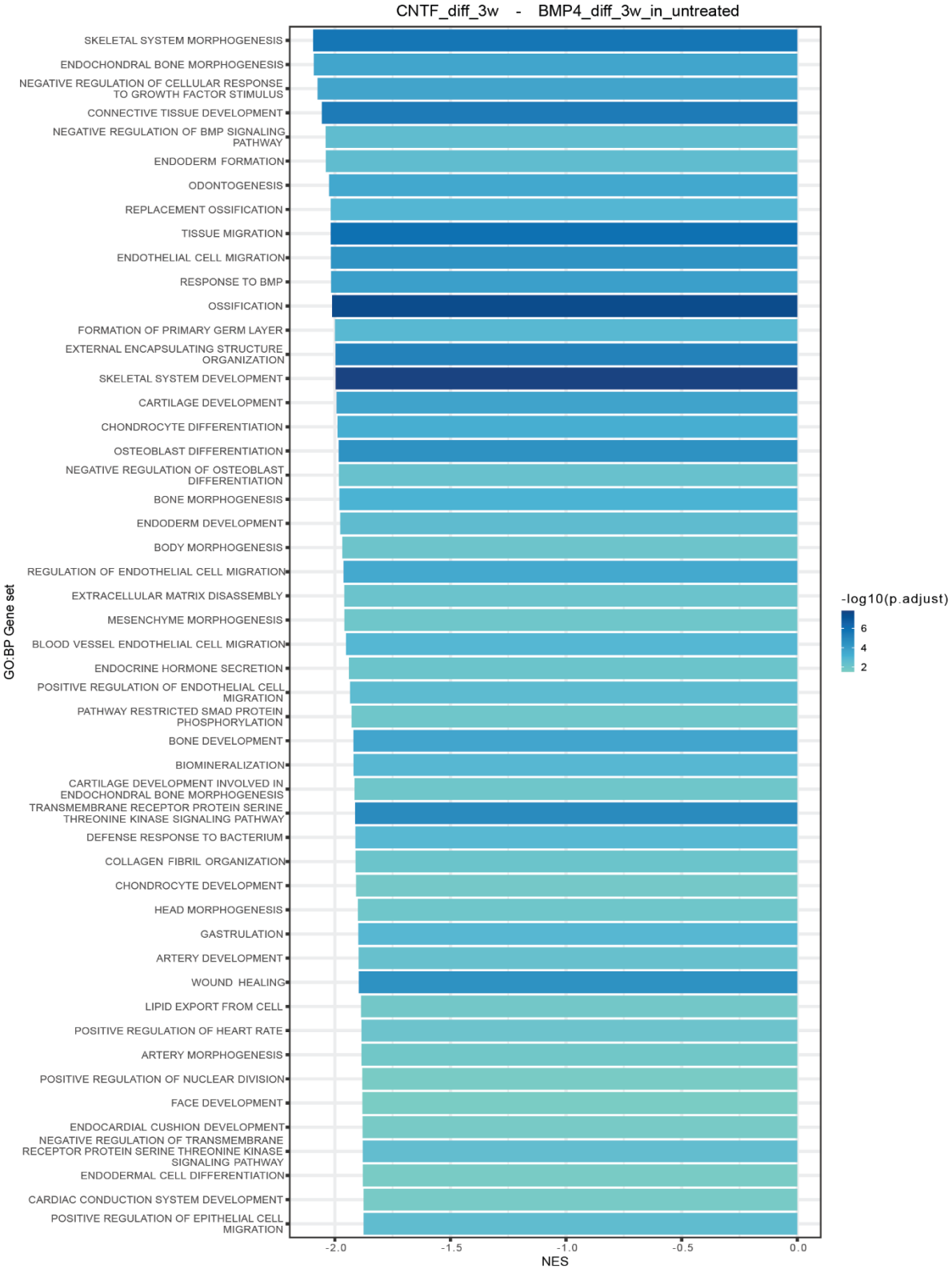

949

950 ***<u>Figure 11 (supplementary)</u>*** *– Bar plot showing top 50 gene sets downregulated in CNTF*
951 *astrocytes versus BMP4 astrocytes. Gene sets were derived from the Biological Process (BP)*

952 *ontology. Gene sets are ordered according to the absolute effect size (NES) and colored by*
953 *significance (-log_{10} p-value adjusted).*

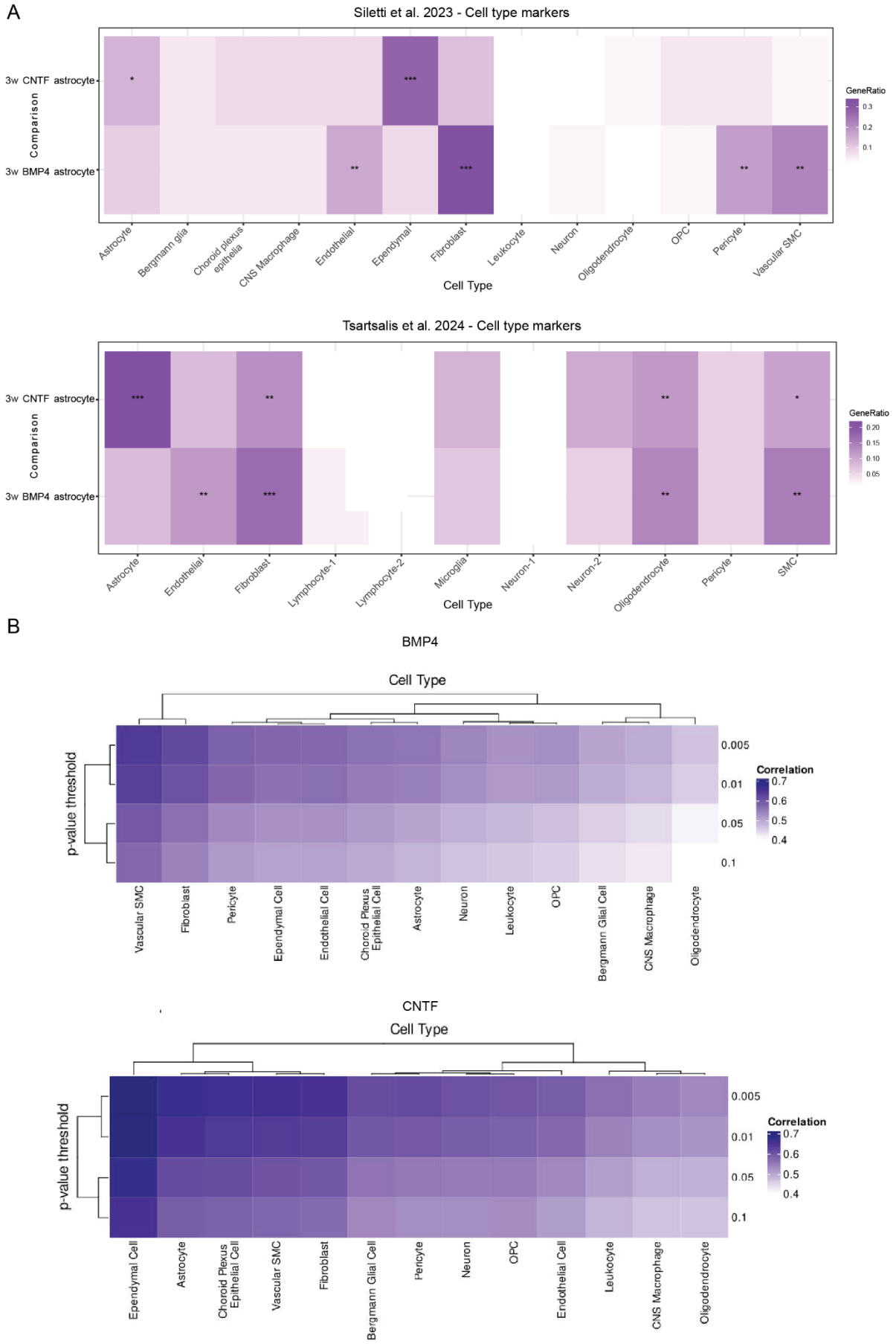

Figure 12 (supplementary) *– A) Comparison between the expression patterns of*

956 *differentiated BMP4 and CNTF astrocytes and cell type markers from Silletti et al, 2023 and*
957 *Tsartsalis et al, 2024. B) Clustered heatmap showing the correlation coefficients (Pearson's r)*
958 *between the effect sizes (log_2FoldChange) of BMP4 or CNTF astrocytes and different cell*
959 *types from Siletti et al, 2023 relative to undifferentiated progenitors at different BMP4- and*
960 *CNTF-differentiated astrocyte DEG adjusted p-value thresholds.*

A

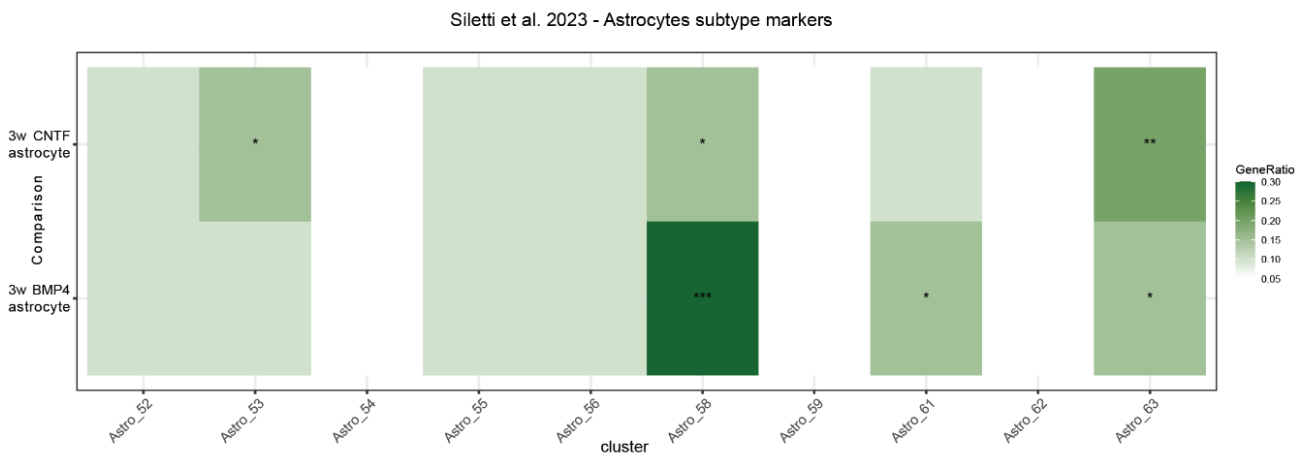
Siletti et al. 2023 - Astrocytes subtype markers
3w CNTF astrocyte
3w BMP4 astrocyte
Comparison
Astro_52
Astro_53
Astro_54
Astro_55
Astro_56
Astro_58
Astro_59
Astro_61
Astro_62
Astro_63
cluster
GeneRatio
0.30
0.25
0.20
0.15
0.10
0.05

B

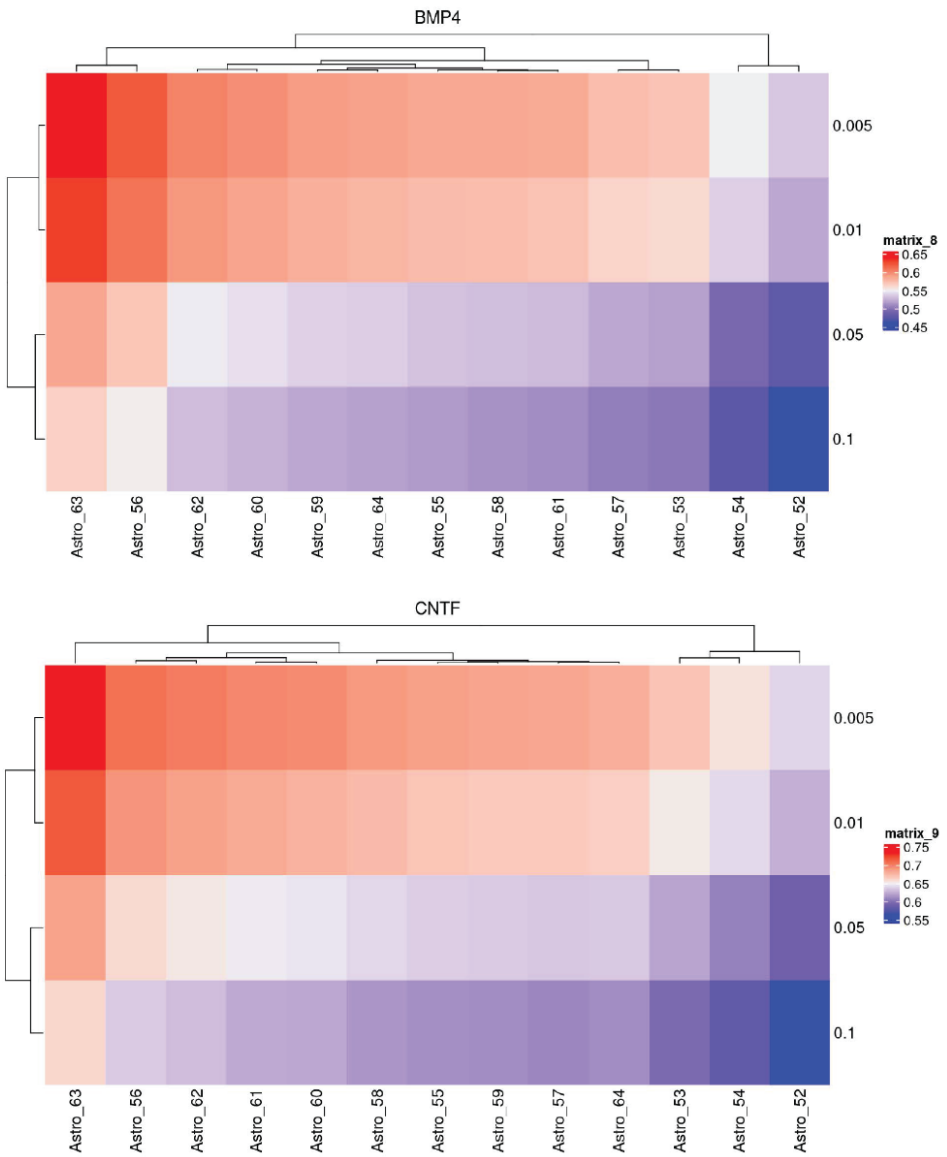
Siletti et al. 2023 - Astrocytes subtype correlation
BMP4
0.005
0.01
0.05
0.1
matrix_8
0.65
0.6
0.55
0.5
0.45
Astro_63
Astro_56
Astro_62
Astro_60
Astro_59
Astro_64
Astro_55
Astro_58
Astro_61
Astro_57
Astro_53
Astro_54
Astro_52
CNTF
0.005
0.01
0.05
0.1
matrix_9
0.75
0.7
0.65
0.6
0.55
Astro_63
Astro_56
Astro_62
Astro_61
Astro_60
Astro_58
Astro_55
Astro_59
Astro_57
Astro_64
Astro_53
Astro_54
Astro_52

963 ***Figure 13 (supplementary)*** *– A) Comparison between the expression patterns of*
964 *differentiated BMP4 and CNTF astrocytes and astrocyte subtype markers from Silletti et al,*
965 *2023. B) Correlation matrices showing the amount of correlation between the expression*
966 *patterns of BMP4 or CNTF astrocytes and different astrocyte subtypes from Silletti et al, 2023*

967

A

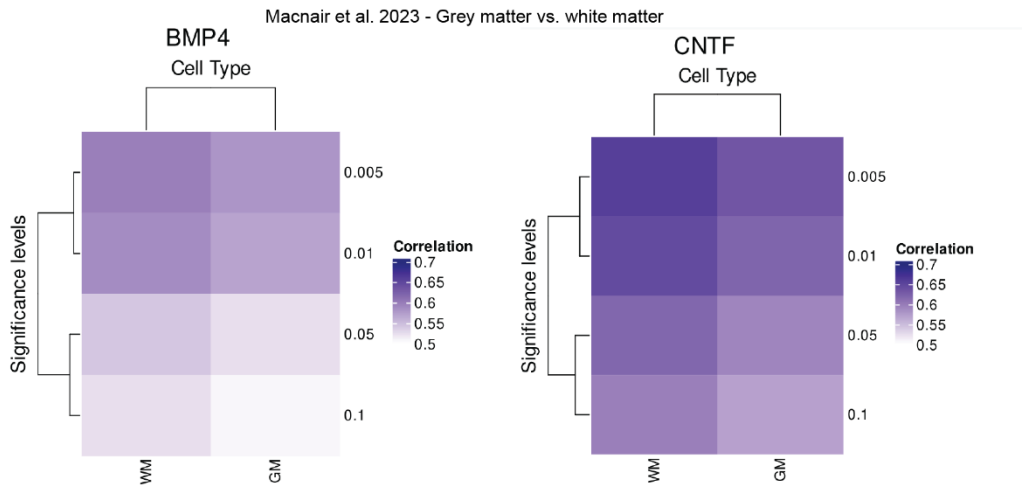
Macnair et al. 2023 - Grey matter vs. white matter
BMP4
Cell Type
CNTF
Cell Type
Significance levels
0.005
0.01
0.05
0.1
Correlation
0.7
0.65
0.6
0.55
0.5
WM
GM

B

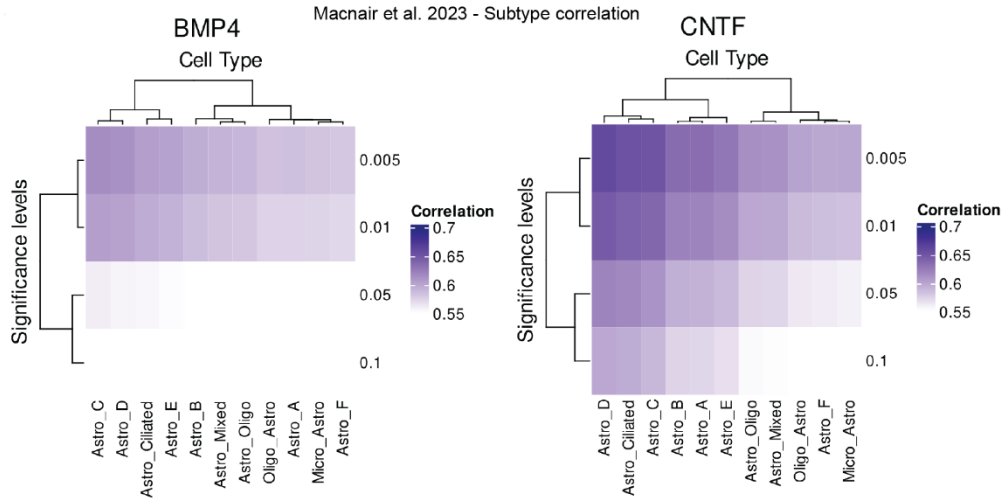
Macnair et al. 2023 - Subtype correlation
BMP4
Cell Type
CNTF
Cell Type
Significance levels
0.005
0.01
0.05
0.1
Correlation
0.7
0.65
0.6
0.55
Astro_C
Astro_D
Astro_Ciliated
Astro_E
Astro_B
Astro_Mixed
Astro_Oligo
Oligo_Astro
Astro_A
Micro_Astro
Astro_F
Astro_D
Astro_Ciliated
Astro_C
Astro_B
Astro_A
Astro_E
Astro_Oligo
Astro_Mixed
Oligo_Astro
Astro_F
Micro_Astro

C

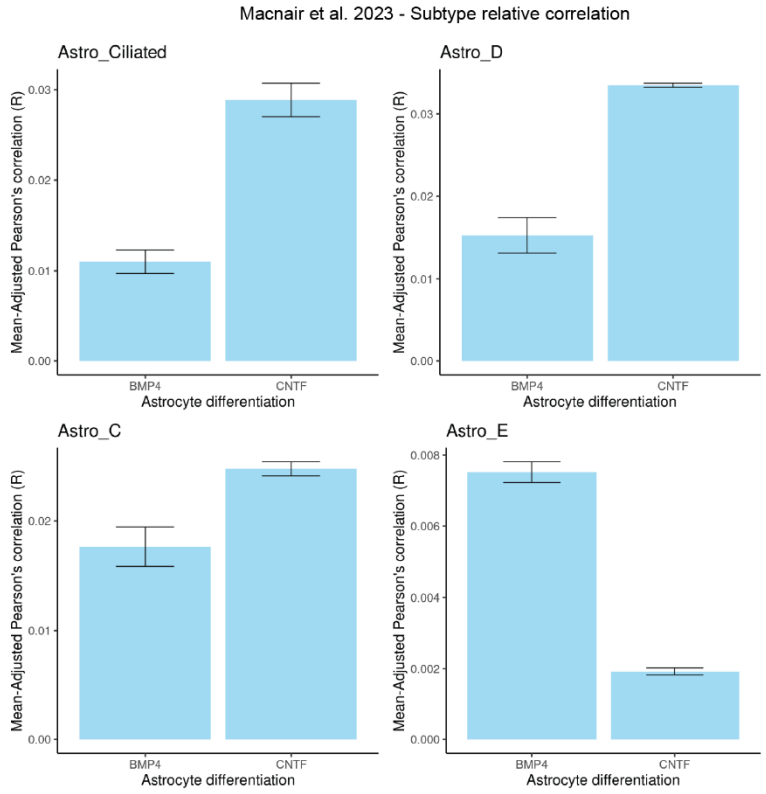
Macnair et al. 2023 - Subtype relative correlation
Astro_Ciliated
Astro_D
Astro_C
Astro_E
Mean-Adjusted Pearson's correlation (R)
BMP4
CNTF
Astrocyte differentiation

968

969 ***Figure 14 (supplementary)*** *- A) Comparison between the expression patterns of*
970 *differentiated BMP4 and CNTF astrocytes and those of white and grey matter astrocytes from*
971 *Macnair et al, 2023. B) Correlation matrices showing the amount of correlation between the*
972 *expression patterns of BMP4 or CNTF astrocytes and different astrocyte subtypes from*
973 *Macnair et al, 2023. C) Bar blots showing the relative correlation between BMP4 and CNTF*
974 *astrocytes and the top subtypes from Macnair et al, 2023.*

975

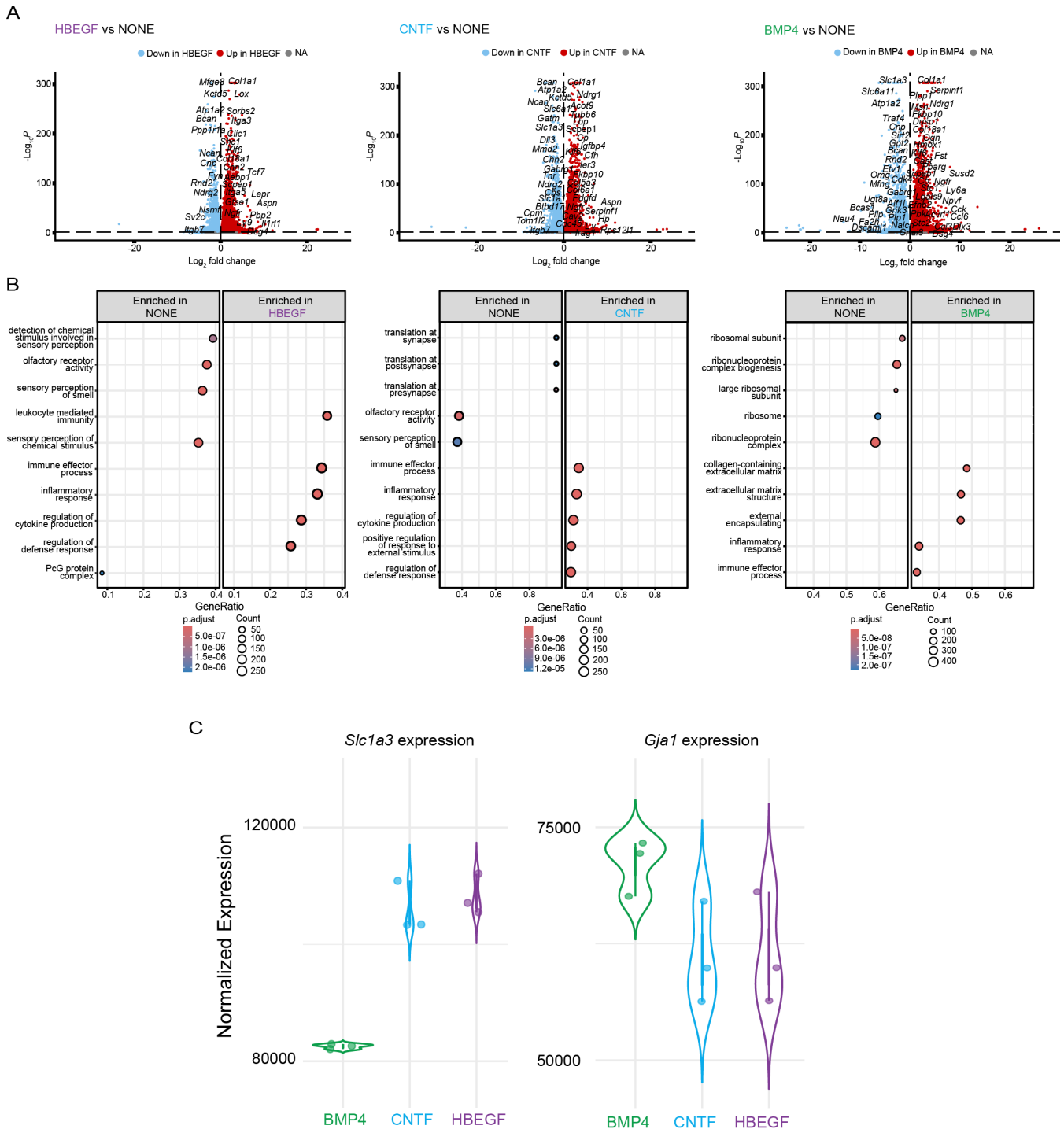

Figure 15 (supplementary) - *A) Volcano plots of differentially expressed genes between respective treatment conditions. Positive log_2 fold change is representative of enrichment while negative log_2 fold change is representative of de-enrichment. B) Dot plotting of GO biological process gene set enrichment. Gene ratio describes the ratio of significantly changed genes to the total genes in each pathway set. Dot size represents the total number of enriched*

983 *or de-enriched genes while color is representative of adjusted p-value. C) Violin plotting of*
984 *individual gene expression across n=3 technical replicates split by treatment condition. Counts*
985 *normalized by DESeq2 median of ratios.*

986

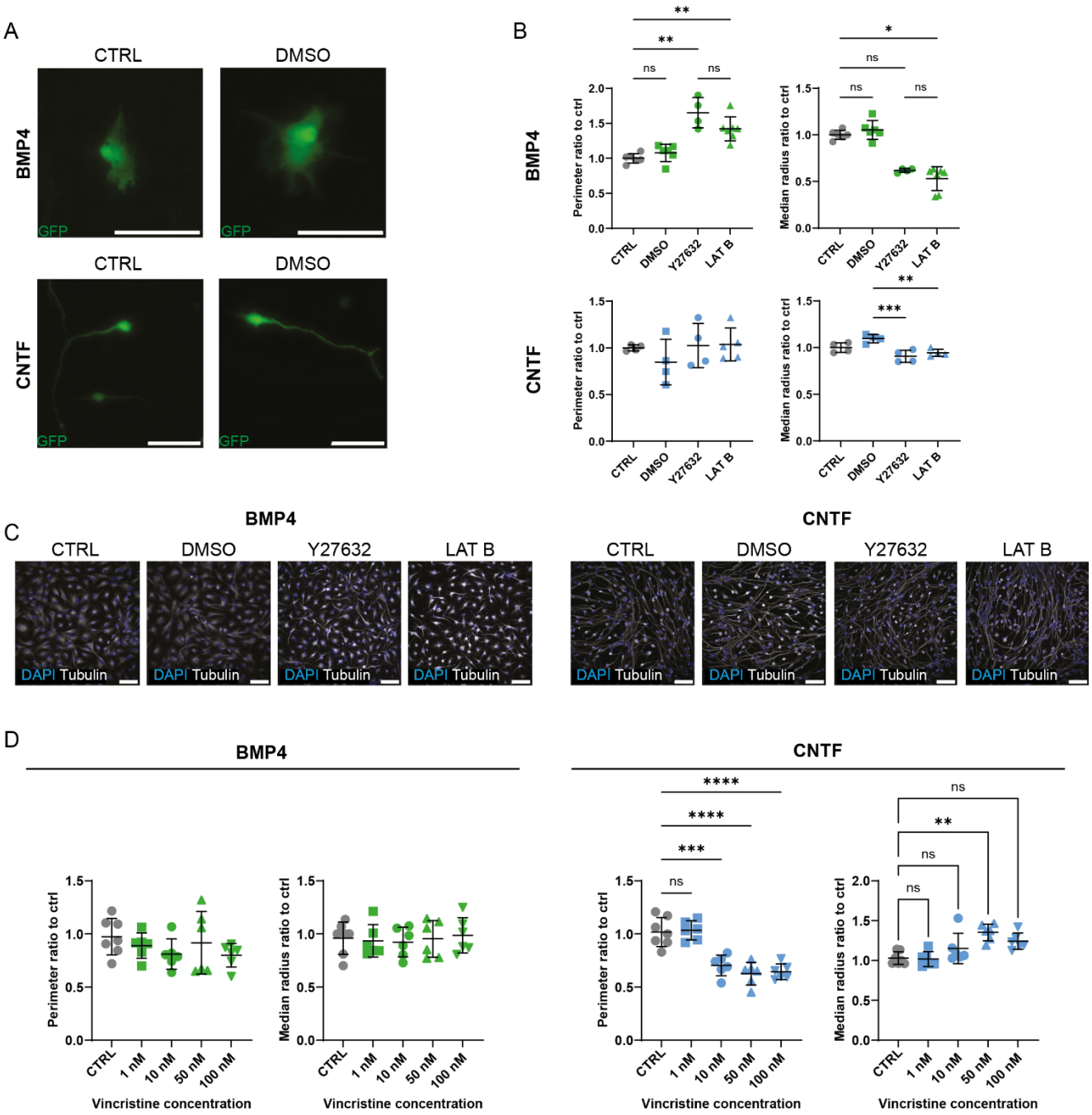

987

988 ***Figure 16 (supplementary)*** *– A) Representative images of GFP⁺ BMP4 and CNTF*
989 *astrocytes, either untreated (CTRL) or treated with vehicle control DMSO. Scale bar: 100 µm.*
990 *B) Quantification of shape changes in the presence of actin inhibitors analysing perimeter and*
991 *median radius expressed as a ratio compared to control (ctrl, black). Data represents well*
992 *averages of technical replicates of two control lines from two experimental blocks (n=4-5 wells*

993 *total), mean ± SD. Ordinary one-way ANOVAs with Tukey's post-hoc was used to test for*
994 *significance. *p<0.05, **p<0.01, ****p<0.0001 ns or no comparisons shown: non-significant.*
995 *C) Representative images of BMP4 and CNTF astrocytes, either untreated (ctrl) or treated*
996 *with actin inhibitors Y27632 dihydrochloride (Y27632; 25 μM) or latrunculin B (LAT B; 1 μM)*
997 *for 2 hours, stained with nuclear (DAPI, blue) and microtubule cytoskeletal markers (Tubulin,*
998 *white). Scale bar: 100 μm. D) Quantification of shape changes in the presence of vincristine*
999 *analysing perimeter and median radius, expressed as a ratio compared to control (ctrl, black).*
1000 *Data represents well averages of technical replicates of two control lines from two*
1001 *experimental blocks (n=6-7 wells total), mean ± SD. Ordinary one-way ANOVAs with Tukey's*
1002 *post-hoc was used to test for significance.*

1003

1004

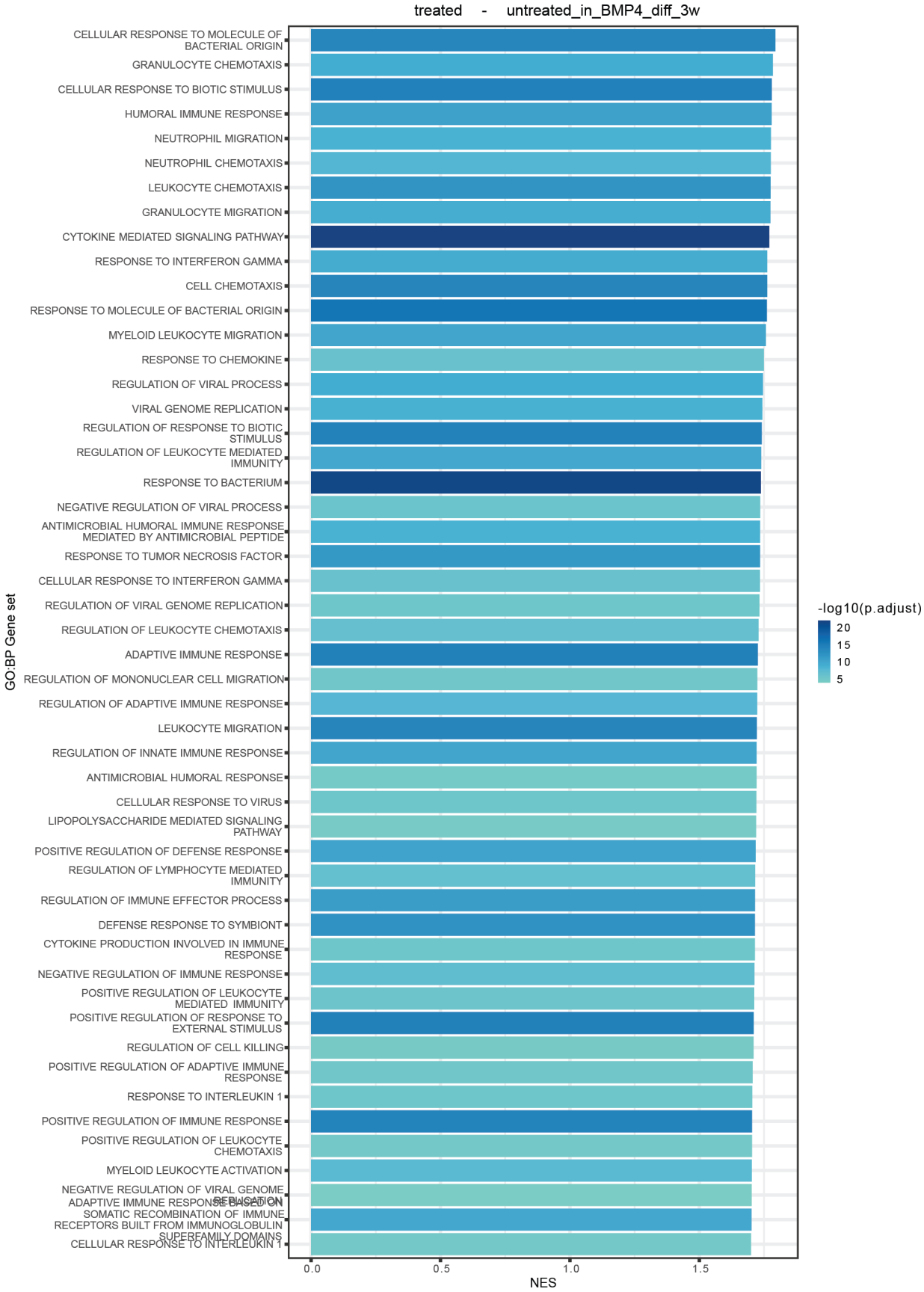

1005

1006 ***<u>Figure 17 (supplementary)</u>*** *– Bar plot showing the gene sets upregulated in treated BMP4*

1007 *astrocytes versus untreated BMP4 astrocytes. Gene sets were derived from the Biological*

1008 *Process (BP) ontology. Gene sets are ordered according to the absolute effect size (NES) and*
1009 *colored by significance (-log_{10} p-value adjusted).*

1010

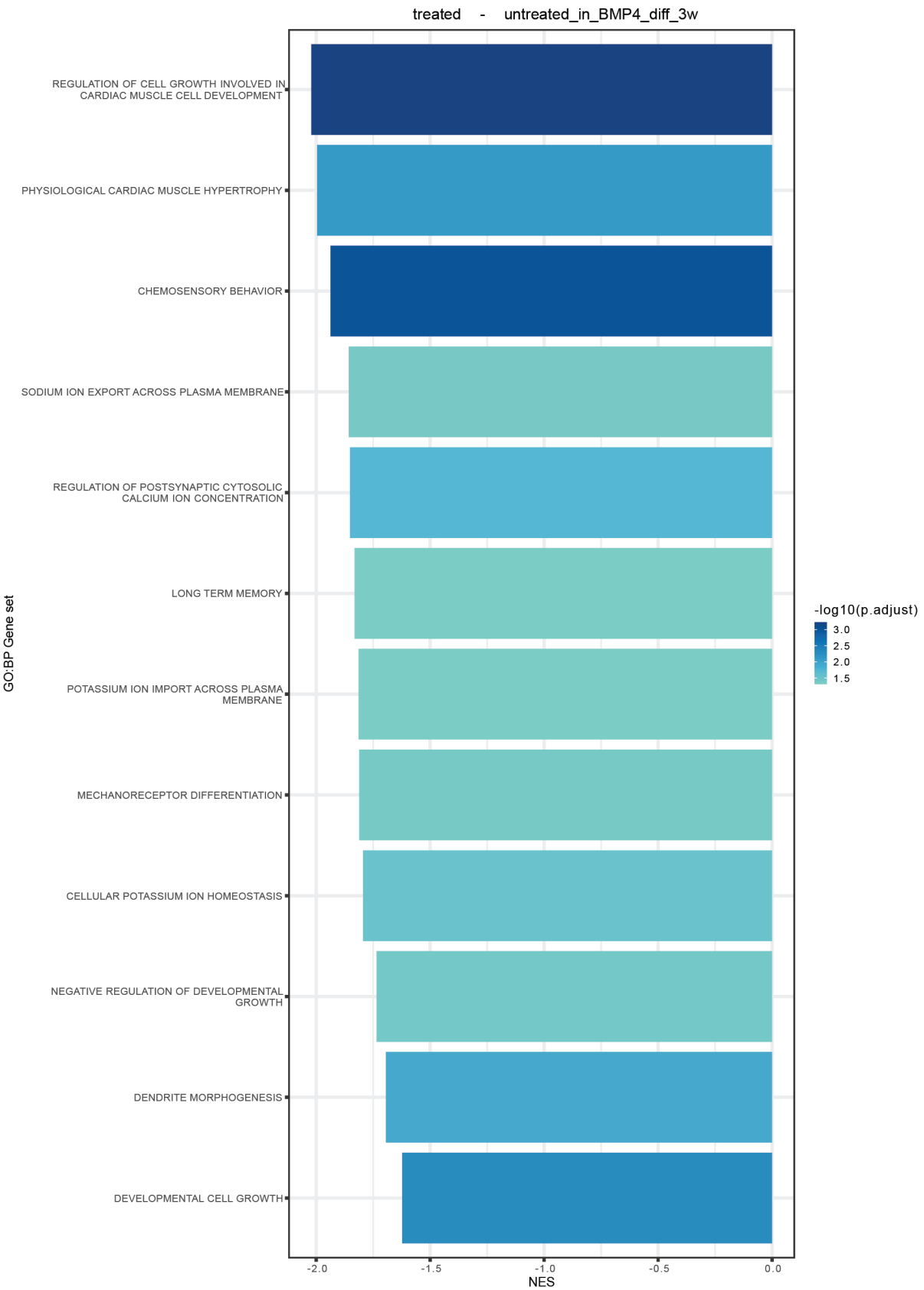

1011

1012 ***Figure 18 (supplementary)*** *– Bar plot showing the gene sets downregulated in treated BMP4*
1013 *astrocytes versus untreated BMP4 astrocytes. Gene sets were derived from the Biological*

1014 *Process (BP) ontology. Gene sets are ordered according to the absolute effect size (NES) and*
1015 *colored by significance (-log_{10} p-value adjusted).*

1016

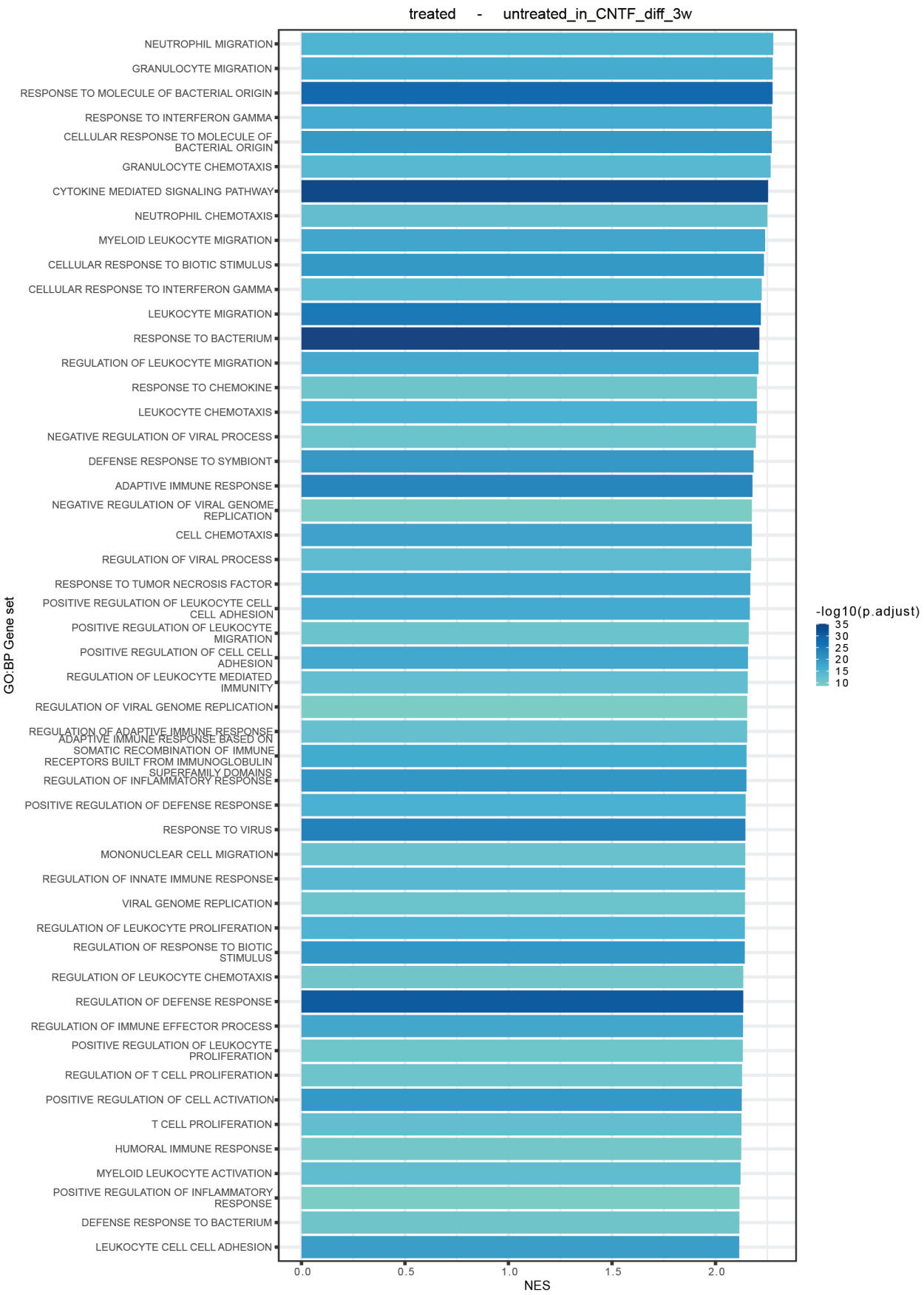
treated - untreated_in_CNTF_diff_3w
NEUTROPHIL MIGRATION
GRANULOCYTE MIGRATION
RESPONSE TO MOLECULE OF BACTERIAL ORIGIN
RESPONSE TO INTERFERON GAMMA
CELLULAR RESPONSE TO MOLECULE OF BACTERIAL ORIGIN
GRANULOCYTE CHEMOTAXIS
CYTOKINE MEDIATED SIGNALING PATHWAY
NEUTROPHIL CHEMOTAXIS
MYELOID LEUKOCYTE MIGRATION
CELLULAR RESPONSE TO BIOTIC STIMULUS
CELLULAR RESPONSE TO INTERFERON GAMMA
LEUKOCYTE MIGRATION
RESPONSE TO BACTERIUM
REGULATION OF LEUKOCYTE MIGRATION
RESPONSE TO CHEMOKINE
LEUKOCYTE CHEMOTAXIS
NEGATIVE REGULATION OF VIRAL PROCESS
DEFENSE RESPONSE TO SYMBIONT
ADAPTIVE IMMUNE RESPONSE
NEGATIVE REGULATION OF VIRAL GENOME REPLICATION
CELL CHEMOTAXIS
REGULATION OF VIRAL PROCESS
RESPONSE TO TUMOR NECROSIS FACTOR
POSITIVE REGULATION OF LEUKOCYTE CELL CELL ADHESION
POSITIVE REGULATION OF LEUKOCYTE MIGRATION
POSITIVE REGULATION OF CELL CELL ADHESION
REGULATION OF LEUKOCYTE MEDIATED IMMUNITY
REGULATION OF VIRAL GENOME REPLICATION
REGULATION OF ADAPTIVE IMMUNE RESPONSE
ADAPTIVE IMMUNE RESPONSE BASED ON SOMATIC RECOMBINATION OF IMMUNE RECEPTORS BUILT FROM IMMUNOGLOBULIN SUPERFAMILY DOMAINS
REGULATION OF INFLAMMATORY RESPONSE
POSITIVE REGULATION OF DEFENSE RESPONSE
RESPONSE TO VIRUS
MONONUCLEAR CELL MIGRATION
REGULATION OF INNATE IMMUNE RESPONSE
VIRAL GENOME REPLICATION
REGULATION OF LEUKOCYTE PROLIFERATION
REGULATION OF RESPONSE TO BIOTIC STIMULUS
REGULATION OF LEUKOCYTE CHEMOTAXIS
REGULATION OF DEFENSE RESPONSE
REGULATION OF IMMUNE EFFECTOR PROCESS
POSITIVE REGULATION OF LEUKOCYTE PROLIFERATION
REGULATION OF T CELL PROLIFERATION
POSITIVE REGULATION OF CELL ACTIVATION
T CELL PROLIFERATION
HUMORAL IMMUNE RESPONSE
MYELOID LEUKOCYTE ACTIVATION
POSITIVE REGULATION OF INFLAMMATORY RESPONSE
DEFENSE RESPONSE TO BACTERIUM
LEUKOCYTE CELL CELL ADHESION
GO:BP Gene set
0.0
0.5
1.0
1.5
2.0
NES
-log10(p.adjust)
35
30
25
20
15
10

1017

1018 **Figure 19 (supplementary)** – Bar plot showing the gene sets upregulated in treated CNTF
1019 astrocytes versus untreated CNTF astrocytes. Gene sets were derived from the Biological
1020 Process (BP) ontology. Gene sets are ordered according to the absolute effect size (NES) and
1021 colored by significance (-$\log_{10}$ p-value adjusted).

1022

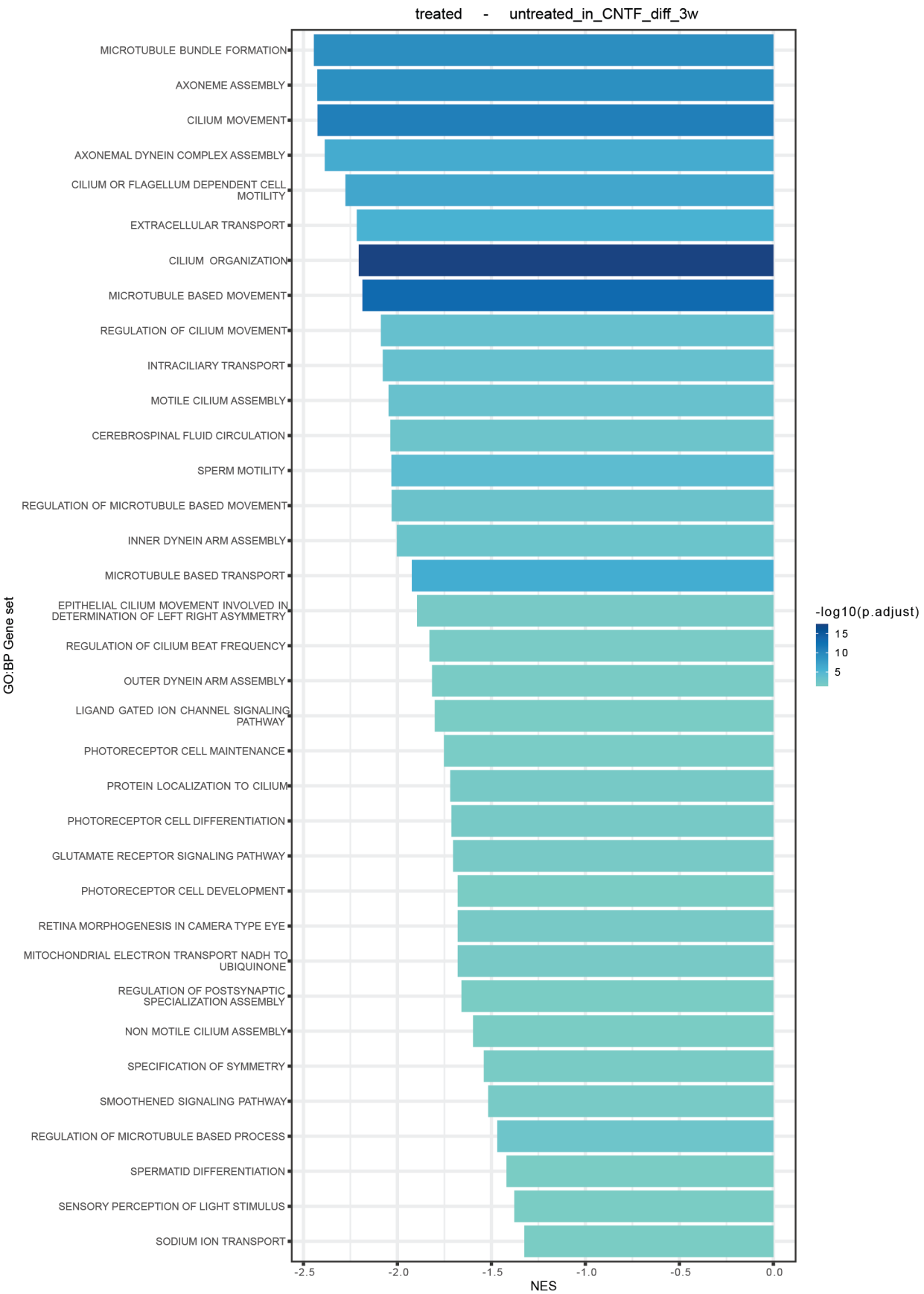
treated - untreated_in_CNTF_diff_3w
MICROTUBULE BUNDLE FORMATION
AXONEME ASSEMBLY
CILIUM MOVEMENT
AXONEMAL DYNEIN COMPLEX ASSEMBLY
CILIUM OR FLAGELLUM DEPENDENT CELL MOTILITY
EXTRACELLULAR TRANSPORT
CILIUM ORGANIZATION
MICROTUBULE BASED MOVEMENT
REGULATION OF CILIUM MOVEMENT
INTRACILIARY TRANSPORT
MOTILE CILIUM ASSEMBLY
CEREBROSPINAL FLUID CIRCULATION
SPERM MOTILITY
REGULATION OF MICROTUBULE BASED MOVEMENT
INNER DYNEIN ARM ASSEMBLY
MICROTUBULE BASED TRANSPORT
EPITHELIAL CILIUM MOVEMENT INVOLVED IN DETERMINATION OF LEFT RIGHT ASYMMETRY
REGULATION OF CILIUM BEAT FREQUENCY
OUTER DYNEIN ARM ASSEMBLY
LIGAND GATED ION CHANNEL SIGNALING PATHWAY
PHOTORECEPTOR CELL MAINTENANCE
PROTEIN LOCALIZATION TO CILIUM
PHOTORECEPTOR CELL DIFFERENTIATION
GLUTAMATE RECEPTOR SIGNALING PATHWAY
PHOTORECEPTOR CELL DEVELOPMENT
RETINA MORPHOGENESIS IN CAMERA TYPE EYE
MITOCHONDRIAL ELECTRON TRANSPORT NADH TO UBIQUINONE
REGULATION OF POSTSYNAPTIC SPECIALIZATION ASSEMBLY
NON MOTILE CILIUM ASSEMBLY
SPECIFICATION OF SYMMETRY
SMOOTHENED SIGNALING PATHWAY
REGULATION OF MICROTUBULE BASED PROCESS
SPERMATID DIFFERENTIATION
SENSORY PERCEPTION OF LIGHT STIMULUS
SODIUM ION TRANSPORT
GO:BP Gene set
-2.5
-2.0
-1.5
-1.0
-0.5
0.0
NES
-log10(p.adjust)
15
10
5

1023

1024 **Figure 20 (supplementary)** – Bar plot showing the gene sets downregulated in treated CNTF
1025 astrocytes versus untreated CNTF astrocytes. Gene sets were derived from the Biological
1026 Process (BP) ontology. Gene sets are ordered according to the absolute effect size (NES) and
1027 colored by significance ($-\log_{10}$ p-value adjusted).

1028

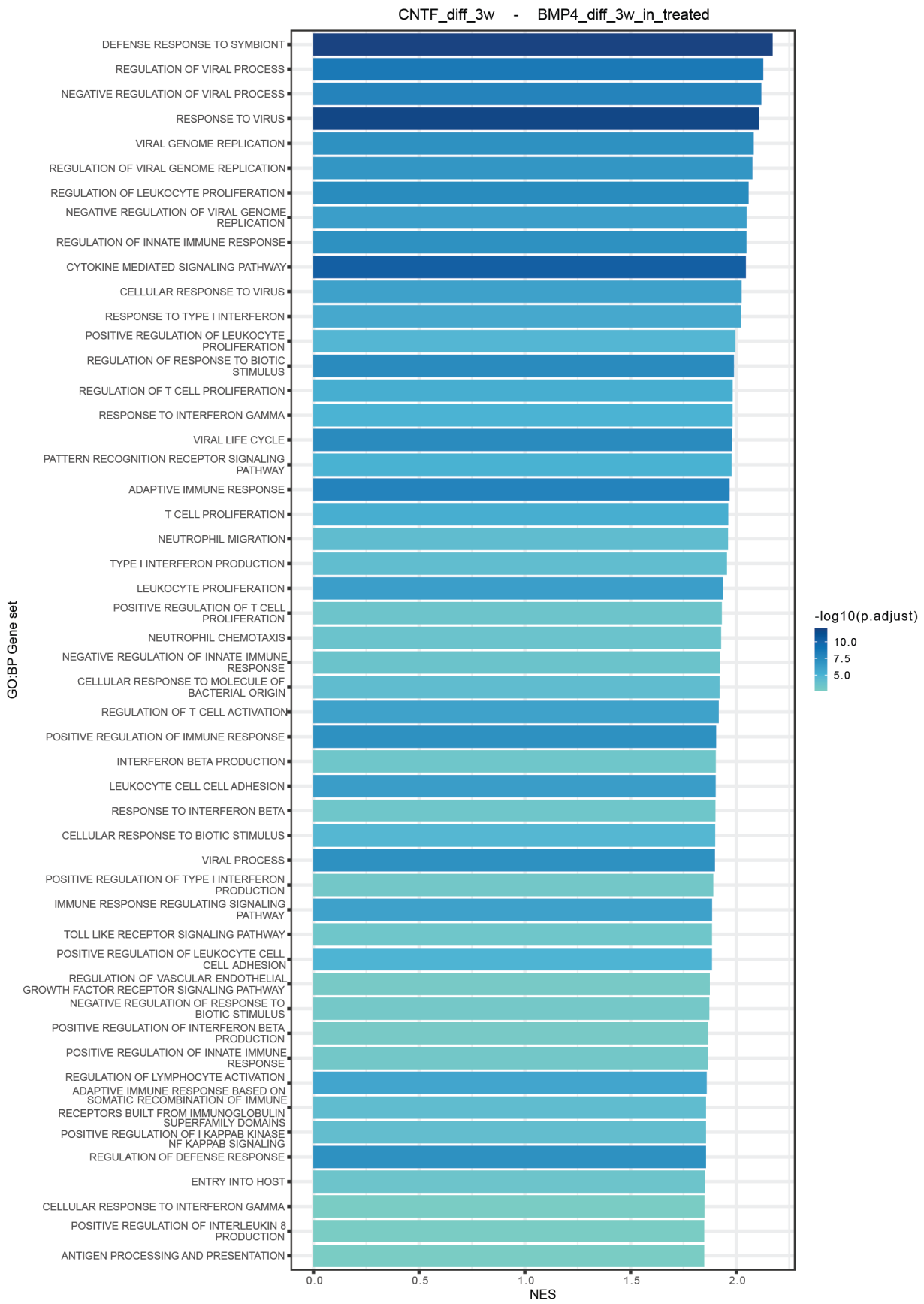

Figure 21 (supplementary) – Bar plot showing the gene sets upregulated in treated CNTF astrocytes versus treated BMP4 astrocytes. Gene sets were derived from the Biological

1032 Process (BP) ontology. Gene sets are ordered according to the absolute effect size (NES) and
1033 colored by significance (-$\log_{10}$ p-value adjusted).

1034

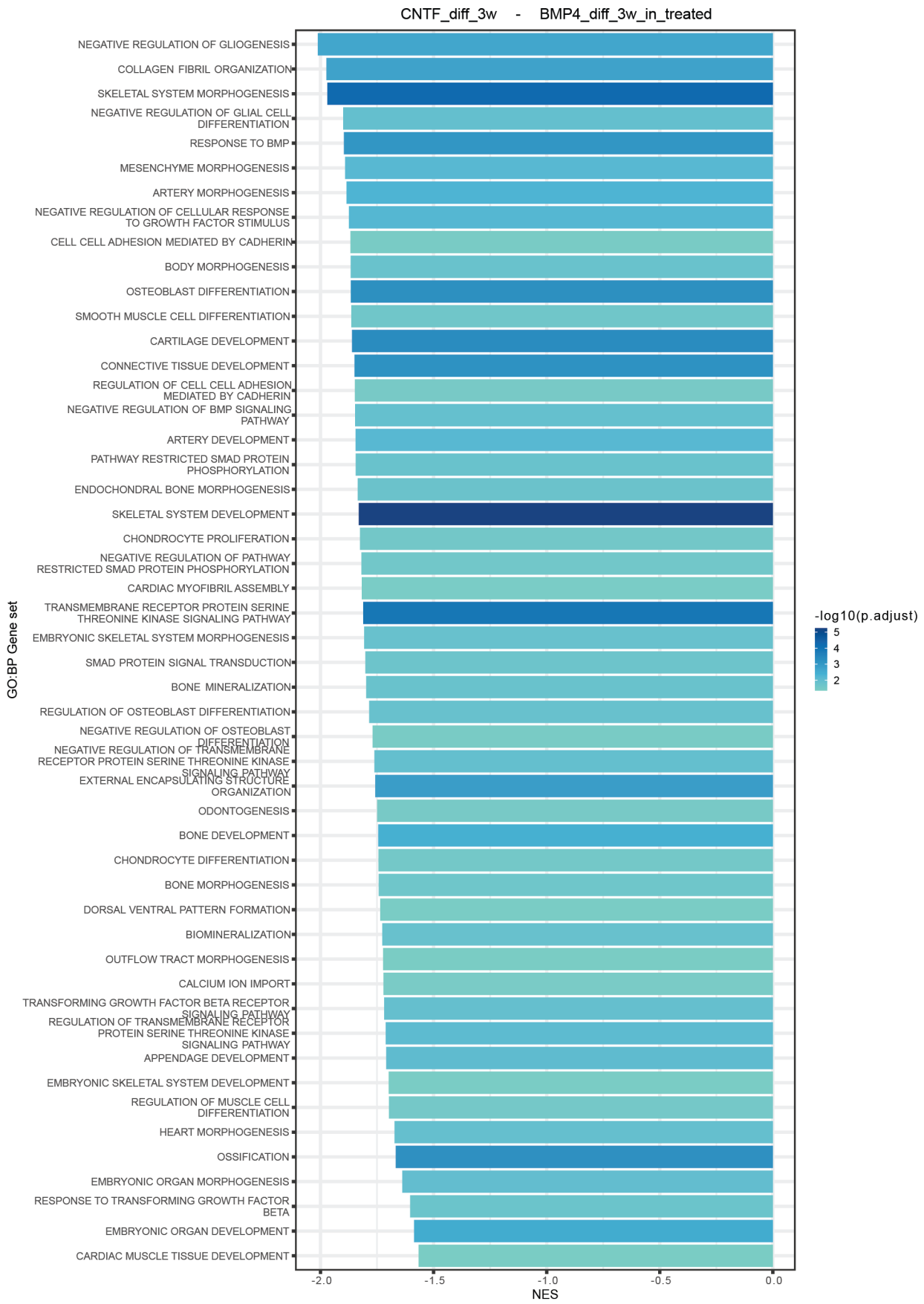
CNTF_diff_3w - BMP4_diff_3w_in_treated
NEGATIVE REGULATION OF GLIOGENESIS
COLLAGEN FIBRIL ORGANIZATION
SKELETAL SYSTEM MORPHOGENESIS
NEGATIVE REGULATION OF GLIAL CELL DIFFERENTIATION
RESPONSE TO BMP
MESENCHYME MORPHOGENESIS
ARTERY MORPHOGENESIS
NEGATIVE REGULATION OF CELLULAR RESPONSE TO GROWTH FACTOR STIMULUS
CELL CELL ADHESION MEDIATED BY CADHERIN
BODY MORPHOGENESIS
OSTEOBLAST DIFFERENTIATION
SMOOTH MUSCLE CELL DIFFERENTIATION
CARTILAGE DEVELOPMENT
CONNECTIVE TISSUE DEVELOPMENT
REGULATION OF CELL CELL ADHESION MEDIATED BY CADHERIN
NEGATIVE REGULATION OF BMP SIGNALING PATHWAY
ARTERY DEVELOPMENT
PATHWAY RESTRICTED SMAD PROTEIN PHOSPHORYLATION
ENDOCHONDRAL BONE MORPHOGENESIS
SKELETAL SYSTEM DEVELOPMENT
CHONDROCYTE PROLIFERATION
NEGATIVE REGULATION OF PATHWAY RESTRICTED SMAD PROTEIN PHOSPHORYLATION
CARDIAC MYOFIBRIL ASSEMBLY
TRANSMEMBRANE RECEPTOR PROTEIN SERINE THREONINE KINASE SIGNALING PATHWAY
EMBRYONIC SKELETAL SYSTEM MORPHOGENESIS
SMAD PROTEIN SIGNAL TRANSDUCTION
BONE MINERALIZATION
REGULATION OF OSTEOBLAST DIFFERENTIATION
NEGATIVE REGULATION OF OSTEOBLAST DIFFERENTIATION
NEGATIVE REGULATION OF TRANSMEMBRANE RECEPTOR PROTEIN SERINE THREONINE KINASE SIGNALING PATHWAY
EXTERNAL ENCAPSULATING STRUCTURE ORGANIZATION
ODONTOGENESIS
BONE DEVELOPMENT
CHONDROCYTE DIFFERENTIATION
BONE MORPHOGENESIS
DORSAL VENTRAL PATTERN FORMATION
BIOMINERALIZATION
OUTFLOW TRACT MORPHOGENESIS
CALCIUM ION IMPORT
TRANSFORMING GROWTH FACTOR BETA RECEPTOR SIGNALING PATHWAY
REGULATION OF TRANSMEMBRANE RECEPTOR PROTEIN SERINE THREONINE KINASE SIGNALING PATHWAY
APPENDAGE DEVELOPMENT
EMBRYONIC SKELETAL SYSTEM DEVELOPMENT
REGULATION OF MUSCLE CELL DIFFERENTIATION
HEART MORPHOGENESIS
OSSIFICATION
EMBRYONIC ORGAN MORPHOGENESIS
RESPONSE TO TRANSFORMING GROWTH FACTOR BETA
EMBRYONIC ORGAN DEVELOPMENT
CARDIAC MUSCLE TISSUE DEVELOPMENT
GO:BP Gene set
-2.0
-1.5
-1.0
-0.5
0.0
NES
-log10(p.adjust)
5
4
3
2

1035

1036 **Figure 22 (supplementary)** – Bar plot showing the gene sets downregulated in treated BMP4
1037 astrocytes versus untreated BMP4 astrocytes. Gene sets were derived from the Biological
1038 Process (BP) ontology. Gene sets are ordered according to the absolute effect size (NES) and
1039 colored by significance (-$\log_{10}$ p-value adjusted).

1040

1041

1042

1043 **Acknowledgements**

1044 A.S. wishes to acknowledge the UK-Dementia Research Institute and the Medical Research
1045 Council, which supported a part of this study with a programme grant funding.S.J.M. is
1046 supported by the UK Dementia Research Institute (award number UKDRI-6009) through UK
1047 DRI Ltd, principally funded by the UK Medical Research Council and a Medical Research
1048 Council grant (award number MR/W004984/1).

1049 **Ethics declaration**

1050 The authors declare no competing interests.

1051

1052 **Materials and Methods**

1053 **Cell culture**

1054 All cells were kept in humidified atmosphere at 37°C with 5% CO_2. Human iPSCs were
1055 cultured on plates coated with Matrigel (Corning; 1:100), fed with Essential 8 Flex medium
1056 (Gibco) and passaged with ethylenediaminetetraacetic acid with phosphate-buffered saline
1057 (EDTA-PBS) (Gibco, 0.5 mM).

1058 Motor neuron progenitors were generated and patterned to ventral spinal cord identity
1059 following a previously published protocol[20].

1060 Cortical neuron progenitors were generated according to a previously published protocol[75].

1061 Both these progenitors were cultured in a base medium containing 50% advanced
1062 Dulbecco's modified eagle's medium (DMEM) (Gibco) and 50% NeuroBasal (Gibco) with
1063 B27 (Gibco) and N2 (Gibco) supplements, Penicillin-Streptomycin antibiotic mix (Gibco, 100
1064 µg/ml) and GlutaMAX (Gibco, 1X). Base medium was supplemented with FGF-2 (Gibco, 20
1065 ng/ml) (F20 medium).

1066 Astrocyte progenitors were obtained following a published protocol[19]. Briefly, neurospheres
1067 were formed starting from overconfluent motor neuron progenitors and cultured on an orbital
1068 shaker (60 rpm) in F20 medium for 2 weeks. They were then mechanically chopped at the
1069 start of the glial enrichment phase and cultured for 2-4 weeks in base medium supplemented
1070 with EGF (Gibco, 20 ng/ml) and leukaemia inhibiting factor (LIF) (Sigma-Aldrich, 20 ng/ml).
1071 After the enrichment, spheres were propagated in base medium containing EGF (20 ng/ml)
1072 and FGF-2 (20 ng/ml) (EF20 medium). After 1-2 weeks the spheres were landed in Matrigel-
1073 coated plates (1:100) to allow a population of monolayer astrocytes to migrate out of them.

1074 Single cell suspensions of astrocyte progenitor cells were isolated and then propagated in
1075 EF20 medium and passaged with Accutase (StemPro) when they reached confluency.

1076 For neuronal differentiation of motor neuron progenitors and cortical neuron progenitors,
1077 base medium supplemented with compound E (Enzo, 0.1 μM) was used.

1078 For differentiation of astrocyte progenitors into astrocytes, NeuroBasal medium was used.
1079 This was supplemented with B27 (Gibco), Non-Essential Amino Acids (Gibco, 1X), Penicillin-
1080 Streptomycin antibiotic mix (Gibco, 100 μg/ml), GlutaMAX (Gibco, 1X) and either BMP4
1081 (Gibco, 10 ng/ml) or CNTF (Gibco, 20 ng/ml) or a combination of both (respectively,
1082 NB27+BMP4, NB27+CNTF, NB27+BOTH). Throughout the differentiation process (the
1083 duration is specified for each experiment) cultures were fed every other day.

Cell line name	Donor Age	Donor Sex
Control 2	64	Male
Control 3	Unknown	Female

1084 **Table 1** – iPSC lines

1085

1086 Constructs

1087 The mito-dendra2 construct was derived from the Addgene plasmid #55796
1088 (http://n2t.net/addgene:55796; RRID: Addgene_55796), contributed from David Chan.
1089 Cloning was performed using the GeneArt assembly kit (Invitrogen) to insert the mito-
1090 dendra2 sequence into a PiggyBac (PB) backbone construct with a T2A Neomycin selection
1091 cassette. Other PiggyBac constructs were cloned in the laboratory, such as PB-EF1α-GFP-
1092 PGK-Puro and PB-CAG-RFP-Hygro for stable transfection of GFP and RFP. When stable
1093 transfections were required, these vectors were co-transfected with a construct encoding the
1094 PB transposase.

1095 Chemical transfection of astrocyte progenitors

1096 Stable lines of astrocyte progenitors expressing PB-Ef1α-GFP-PGK-Puro were established
1097 to perform single cell shape analysis aiming for 5-10% transfection efficiency. Stable co-
1098 transfection of PB-CAG-RFP-Hygro and PB-Ef1α-mito-dendra2-Neo was carried out to allow
1099 visualisation of mitochondrial distribution in single cells. All transfections were performed via
1100 lipofection using TransIt-LT1 transfection reagent (Mirus). Astrocyte progenitors were
1101 passaged into 24 well plates one day before the transfection. A total of 1μg of DNA per well
1102 of a 24 well plate was used in 200 μL of pen-strep free EF20 medium.

1103 This solution was well mixed and added to the wells which also contained 200 µL of
1104 penicillin-streptomycin (Pen-Strep) free medium. The medium containing the transfection
1105 reagent was exchanged with growth medium after 24 h. Cells were cultured to confluency
1106 and then pooled into a 6-well plate and there further expanded.

1107

1108 **Treatment with reactivity factors**

1109 To induce reactivity, 2-weeks differentiated astrocytes were cultured for one additional week
1110 in the same medium supplemented with reactivity factors TNF (Cell Signalling Technology,
1111 30 ng/ml), IL-1α (Sigma, 1 µg/ml) and C1q (Abcam, 400 µg/ml) (TIC).

1112 After treatment cells were either fixed, stained and processed for morphological analysis and
1113 protein quantification or scratched and live images (following the methods documented in
1114 relevant sections).

1115

1116 **Treatment with cytoskeleton disrupting drugs**

1117 For the disruption of actin cytoskeleton, 2 weeks differentiated BMP4 and CNTF astrocytes
1118 were treated with ROCK inhibitor Y27632 (Tocris, 25 µM) or LAT B (Sigma, 1 µM) for 2
1119 hours. A vehicle control for LAT B was carried out using 0.1% (v/v) dimethyl sulfoxide
1120 (DMSO, Sigma). For the disruption of microtubules, 2 weeks differentiated BMP4 and CNTF
1121 astrocytes were treated with a range of concentrations (1 nM, 10 nM, 50 nM, 100 nM) of
1122 Vincristine (ThermoFisher) for 24 hours. After treatment, cells were fixed and imaged at 20x
1123 magnification on a Nikon Tie Eclipse microscope.

1124 For all experiments, an untreated control was carried out.

1125 Immunostaining and live dyes

1126 For immunostaining, cells were fixed using 4% paraformaldehyde (PFA) for a duration of 15
1127 minutes. This was followed by 3 washes with PBS. Cell permeabilization was achieved
1128 through 10 minutes incubation with 0.1% Triton-X (Sigma) in PBS. This was then replaced
1129 with the blocking solution, consisting of 3% goat serum (GS, Sigma) in PBS, which was
1130 incubated for 30 minutes. Primary antibodies were diluted in a solution of 0.05% Triton 1.5%
1131 GS in PBS and incubated for 1 hour at room temperature, followed by 3 x PBS washes.
1132 Details of primary antibodies and their concentrations can be found in Table 2. Secondary
1133 antibodies were diluted in the same solution as the primary and incubated for 30 minutes,
1134 followed by 3 x PBS washes. All secondary antibodies were employed at a final

1135 concentration of 2 µg/ml. Details of the secondary antibodies used can be found in table 3.
1136 DAPI (Sigma) was used in combination with the secondary antibodies at a final
1137 concentration of 1 µg/ml.

1138 For Connexin-43, EAAT1, EAAT2 staining and synaptogenesis analysis, cells were fixed with
1139 100% methanol for 10 minutes at -20°C to maintain membrane integrity. This was followed
1140 by 3 x PBS washes. In addition, the Triton-X permeabilization step was omitted. Triton-X
1141 was replaced by PBS as a diluent in the antibody staining solutions.

1142 All samples were mounted with FluorSave (Millipore) for a minimum of 1 hour at room
1143 temperature before imaging.

1144 Silicon rhodamine-tubulin (Spirochrome) was used at a concentration of 100 nM and
1145 incubated with the cells for 1 hour in the incubator, followed by 3 x PBS washes to remove
1146 dye residues.

1147 Fluo-4AM (ThermoFisher) was used at a concentration of 5 µM and incubated with cells for
1148 1 hour, followed by 2 x PBS washes.

1149 Cell permeable Hoescht 33342 (Sigma) was used at a concentration of 1 µg/ml and
1150 incubated for 15 minutes in live cells, followed by 3 x PBS washes.

1151

Antibody	Host species	Isotype	Manufacturer	Catalogue code	Dilution
GFAP-Cy3	Mouse	IgG1	Sigma	C9205	1:500
GFAP	Chicken	Polyclonal	Abcam	Ab4674	1:1250
S100β	Mouse	IgG1	Sigma	S2532	1:1000
Ki67	Rabbit	IgG1	Abcam	Ab92742	1:500
Cx43	Mouse	IgG1	ThermoFisher	13-8300	1:500
GFP	Rabbit	Polyclonal	Abcam	Ab6556	1:500
β3-tubulin	Mouse	IgG2b	Sigma	T5076	1:1000
MAP2	Mouse	IgG1	Sigma	13-1500	1:750
Synaptophysin	Rabbit	Polyclonal	ThermoFisher	PA1-1043	1:500
α-tubulin	Mouse	IgG2a	ThermoFisher	MA5-31466	1:500
C3d	Rabbit	Polyclonal	Dako	A0063	1:500
PSD95	Mouse	IgG2a	ThermoFisher	MA1-045	1:500
EAAT1	Rabbit	Polyclonal	Novus Biologicals	NBP1-84940	1:500
EAAT2	Rabbit	Polyclonal	Abcam	Ab41621	1:500

1152 **Table 2** – Primary antibodies

1153

1154

1155

1156

1157

Target Species	Host species	Isotype	Conjugate	Manufacturer	Catalogue code	Dilution
Mouse	Goat	IgG1	Alexa fluor 555	Invitrogen	A21127	1:1000
Mouse	Goat	IgG1	Alexa fluor 647	Invitrogen	A21240	1:1000
Mouse	Goat	H+L	Alexa fluor 488	Invitrogen	A32723	1:1000
Mouse	Goat	IgG2bn	Alexa fluor 647	Invitrogen	A21242	1:1000
Mouse	Goat	IgG2a	Alexa fluor 555	Invitrogen	A21137	1:1000
Rabbit	Goat	H+L	Alexa fluor 555	Invitrogen	A32732	1:1000
Rabbit	Goat	H+L	Alexa fluor 488	Invitrogen	A11034	1:1000
Rabbit	Goat	H+L	Alexa fluor 647	Invitrogen	A32733	1:1000
Chicken	Goat	H+L	Alexa fluor 488	Invitrogen	A11039	1:1000

1158 **Table 3** – Secondary antibodies

1159

1160 <u>Astrocyte morphological analysis over differentiation</u>

1161 Astrocyte progenitors sparsely transfected with GFP were differentiated for 3 weeks in either
1162 NB27+BMP4, NB27+CNTF, NB27+BOTH or NB27 alone. Live imaging was performed on
1163 the Nikon Ti2 Eclipse microscope on days 0, 1, 7, 14 and 21 during the differentiation
1164 process. For each imaging timepoint imaging medium was used. 8x8 grids with 10% overlap

1165 were acquired in each well at each timepoint, using a 40x extra-long working distance
1166 objective. An imaging control was performed in parallel.

1167 Manual process and cell body analysis

1168 To assess subtle differences in shape between GFP^+ astrocytes cultured in CNTF or NB27
1169 alone, they were fixed with PFA, stained and imaged on the SoRa microscope at 60x
1170 magnification. Z-stacks of 35 slices with a step size of 0.3 µm were taken and images tiled to
1171 capture whole GFP^+ cells.

1172 Manual analysis of process length and cell body shape in GFP^+ astrocytes was performed by
1173 a blinded operator using ImageJ after stitching the tiles. The segmented line tool was used
1174 to trace the primary processes starting from the cell body and ending at the process tip.
1175 Process number and length were recorded and averaged per cell. The cell soma was traced
1176 using the freehand selection tool, excluding the cell processes.

1177 Cytokine switching experiments

1178 Astrocytes were differentiated with BMP4 or CNTF for either 1 or 2 weeks; at the time of
1179 switching, a number of wells were changed to the alternate cytokine (i.e. BMP4 to CNTF and
1180 CNTF to BMP4) while a number of control wells were maintained in the same differentiation
1181 media. At the end of the differentiation, 2 or 3 weeks of differentiation respectively, cells were
1182 fixed with PFA and imaged on the Nikon Ti2 Eclipse microscope at 20x magnification, taking
1183 a 5x5 grid with 10% overlap in each well.

1184

1185 Glutamate uptake assay

1186 To analyze glutamate uptake kinetics, a fluorometric glutamate uptake assay kit (Abcam)
1187 was used. 2-weeks differentiated BMP4 and CNTF astrocytes were incubated with 100 µM
1188 L-glut in Hanks' Balanced Salt Solution (HBSS, Gibco) for different intervals of times (0, 60,
1189 180 minutes). EAAT inhibitor PDC was used as a control and was incubated with the cells
1190 for 180 minutes (180 + PDC). Media was collected and enzyme mixes prepared according to
1191 the manufacturer's instructions, before transferring to a clear bottom 96-well plate and
1192 incubating for 1 hour at RT. Glutamate-concentration standards were prepared in dilution
1193 buffer and used as a reference for quantification. A Tecan spark microplate reader was used
1194 to quantify fluorescence which correlated to L-glut concentration in the media. A blank well
1195 containing only enzyme mix was used as a control to subtract background fluorescence from
1196 all experimental wells. All experimental wells were then interpolated to the standard curve.

1197 During the enzyme incubation period, the astrocytes were incubated with Hoechst 33342
1198 and then PFA fixed; nuclei images were taken on a Nikon Ti2 widefield microscope and the
1199 number of nuclei used to calculate average number of cells per well.

1200 Fluorescence intensity was normalised to the number of cells to standardise differences in
1201 confluency. All wells were also normalised to the average of the 0-minute timepoint of the
1202 corresponding experiment to produce a % to the t0 baseline.

1203 Calcium imaging

1204 To analyse calcium wave dynamics, 3 weeks differentiated BMP4 and CNTF astrocytes
1205 stained with Fluo-4AM were live imaged in a custom-built widefield microscope. A 5 mM ATP
1206 (Sigma) solution was prepared in Ca^{2+} free HBSS.

1207 Timelapses were taken with 20x magnification, acquiring 400 images with a 400 ms interval.
1208 ATP was added at a final concentration of 0.5 mM at frame 110-115. An imaging control and
1209 a vehicle control were also performed.

1210 To quantify calcium kinetics, pre-processing of the time-lapse videos was performed,
1211 including bleach correction with exponential fit and image registration to account for plate
1212 movements during the imaging, both on ImageJ. Approximately 30 circular, 5-pixel radius
1213 ROIs were drawn in each well, centering on the cell bodies. Fluo-4AM intensity in these
1214 ROIs was measured across every frame and the data input into PeakCaller software to
1215 perform peak analysis. To visualize intensity changes, a temporal color code with Fire LUT
1216 was applied to the timelapses on ImageJ.

1217 **Scratch assay**

1218 To test wound healing capacity, astrocytes were differentiated with BMP4 or CNTF for 2
1219 weeks, followed by either another week of standard differentiation or, in a subset of wells,
1220 one week of treatment with TICs. Cells were stained with silicon rhodamine-tubulin (SiR-
1221 Tubulin) and, in a subset of wells for each condition, a scratch was made with a pipette tip in
1222 the center of the well.

1223 Following two PBS washes, cells were put in imaging medium and then imaged live on a
1224 custom built widefield microscope at 4x magnification. Imaging was then performed again, in
1225 the same positions, at 24 hours, 48 hours and 1 week after the scratch. Before each imaging
1226 session, cells were re-stained with SiR-Tubulin. At the end of the week, they were fixed with
1227 4% PFA and stained using immunocytochemistry

1228 The ImageJ Wound Healing plugin was used to quantify scratch areas at each time point
1229 and in each condition from the live images. The percentage of scratch area filled over the
1230 original total area was calculated, and every condition was normalized to untreated BMP4.

1231 To assess nuclei presence in the scratch area, nuclei were identified from DAPI images
1232 using a pipeline including pixel classification using ilastik and object recognition using
1233 CellProfiler. At the same time, ilastik was used to produce a segmentation of the SiR-Tubulin
1234 image from the Day 0 timepoint. This was used to mask the nuclei and identify for each
1235 condition the nuclei that, at the one-week timepoint, had migrated or proliferated to the point
1236 of occupying the original scratch area.

1237 Mitochondrial dynamics analysis

1238 For the analysis of mitochondrial distribution and motility, astrocytes progenitors were co-
1239 transfected with mito-dendra2 and RFP, seeded on glass bottom chambers (Ibidi) and
1240 differentiated for 2-weeks with either BMP4 or CNTF. After PFA fixation, they were stained
1241 with DAPI.

1242 For mitochondrial distribution, images were acquired on a CSU-W1 SoRa microscope with
1243 60x magnification. Z-stacks composed of 35 slices with 0.3 µm step size (for a total of 10.5
1244 µm) were taken and tiling was performed on ImageJ to capture whole cell morphology.

1245 For the analysis of mitochondrial distribution, pixel classification was carried out with ilastik
1246 on the DAPI and RFP channels to generate binary segmentations of the nuclei and whole
1247 cells. These were uploaded onto CellProfiler together with the mito-dendra2 images. Nuclei
1248 with less than 95% overlap with the RFP cell objects were excluded, as well as RFP whole
1249 cells containing more than one nucleus (due to overlapping of non-fluorescent cells), to
1250 obtain one nucleus per RFP cell. The distribution of mito-dendra2 intensity was measured
1251 dividing the cell objects in 40 radial 25 µm bins (for a total of 1000 µm) starting from the
1252 edge of the nucleus. The fraction of total mito-dendra2 intensity in each bin was converted to
1253 a percentage and plotted.

1254 For mitochondrial motility, 2-weeks differentiated BMP4 and CNTF astrocytes were changed
1255 to imaging medium and imaging performed on the CSU-W1 SoRa with 40x magnification.
1256 For each cell, an initial image was taken of both RFP and mito-dendra2, followed by a
1257 timelapse of only mito-dendra2 signal. For this, an image was taken every 10 seconds for 2
1258 minutes with Z-stacks of 6 slices with a 2 µm step size (for a total of 12 µm). Low laser
1259 power was used to reduce toxicity. After the timelapse, another picture was taken with the
1260 RFP, mito-dendra2 and Hoechst channels to be used to locate the nucleus (without Z-stack).

1261 For CNTF cells, an additional video was acquired at the end of processes (at a minimum
1262 distance of 150 µm from the nucleus).

1263 The analysis of mitochondrial motility was carried out on the mito-dendra2 timelapse videos;
1264 25x25 µm ROIs were established in the perinuclear (within 25 µm from the nucleus) and
1265 non-perinuclear (50-100 µm from the nucleus) areas, as well as at the process end for CNTF
1266 differentiated astrocytes (within 50 µm from the tip of an RFP^+ process and at least 150 µm
1267 away from the nucleus). These ROIs were then bleach corrected, thresholded, contrast
1268 enhanced and binarized employing ImageJ. The ImageJ Total Motility plugin was used to
1269 quantify the percentage of pixels changing their intensity (0 to 1 or 1 to 0) between each
1270 frame. These percentages were averaged per compartment for each cell and plotted. In
1271 addition, temporal colour coding (Spectrum LUT) was used to visualise moving and
1272 stationary mitochondria on the timelapse.

1273 Neuronal co-culture and synaptogenesis analysis

1274 BMP4 and CNTF astrocytes were differentiated in their usual media for 2 weeks before
1275 plating cortical neuron progenitors on top of them and switching the culture to 50/50 medium
1276 with compound E for 2 additional weeks. At the end, they were fixed with methanol and
1277 stained for MAP2, PSD95 and synaptophysin.

1278 Imaging was performed on the SoRa microscope at 60x magnification, acquiring 10.5 µm Z-
1279 stacks with 0.3 µm step size.

1280 To quantify synaptic proteins and their co-localization, 150x150 µm ROIs were made.
1281 Computer software ilastik was used to produce binary segmentations for each of the three
1282 channels. For PSD95 and synaptophysin the training for pixel classification was carried out
1283 on the Z-stacks, followed by the creation of maximum intensity projections (MIP); for MAP2,
1284 training was performed directly on 2D MIPs as this enables more accurate dendrite
1285 segmentation. A CellProfiler pipeline was used to count the number of $PSD95^+$,
1286 $Synaptophysin^+$ and co-localised $PSD95^+$/$Synaptophysin^+$ puncta located within the MAP2
1287 signal. The data is represented as number of puncta per 100 μm^2 MAP2.

1288 Imaging

1289 Images for the scratch assay, calcium signaling and cell cycle assay were taken on a
1290 custom-built widefield microscope, at 4x magnification and 20x magnification, respectively.

1291 Images for the live astrocyte shape characterisation during differentiation, cytokine switching
1292 experiments, cytoskeletal assays and reactive morphological analysis were taken on a Nikon

1293 Yi2 Eclipse widefield microscope, all at 20x magnification except for the live characterisation
1294 for which a 40x ELWD objective was used.

1295 Images for the following experiments were acquired using the Olympus SpinSR10 SoRa
1296 spinning disk confocal microscope: manual analysis of processes, connexin-43 expression
1297 analysis, EAAT1 expression analysis, neuronal co-culture experiments, mitochondrial
1298 distribution and motility assays. Magnification ranging from 20x to 60x was used.

1299

1300 **Astrocyte morphological analysis**

1301 For all experiments which required single-cell morphology analysis of astrocytes transfected
1302 with GFP, a semi-automated image analysis pipeline was established which relies on open-
1303 source software.

1304 GFP images were first pre-processed using a custom ImageJ macro which carried out
1305 contrast enhancement and gaussian blur to improve boundary detection, in addition to
1306 stitching tiles when required.

1307 ilastik was then used to perform pixel classification. A subset of randomly selected images
1308 (around 10%) was used to train the algorithm in an operator-dependent manner by assigning
1309 two labels, corresponding to foreground pixels (GFP^+ cells) and background pixels (GFP^-).
1310 After sufficient training, the software was able to perform accurate unsupervised pixel
1311 classification, and all images were batch processed in an automated manner. The results
1312 were binary segmentations of GFP^+ cells which were batch thresholded on ImageJ and, if
1313 necessary, split into smaller tiles to allow faster downstream analysis. These were then input
1314 into CellProfiler where the GFP^+ cells were identified as objects (after size-based filtering to
1315 exclude debris). Any objects touching the image border were excluded to limit the analysis to
1316 entire cells. Morphometric parameters were obtained for all cell objects and exported for
1317 further analysis.

1318 Protein expression analysis

1319 In all cases where protein expression was quantified from immunostaining images, the
1320 images from the channel corresponding to the protein of interest were pre-processed to
1321 subtract background and, in the case of Z-stacks, made into maximum intensity projections
1322 using ImageJ.

1323 These pre-processed images were input into CellProfiler together with the DAPI channel
1324 images. Nuclei were identified as objects thanks to both size- and intensity-based
1325 thresholding and their number counted for each field of view. The whole image intensity of

1326 the staining of interest was measured and the data exported to excel. For each image, the
1327 lower quartile intensity was subtracted from the total intensity, and the result was then
1328 divided by the number of identified nuclei, providing a normalized intensity value per image
1329 (arbitrary units, a.u). The fields of view average for each well were plotted.

1330 **Library prep and bulk RNA sequencing**

1331 The sequencing library was prepared with NEBNext UltraTM II Directional PolyA mRNA kit
1332 (NEB) and sequencing was performed on Illumina HiSeq 4000 yielding around 33 million
1333 strand specific 75 bp paired-ends reads per sample. Information on the number of reads and
1334 other statistics can be found in Table 4 and Table 5.

1335 **Bioinformatic analysis of bulk RNA-seq**

1336 Bulk RNA-seq data processing

1337 Primary data analysis was done using the nf-core/rnaseq pipeline [https://github.com/nf-
1338 core/rnaseq] using default parameters (version 3.10.1) written in the Nextflow domain
1339 specific language (version 22.10.3) in conjunction with Singularity (version 3.6.4). Alignment
1340 of sequencing reads was carried out using the reference human genome (Ensembl GRCh38
1341 release 95). Gene counts per gene per sample were obtained using RSEM-STAR (RSEM
1342 v1.3.1, STAR v2.7.10a)[76] option of the pipeline and they were imported on DESeq[77]
1343 (v1.38.3) within R environment (v4.2.2) for differential expression analysis. For further quality
1344 control (QC), PCA and heatmap plots (data not shown) with hierarchical clustering of top 500
1345 variable genes post variable stabilizing transformation were studied for any batch effects.

Sample	Tot Sequences	Reads Mapped	%reads_mapped
CTRL2_BMP4_2_weeks_untreated_1	63318020	62742108	99.09044534241596
CTRL2_BMP4_2_weeks_untreated_2	60343938	59872215	99.21827607604926
CTRL2_BMP4_2_weeks_untreated_3	68280126	67632955	99.05218247546877
CTRL2_BMP4_3_weeks_treated_1	72523052	71896908	99.13662762013932
CTRL2_BMP4_3_weeks_treated_2	68719910	68097505	99.09428723058572
CTRL2_BMP4_3_weeks_treated_3	68118536	67530234	99.13635548479786
CTRL2_BMP4_3_weeks_untreated_1	66628114	66104610	99.21428963155104
CTRL2_BMP4_3_weeks_untreated_2	62246314	61673077	99.07908281926541
CTRL2_BMP4_3_weeks_untreated_3	75548322	74816579	99.03142388787933
CTRL2_CNTF_2_weeks_untreated_1	67261926	66585345	98.99410998132882
CTRL2_CNTF_2_weeks_untreated_2	71659442	71061694	99.16584893306873
CTRL2_CNTF_2_weeks_untreated_3	71068294	70510948	99.21575998433282
CTRL2_CNTF_3_weeks_treated_1	68734158	68098991	99.07590778954476
CTRL2_CNTF_3_weeks_treated_2	59399876	58853905	99.08085498360299
CTRL2_CNTF_3_weeks_treated_3	71788402	71182205	99.15557808349043
CTRL2_CNTF_3_weeks_untreated_1	58906132	58378701	99,10462463
CTRL2_CNTF_3_weeks_untreated_2	68983766	68423294	99.18753058509448
CTRL2_CNTF_3_weeks_untreated_3	53404294	52966947	99.18106397961182
CTRL2_progenitor_0_weeks_untreated_1	67729414	67172903	99.17833188398765
CTRL2_progenitor_0_weeks_untreated_2	55756870	55285879	99.15527718826398
CTRL2_progenitor_0_weeks_untreated_3	66857320	66328786	99.20945978690142
CTRL3_BMP4_2_weeks_untreated_1	60670484	60124120	99.09945666495754
CTRL3_BMP4_2_weeks_untreated_2	60575578	60062557	99,15308939
CTRL3_BMP4_2_weeks_untreated_3	72381544	71709248	99.07117759190105
CTRL3_BMP4_3_weeks_treated_1	59569862	58937206	98.93795960111508
CTRL3_BMP4_3_weeks_treated_2	60456496	59835814	98.97334109472703
CTRL3_BMP4_3_weeks_treated_3	63511056	62774236	98.83985553633372
CTRL3_BMP4_3_weeks_untreated_1	63483212	62906589	99.09169214689389
CTRL3_BMP4_3_weeks_untreated_2	63907994	63137193	98.79388954064183
CTRL3_BMP4_3_weeks_untreated_3	70417194	69720828	99.01108527556495
CTRL3_CNTF_2_weeks_untreated_1	67219916	66494396	98.92067702078057
CTRL3_CNTF_2_weeks_untreated_2	57342148	56836702	99.11854365832266
CTRL3_CNTF_2_weeks_untreated_3	68479538	67892401	99.14260957776906
CTRL3_CNTF_3_weeks_treated_1	83891758	82793982	98.69143760224932
CTRL3_CNTF_3_weeks_treated_2	62189738	61368150	98.67890101096744
CTRL3_CNTF_3_weeks_treated_3	70108650	69162549	98.65052172592112
CTRL3_CNTF_3_weeks_untreated_1	61146520	60582830	99.07813232870815
CTRL3_CNTF_3_weeks_untreated_2	61434970	60895515	99.12190890627927
CTRL3_CNTF_3_weeks_untreated_3	66441722	65868380	99.13707534551858
CTRL3_progenitor_0_weeks_untreated_1	71789704	71124727	99.07371536174603
CTRL3_progenitor_0_weeks_untreated_2	77861818	77130398	99.06061787563193
CTRL3_progenitor_0_weeks_untreated_3	58143092	57661737	99.17212005168216

Table 4 - RNA sequencing statistics

Sample	%rRNA	%Exonic	%Sense	%Antisense
CTRL2_BMP4_2_weeks_untreated_1	1.0702831391233224e-05	0,9083504	1,3	91,07
CTRL2_BMP4_2_weeks_untreated_2	7.498254031548753e-06	0,90971877	1,27	90,16
CTRL2_BMP4_2_weeks_untreated_3	3.602798417991563e-05	0,92046098	1,06	91,74
CTRL2_BMP4_3_weeks_treated_1	3.412575402404687e-05	0,91035656	1,15	91,08
CTRL2_BMP4_3_weeks_treated_2	2.9365221788994567e-05	0,9182632	0,88	91,7
CTRL2_BMP4_3_weeks_treated_3	8.864763598916725e-05	0,92032158	0,98	93,42
CTRL2_BMP4_3_weeks_untreated_1	2.3645756836494996e-05	0,91036341	1,34	90,51
CTRL2_BMP4_3_weeks_untreated_2	6.841568114778179e-05	0,91692811	0,93	90,77
CTRL2_BMP4_3_weeks_untreated_3	5.652362846828613e-05	0,914929	1,26	91,6
CTRL2_CNTF_2_weeks_untreated_1	1.3677717281994113e-05	0,89461464	1,09	90,23
CTRL2_CNTF_2_weeks_untreated_2	9.502154566037075e-06	0,91487257	1,14	90,76
CTRL2_CNTF_2_weeks_untreated_3	9.525412817103375e-06	0,91915607	1,07	90,97
CTRL2_CNTF_3_weeks_treated_1	1.6254286214639087e-05	0,92243262	0,69	93,29
CTRL2_CNTF_3_weeks_treated_2	3.0267865692853577e-05	0,92125743	0,84	92,09
CTRL2_CNTF_3_weeks_treated_3	1.864833452501371e-05	0,92318015	0,76	94,32
CTRL2_CNTF_3_weeks_untreated_1	7.788432526550377e-06	0,89587303	1,18	88,65
CTRL2_CNTF_3_weeks_untreated_2	1.964225559877943e-05	0,91908482	0,9	92,15
CTRL2_CNTF_3_weeks_untreated_3	5.8648220516638876e-05	0,92558214	0,81	91,47
CTRL2_progenitor_0_weeks_untreated_1	3.3703698785460256e-06	0,90843109	1,02	91,65
CTRL2_progenitor_0_weeks_untreated_2	1.2248234478241135e-05	0,91232669	0,94	90,34
CTRL2_progenitor_0_weeks_untreated_3	2.026570911641441e-05	0,91766338	0,85	93,12
CTRL3_BMP4_2_weeks_untreated_1	1.8582752210409086e-05	0,91282913	1,98	90,41
CTRL3_BMP4_2_weeks_untreated_2	0	0,89503774	2,42	90,45
CTRL3_BMP4_2_weeks_untreated_3	6.267368641202202e-06	0,8993392	2,48	91,69
CTRL3_BMP4_3_weeks_treated_1	0	0,90702329	1,9	91,73
CTRL3_BMP4_3_weeks_treated_2	0	0,90361078	1,96	91,42
CTRL3_BMP4_3_weeks_treated_3	3.571096586985146e-06	0,90903192	1,93	91,42
CTRL3_BMP4_3_weeks_untreated_1	1.0904201465153934e-05	0,88758165	2,29	88,74
CTRL3_BMP4_3_weeks_untreated_2	0	0,89868903	2,19	90,51
CTRL3_BMP4_3_weeks_untreated_3	6.627272831501655e-06	0,87752893	2,32	89,03
CTRL3_CNTF_2_weeks_untreated_1	1.358954702914156e-05	0,90195388	1,85	92,09
CTRL3_CNTF_2_weeks_untreated_2	4.003537044908435e-06	0,89327581	1,78	91,18
CTRL3_CNTF_2_weeks_untreated_3	3.315715719950804e-06	0,90856993	1,92	91,91
CTRL3_CNTF_3_weeks_treated_1	8.006105135532151e-06	0,92146936	1,03	95,63
CTRL3_CNTF_3_weeks_treated_2	3.6379577232932977e-06	0,91029995	1,17	94,74
CTRL3_CNTF_3_weeks_treated_3	0	0,92149999	1,04	94,6
CTRL3_CNTF_3_weeks_untreated_1	3.7903913579077043e-06	0,88722491	2,12	89,74
CTRL3_CNTF_3_weeks_untreated_2	0	0,89913839	1,89	90,48
CTRL3_CNTF_3_weeks_untreated_3	1.0311228625510474e-05	0,90097132	2,05	91,39
CTRL3_progenitor_0_weeks_untreated_1	9.432035815326398e-06	0,91558161	1,53	93,48
CTRL3_progenitor_0_weeks_untreated_2	1.1648714153775956e-05	0,90272594	2,1	91,8
CTRL3_progenitor_0_weeks_untreated_3	0	0,90587083	1,85	93,26

Table 5 - RNA sequencing statistics

1351

1352

1353 Differential expression analysis

1354 Differential gene expression analysis was carried out in R environment v4.2.2 with the
1355 DESeq2 (v1.38.3) package. The gene expression response was modelled as: ~
1356 cell_line_batch + target + treatment + target:treatment, where "target" refers to cell type and
1357 "cell_line_batch" to the 3 individual batch of experiments per sample group. The differential
1358 expression using DESeq2 was achieved by use of negative binomial generalized linear
1359 models along with Wald test *p* value for significance, IHW[78] (v1.26.0) for multiple-testing
1360 correction, and ashr[79] (v2.2-63) for effect-size shrinkage to ensure reported fold-changes are
1361 more robust.

1362 Additional PCA plots were produced using data after regressing out the effect of all
1363 experimental factors from the above model except the one of interest thus masking variance
1364 contribution from other factors. The log2 fold changes for differential comparison of interest
1365 were visualized as volcano plots to represent log fold-change versus p-value between two
1366 experimental factors. Gene signatures were considered significant if FDR q-value <0.05.

1367 Functional enrichment and pathway analysis

1368 Gene Set Enrichment[80] was performed using clusterProfiler package[81] (version 4.6.2) for
1369 each pairwise comparison using gene lists ranked by the regularized log2 fold changes.
1370 Gene sets enrichments were quantified from MSigDB (version 7.5.1) for gene ontology (GO)
1371 Biological Process. Additionally, Venn diagrams were generated using the ggVennDiagram[82]
1372 (version 1.2.2) package across selected differential comparisons to illustrate set overlaps
1373 using significant gene signatures showing either upregulated or downregulated
1374 characteristics separately.

1375 Single-cell RNA-seq reference data

1376 The Human Brain Cell Atlas v1.0 single-cell RNA sequencing (scRNA-seq) dataset from
1377 three pathology-free post-mortem donors across 10 brain regions was downloaded from the
1378 Chan Zuckerberg CELLxGENE explorer
1379 (https://cellxgene.cziscience.com/collections/283d65eb-dd53-496d-adb7-7570c7caa443)[41].
1380 For the ~2.5 million neuronal and 888k non-neuronal nuclei, the integrated Seurat object
1381 was randomly down-sampled to 50k cells and gene-cell expression counts were log
1382 normalized with Seurat *NormaliseData*[83].

1383 Data for cell type markers in the scRNA-seq dataset enriched for vascular cell types,
1384 containing glial and neuronal cell populations, in entorhinal and somatosensory cortex
1385 samples from 6 Alzheimer's disease (AD) and 6 non-disease control (NDC) cases, and
1386 prefrontal cortex samples 10 AD and 10 NDC cases were accessed from GEO[42].

1387 The snRNA-seq dataset containing grey and white matter astrocytes was downloaded from
1388 zenodo (10.5281/zenodo.8338962), and processed into a Seurat object using a script
1389 provided by the authors of the publication. The dataset was subset to 9054 astrocyte cells
1390 from 26 control samples before downstream analysis[43].

1391 Comparative analysis

1392 Gene expression levels in the differentiated astrocytes from bulk RNA-seq data were
1393 correlated with Human Brain Cell Atlas[41] pseudo-bulk counts from scRNA-seq data in the
1394 form of gene effect sizes, which were derived by comparison with progenitor cells. The
1395 down-sampled raw gene-cell count matrix used to derive pseudo-bulk counts by donor and
1396 cell type (neuronal and non-neuronal, annotation level:'cell_type') or subtype (astrocyte,
1397 annotation level: 'cluster_id') with Seurat *AggregateExpression*[83], which were compared
1398 against progenitor cell gene expression with DESeq2 v1.38.3) differential analysis. The
1399 degree of similarity was quantified by Pearson's correlation coefficient (*R*; $p<0.05$) of the
1400 gene $\log_2$(FoldChange) effect sizes. This was repeated at several adjusted *p*-value
1401 thresholds of differentiated astrocyte differentially expressed genes (n=8817 and 9005, 7472
1402 and 7713, 5338 and 5538, 4654 and 4852 for CNTF and BMP4 astrocytes respectively, at
1403 p.adj<0.1, 0.05, 0.01, 0.005) to ensure the robustness of the associations. Hierarchical
1404 clustering of the cell type correlation coefficients was carried out with the ComplexHeatmap
1405 R package using Euclidean distance (v2.14.0). These steps were replicated for the
1406 grey/white matter astrocyte comparisons, with pseudo-bulks derived for each individual and
1407 matter-type (annotation level:'matter') or subtype (annotation level:'fine_type') at the same
1408 adjusted p-value thresholds of differentiated astrocyte differentially expressed genes.

1409 As a complimentary approach, we tested the enrichment of cell type marker genes in the
1410 single cell human reference datasets. The derive the marker gene lists for the down-sampled
1411 Human Brain Cell Atlas dataset[41], we used Seurat *FindAllMarkers*[83] with $\log_2$ FoldChange
1412 threshold=0.1, minimum proportion of cells expressing gene=0.2, and considering only
1413 upregulated genes. This was repeated using the full astrocyte dataset for astrocyte subtype
1414 comparisons. Cell type marker gene list for a human post-mortem snRNA-seq dataset
1415 enriched in vascular cell types were downloaded from a previous publication[42]. The
1416 intersection between the top reference cell type markers and differentiated astrocyte
1417 upregulated genes (Human Brain Cell Atlas cell type Nmarker= 50 and astroDEG=1000;

1418 Human Brain Cell Atlas astrocyte cluster Nmarker=20 and astroDEG=500; Vascular-
1419 enriched cell type Nmarker=100 and astroDEG=1000) was quantified and tested for
1420 enrichment with a hypergeometric test using *phyper* in R.

1421 **Mouse astrocyte isolation and bulk RNA sequencing**

1422

1423 Primary mouse cortical astrocytes were isolated from C57BL/6N mice according to
1424 previously established protocol[44]. Briefly, cortices were isolated from postnatal day 2-3
1425 mouse pups and dissociated with Papain (Worthington) in DMEM (Gibco) with DNase
1426 (Worthington, 12.5U/ml) and filtered through a 70µm filter. Following dissociation, cells were
1427 plated in 10 cm dishes coated with poly-D-lysine (Sigma-Aldrich, 2µg/ml) and laminin (Gibco,
1428 6µg/ml) in survival medium containing 50% DMEM/F-12 (Gibco) and 50% neurobasal
1429 (Gibco) with B27 (Gibco, 1X), N2 (Gibco, 1X), L-glutamine (VWR, 200µg/ml), non-essential
1430 amino acids (Gibco, 1X), penicillin-streptomycin (VWR, 1X), glucose (Alfa Aesar, 3mg/ml),
1431 and N-acetyl-l-cysteine (Sigma-Aldrich, 5µg/ml). Survival medium was supplemented with
1432 Fgf2 (Stemcell Technologies, 20ng/ml), CNTF (Stemcell Technologies, 10ng/ml), BMP4
1433 (Stemcell Technologies, 10ng/ml) and hbEGF (Sigma-Aldrich, 5ng/ml). After 24 hours in
1434 survival medium, B-27 was removed from the medium. From this point, media was changed
1435 every 48 hours while the cells grew, and once they were confluent (5 days), they were
1436 cryopreserved in Cryostor media (Stemcell Technologies) and stored at -80C.

1437

1438 Cells were thawed on day 0 of an experiment, and they were plated on poly-D-lysine
1439 (Sigma-Aldrich, 2µg/ml) and laminin (Gibco, 6µg/ml) coated plates in growth media
1440 containing 50% DMEM/F-12 (Gibco) and 50% neurobasal (Gibco) with N2 (Gibco, 1X), L-
1441 glutamine (VWR, 200µg/ml), non-essential amino acids (Gibco, 1X), Pen-Strep (VWR, 1X),
1442 glucose (Alfa Aesar, 3mg/ml), and N-acetyl-l-cysteine (Sigma-Aldrich, 5µg/ml). Growth media
1443 was supplemented with either BMP4 (Stemcell Technologies, 10ng/ml) or CNTF (Stemcell
1444 technologies, 20ng/ml). Media was changed every 48 hours. On Day 7, cells were imaged
1445 on the Olympus CKX53 microscope with the Olympus DP23M camera. Post-processing was
1446 done in FIJI. Then, cells were lysed to isolate RNA according to manufacturer instructions
1447 with the RNeasy Plus Mini Kit (Qiagen).

1448

1449 Cell lysates were then sequenced on the NovaSeq X+. Raw sequencing FastQ data quality
1450 was assessed using *fastqc*. Adapter and quality trimming was performed using *trimgalore.*
1451 Files were then aligned to the mouse genome (GRCm38 - mm10) using *salmon* (V1.10.0).
1452 Differential gene expression testing between conditions was then generated using

1453 DESeq2(V1.42.1)[77]. Volcano plots were generated using *EnhancedVolcano* (V1.20.0) and
1454 Gene set enrichment go term analysis was performed using clusterProfiler(V4.10.1)[81].

1455 Multivariate analysis of astrocyte morphometric parameters

1456 We performed singular value decomposition (SVD) of matrix of 52 morphological
1457 measurements across the 5,376 cells at distinct stages of astrocyte differentiation in four
1458 different culture conditions (basal, CNTF, BMP4, CNTF+BMP4). We next quantified the
1459 association between individual left singular vectors and culture conditions using linear mixed
1460 modelling, accounting for the idiosyncratic differences that may arise from the different cell
1461 lines and experiments using R and lme4 37. As fixed effects, we entered the culture condition
1462 variable into the model. As random effects, we had intercepts for either cell lines and
1463 experiments. Visual inspection of residual plots did not reveal any obvious deviations from
1464 homoscedasticity or normality. P-values were obtained by likelihood ratio tests of the full model
1465 with the effect in question against the model without the effect in question. We iteratively fitted
1466 a linear mixed model to the each left singular vectors.

1467 To visualize the right singular vectors, we plotted the average singular vectors per group on
1468 the vertical axis as a function of the time corresponding to each sample on the horizontal axis
1469 and coloring all samples corresponding to culture conditions. Next, we identified morphological
1470 features whose profiles correlated (Pearson correlation between individual morphological
1471 measurements profile and right singular vectors) and contributed (projection of each individual
1472 morphological measurements profile onto right singular vectors) most strongly (either
1473 positively or negatively) with the profile of the singular vectors. In order to identify
1474 representative measurements for each singular vector, features were ranked according to both
1475 projection and correlation scores. The highest (most positive scores in both projection and
1476 correlation) and lowest (most negative scores in both correlation and projection) motifs were
1477 selected for each singular vector using K-mean clustering.

1478 Statistical analysis and plotting

1479 For every experiment, Gaussian distribution of the data was tested using Shapiro-Wilks or
1480 Kolmogorov-Smirnov tests, and parametric or non-parametric statistical test used in
1481 accordance.

1482 Statistical tests are specified in figure legends but, briefly, unpaired T-test was used for
1483 comparison between two groups with normal distribution, while Mann-Whitney U-test was
1484 used in case of non-normal distribution. For comparison of 3 or more groups, one-way
1485 ANOVA, Kruskal-Wallis or two-way ANOVA were used based on the normality of the data.
1486 Tukey, Dunn's or Šídák's tests were used for multiple comparisons.

Plotting was performed either on GraphPad Prism or using custom R scripts. Statistical significance was represented as *, **, ***, **** for p-values of <0.05, <0.01, <0.001, <0.0001, respectively.

Figures were assembled using Adobe Illustration software.

Data availability

For RNA sequencing, raw and transformed gene expression counts, differential analysis, and gene set enrichment analysis output tables, as well as Human Brain Cell Atlas reference dataset cell type marker gene lists can be found on the GitHub repository: https://github.com/Marzi-lab/AstroShape_RNA.

Raw RNA sequencing data can be accessed on GEO, under accession number GSE279716.

R scripts used to perform comparative analysis and reproduce the figures in this manuscript are available on the GitHub repository: https://github.com/Marzi-lab/AstroShape_RNA.

For multivariate analysis of astrocyte morphometric parameters, we provide the raw images and complete source code (which is not a software but rather a compilation of R to readily reproduce figures, tables, and other results that involve computation to facilitate the development and evaluation of additional profiling methods. We also provide the >60 measurements of each of the ~500 cells whose origins are annotated. The raw images, metadata and single-cell measurements provided as comma-delimited files have been deposited on Github together with the statistical analysis in the following repository: https://github.com/RLuisier/AstroShape.

Bibliography

1. Pitaval, A., Tseng, Q., Bornens, M. & Théry, M. Cell shape and contractility regulate ciliogenesis in cell cycle–arrested cells. *J. Cell Biol.* **191**, 303–312 (2010).

2. Esfahani, P. H. & Knöll, R. Cell shape: effects on gene expression and signaling. *Biophys. Rev.* **12**, 895–901 (2020).

3. Ron, A. *et al.* Cell shape information is transduced through tension-independent mechanisms. *Nat. Commun.* **8**, 2145 (2017).

4. Sero, J. E. & Bakal, C. Multiparametric Analysis of Cell Shape Demonstrates that β-PIX Directly Couples YAP Activation to Extracellular Matrix Adhesion. *Cell Syst.* **4**, 84-96.e6 (2017).

5. Rincel, M. *et al.* Maternal high-fat diet and early life stress differentially modulate spine density and dendritic morphology in the medial prefrontal cortex of juvenile and adult rats. *Brain Struct. Funct.* **223**, 883–895 (2018).

6. Nurmagambetova, A., Mustyatsa, V., Saidova, A. & Vorobjev, I. Morphological and cytoskeleton changes in cells after EMT. *Sci. Rep.* **13**, 22164 (2023).

7. Gallo, V. & Deneen, B. Glial Development: The Crossroads of Regeneration and Repair in the CNS. *Neuron* **83**, 283–308 (2014).

8. Rodnight, R. B. & Gottfried, C. Morphological plasticity of rodent astroglia. *J. Neurochem.* **124**, 263–275 (2013).

9. Khakh, B. S. & Sofroniew, M. V. Diversity of astrocyte functions and phenotypes in neural circuits. *Nat. Neurosci.* **18**, 942–952 (2015).

10. Clarke, B. E., Taha, D. M., Tyzack, G. E. & Patani, R. Regionally encoded functional heterogeneity of astrocytes in health and disease: A perspective. *Glia* **69**, 20–27 (2021).

11. Clarke, L. E. & Barres, B. A. Emerging roles of astrocytes in neural circuit development. *Nat. Rev. Neurosci.* **14**, 311–321 (2013).

12. Oberheim, N. A. *et al.* Uniquely Hominid Features of Adult Human Astrocytes. *J. Neurosci.* **29**, 3276–3287 (2009).

13. Schiweck, J., Eickholt, B. J. & Murk, K. Important Shapeshifter: Mechanisms Allowing Astrocytes to Respond to the Changing Nervous System During Development, Injury and Disease. *Front. Cell. Neurosci.* **12**, 261 (2018).

14. Caiazzo, M. *et al.* Direct Conversion of Fibroblasts into Functional Astrocytes by Defined Transcription Factors. *Stem Cell Rep.* **4**, 25–36 (2015).

15. Leng, K. *et al.* CRISPRi screens in human iPSC-derived astrocytes elucidate regulators of distinct inflammatory reactive states. *Nat. Neurosci.* **25**, 1528–1542 (2022).

16. Frazel, P. W. *et al.* Longitudinal scRNA-seq analysis in mouse and human informs optimization of rapid mouse astrocyte differentiation protocols. *Nat. Neurosci.* **26**, 1726–1738 (2023).

17. Wang, M. *et al.* Morphological diversification and functional maturation of human astrocytes in glia-enriched cortical organoid transplanted in mouse brain. *Nat. Biotechnol.* 1–11 (2024) doi:10.1038/s41587-024-02157-8.

18. Bilican, B. *et al.* Mutant induced pluripotent stem cell lines recapitulate aspects of TDP-43 proteinopathies and reveal cell-specific vulnerability. *Proc. Natl. Acad. Sci.* **109**, 5803–5808 (2012).

19. Serio, A. *et al.* Astrocyte pathology and the absence of non-cell autonomy in an induced pluripotent stem cell model of TDP-43 proteinopathy. *Proc. Natl. Acad. Sci.* **110**, 4697–4702 (2013).

20. Hall, C. E. *et al.* Progressive Motor Neuron Pathology and the Role of Astrocytes in a Human Stem Cell Model of VCP-Related ALS. *Cell Rep.* **19**, 1739–1749 (2017).

21. Perriot, S. *et al.* Human Induced Pluripotent Stem Cell-Derived Astrocytes Are Differentially Activated by Multiple Sclerosis-Associated Cytokines. *Stem Cell Rep.* **11**, 1199–1210 (2018).

22. Barbar, L. *et al.* CD49f Is a Novel Marker of Functional and Reactive Human iPSC-Derived Astrocytes. *Neuron* **107**, 436-453.e12 (2020).

23. Gilyarov, A. V. Nestin in central nervous system cells. *Neurosci. Behav. Physiol.* **38**, 165–169 (2008).

24. Deneen, B. *et al.* The Transcription Factor NFIA Controls the Onset of Gliogenesis in the Developing Spinal Cord. *Neuron* **52**, 953–968 (2006).

25. Bonaguidi, M. A. *et al.* LIF and BMP signaling generate separate and discrete types of GFAP-expressing cells. *Development* **132**, 5503–5514 (2005).

26. Davies, S. J. A. *et al.* Transplantation of Specific Human Astrocytes Promotes Functional Recovery after Spinal Cord Injury. *PLoS ONE* **6**, e17328 (2011).

27. Cahoy, J. D. *et al.* A Transcriptome Database for Astrocytes, Neurons, and Oligodendrocytes: A New Resource for Understanding Brain Development and Function. *J. Neurosci.* **28**, 264–278 (2008).

28. Du, J. *et al.* S100B is selectively expressed by gray matter protoplasmic astrocytes and myelinating oligodendrocytes in the developing CNS. *Mol. Brain* **14**, 154 (2021).

29. Luisier, R. *et al.* Computational modeling identifies key gene regulatory interactions underlying phenobarbital-mediated tumor promotion. *Nucleic Acids Res.* **42**, 4180–4195 (2014).

30. Sakuragi, S., Niwa, F., Oda, Y., Mikoshiba, K. & Bannai, H. Astroglial Ca2+ signaling is generated by the coordination of IP3R and store-operated Ca2+ channels. *Biochem. Biophys. Res. Commun.* **486**, 879–885 (2017).

31. Perea, G. *et al.* Activity-dependent switch of GABAergic inhibition into glutamatergic excitation in astrocyte-neuron networks. *eLife* **5**, e20362 (2016).

32. Jackson, J. G. & Robinson, M. B. Reciprocal Regulation of Mitochondrial Dynamics and Calcium Signaling in Astrocyte Processes. *J. Neurosci.* **35**, 15199–15213 (2015).

33. Derouiche, A., Haseleu, J. & Korf, H.-W. Fine Astrocyte Processes Contain Very Small Mitochondria: Glial Oxidative Capability May Fuel Transmitter Metabolism. *Neurochem. Res.* **40**, 2402–2413 (2015).

1583 34. Rothstein, J. D. *et al.* Knockout of Glutamate Transporters Reveals a Major Role for Astroglial
1584 Transport in Excitotoxicity and Clearance of Glutamate. *Neuron* **16**, 675–686 (1996).

1585 35. Blitzblau, R., Gupta, S., Djali, S., Robinson, M. B. & Rosenberg, P. A. The Glutamate Transport
1586 Inhibitor L-trans-pyrrolidine-2,4-dicarboxylate Indirectly Evokes NMDA Receptor Mediated
1587 Neurotoxicity in Rat Cortical Cultures. *Eur. J. Neurosci.* **8**, 1840–1852 (1996).

1588 36. Stogsdill, J. A. *et al.* Astrocytic neuroligins control astrocyte morphogenesis and synaptogenesis.
1589 *Nature* **551**, 192–197 (2017).

1590 37. Araque, A. *et al.* Gliotransmitters Travel in Time and Space. *Neuron* **81**, 728–739 (2014).

1591 38. Shi, Y., Kirwan, P. & Livesey, F. J. Directed differentiation of human pluripotent stem cells to
1592 cerebral cortex neurons and neural networks. *Nat. Protoc.* **7**, 1836–1846 (2012).

1593 39. Allen, N. J. *et al.* Astrocyte glypicans 4 and 6 promote formation of excitatory synapses via
1594 GluA1 AMPA receptors. *Nature* **486**, 410–414 (2012).

1595 40. Diniz, L. P. *et al.* Astrocyte transforming growth factor beta 1 promotes inhibitory synapse
1596 formation via CaM kinase II signaling. *Glia* **62**, 1917–1931 (2014).

1597 41. Siletti, K. *et al.* Transcriptomic diversity of cell types across the adult human brain. *Science* **382**,
1598 eadd7046 (2023).

1599 42. Tsartsalis, S. *et al.* A single nuclear transcriptomic characterisation of mechanisms responsible for
1600 impaired angiogenesis and blood-brain barrier function in Alzheimer's disease. *Nat. Commun.* **15**,
1601 2243 (2024).

1602 43. Macnair, W. *et al.* Single nuclei RNAseq stratifies multiple sclerosis patients into distinct white
1603 matter glial responses. *bioRxiv* 2022.04.06.487263 (2023) doi:10.1101/2022.04.06.487263.

1604 44. Clayton, B. L. L. *et al.* A phenotypic screening platform for identifying chemical modulators of
1605 astrocyte reactivity. *Nat. Neurosci.* **27**, 656–665 (2024).

1606 45. Foo, L. C. *et al.* Development of a Method for the Purification and Culture of Rodent Astrocytes.
1607 *Neuron* **71**, 799–811 (2011).

1608 46. Morton, W. M., Ayscough, K. R. & McLaughlin, P. J. Latrunculin alters the actin-monomer
1609 subunit interface to prevent polymerization. *Nat. Cell Biol.* **2**, 376–378 (2000).

1610 47. Ishizaki, T. *et al.* Pharmacological properties of Y-27632, a specific inhibitor of rho-associated
1611 kinases. *Mol. Pharmacol.* **57**, 976–83 (2000).

1612 48. Liu, F., Huang, J. & Liu, Z. Vincristine Impairs Microtubules and Causes Neurotoxicity in
1613 Cerebral Organoids. *Neuroscience* **404**, 530–540 (2019).

1614 49. Zhang, Y. *et al.* An RNA-Sequencing Transcriptome and Splicing Database of Glia, Neurons, and
1615 Vascular Cells of the Cerebral Cortex. *J. Neurosci.* **34**, 11929–11947 (2014).

1616 50. Blüml, S., Moreno-Torres, A., Shic, F., Nguy, C. -H. & Ross, B. D. Tricarboxylic acid cycle of
1617 glia in the in vivo human brain. *NMR Biomed.* **15**, 1–5 (2002).

1618 51. Goubert, E. *et al.* Inhibition of the Mitochondrial Glutamate Carrier SLC25A22 in Astrocytes
1619 Leads to Intracellular Glutamate Accumulation. *Front. Cell. Neurosci.* **11**, 149 (2017).

1620 52. Agarwal, A. *et al.* Transient Opening of the Mitochondrial Permeability Transition Pore Induces
1621 Microdomain Calcium Transients in Astrocyte Processes. *Neuron* **93**, 587-605.e7 (2017).

1622 53. Alaoui, A. A. E., Jackson, M., Fabri, M., Vivo, L. de & Bellesi, M. Characterization of
1623 Subcellular Organelles in Cortical Perisynaptic Astrocytes. *Front. Cell. Neurosci.* **14**, 573944 (2021).

1624 54. Srinivasan, R. *et al.* Ca2+ signaling in astrocytes from Ip3r2−/− mice in brain slices and during
1625 startle responses in vivo. *Nat. Neurosci.* **18**, 708–717 (2015).

1626 55. Varadi, A. *et al.* Cytoplasmic dynein regulates the subcellular distribution of mitochondria by
1627 controlling the recruitment of the fission factor dynamin-related protein-1. *J. Cell Sci.* **117**, 4389–
1628 4400 (2004).

1629 56. Gurskaya, N. G. *et al.* Engineering of a monomeric green-to-red photoactivatable fluorescent
1630 protein induced by blue light. *Nat. Biotechnol.* **24**, 461–465 (2006).

1631 57. Escartin, C. *et al.* Reactive astrocyte nomenclature, definitions, and future directions. *Nat.*
1632 *Neurosci.* **24**, 312–325 (2021).

1633 58. Matusova, Z., Hol, E. M., Pekny, M., Kubista, M. & Valihrach, L. Reactive astrogliosis in the era
1634 of single-cell transcriptomics. *Front. Cell. Neurosci.* **17**, 1173200 (2023).

1635 59. Liddelow, S. A. *et al.* Neurotoxic reactive astrocytes are induced by activated microglia. *Nature*
1636 **541**, 481–487 (2017).

1637 60. Wanner, I. B. *et al.* Glial Scar Borders Are Formed by Newly Proliferated, Elongated Astrocytes
1638 That Interact to Corral Inflammatory and Fibrotic Cells via STAT3-Dependent Mechanisms after
1639 Spinal Cord Injury. *J. Neurosci.* **33**, 12870–12886 (2013).

1640 61. Litvinchuk, A. *et al.* Complement C3aR Inactivation Attenuates Tau Pathology and Reverses an
1641 Immune Network Deregulated in Tauopathy Models and Alzheimer's Disease. *Neuron* **100**, 1337-
1642 1353.e5 (2018).

1643 62. Yun, S. P. *et al.* Block of A1 astrocyte conversion by microglia is neuroprotective in models of
1644 Parkinson's disease. *Nat. Med.* **24**, 931–938 (2018).

1645 63. Liddelow, S. A. *et al.* Neurotoxic reactive astrocytes are induced by activated microglia. *Nature*
1646 **541**, 481–487 (2017).

1647 64. Liang, C.-C., Park, A. Y. & Guan, J.-L. In vitro scratch assay: a convenient and inexpensive
1648 method for analysis of cell migration in vitro. *Nat. Protoc.* **2**, 329–333 (2007).

1649 65. Jo, J. *et al.* Regional heterogeneity of astrocyte morphogenesis dictated by the formin protein,
1650 Daam2, modifies circuit function. *Embo Rep* **22**, e53200 (2021).

1651 66. Lanjakornsiripan, D. *et al.* Layer-specific morphological and molecular differences in neocortical
1652 astrocytes and their dependence on neuronal layers. *Nat. Commun.* **9**, 1623 (2018).

1653 67. Batiuk, M. Y. *et al.* Identification of region-specific astrocyte subtypes at single cell resolution.
1654 *Nat. Commun.* **11**, 1220 (2020).

68. Kumar, M., Nguyen, N. T. P., Milanese, M. & Bonanno, G. Insights into Human-Induced Pluripotent Stem Cell-Derived Astrocytes in Neurodegenerative Disorders. *Biomolecules* **12**, 344 (2022).

69. Crompton, L. A., Cordero-Llana, O. & Caldwell, M. A. Astrocytes in a dish: Using pluripotent stem cells to model neurodegenerative and neurodevelopmental disorders. *Brain Pathol.* **27**, 530–544 (2017).

70. Voss, A. J. *et al.* Identification of ligand–receptor pairs that drive human astrocyte development. *Nat. Neurosci.* **26**, 1339–1351 (2023).

71. Du, Y., Brennan, F. H., Popovich, P. G. & Zhou, M. Microglia maintain the normal structure and function of the hippocampal astrocyte network. *Glia* **70**, 1359–1379 (2022).

72. Owens, P. *et al.* Bone Morphogenetic Proteins Stimulate Mammary Fibroblasts to Promote Mammary Carcinoma Cell Invasion. *PLoS ONE* **8**, e67533 (2013).

73. Takagishi, M., Yue, Y., Gray, R. S., Verhey, K. J. & Wallingford, J. B. Kif6 regulates cilia motility and polarity in brain ependymal cells. *Dis. Model. Mech.* **17**, dmm050137 (2024).

74. Wiese, S., Karus, M. & Faissner, A. Astrocytes as a Source for Extracellular Matrix Molecules and Cytokines. *Front. Pharmacol.* **3**, 120 (2012).

75. Shi, Y., Kirwan, P. & Livesey, F. J. Directed differentiation of human pluripotent stem cells to cerebral cortex neurons and neural networks. *Nat. Protoc.* **7**, 1836–1846 (2012).

76. Li, B. & Dewey, C. N. RSEM: accurate transcript quantification from RNA-Seq data with or without a reference genome. *BMC Bioinform.* **12**, 323 (2011).

77. Love, M. I., Huber, W. & Anders, S. Moderated estimation of fold change and dispersion for RNA-seq data with DESeq2. *Genome Biol.* **15**, 550 (2014).

78. Ignatiadis, N., Klaus, B., Zaugg, J. B. & Huber, W. Data-driven hypothesis weighting increases detection power in genome-scale multiple testing. *Nat. Methods* **13**, 577–580 (2016).

79. Stephens, M. False discovery rates: a new deal. *Biostatistics* **18**, 275–294 (2017).

80. Subramanian, A. *et al.* Gene set enrichment analysis: A knowledge-based approach for interpreting genome-wide expression profiles. *Proc. Natl. Acad. Sci.* **102**, 15545–15550 (2005).

81. Yu, G., Wang, L.-G., Han, Y. & He, Q.-Y. clusterProfiler: an R Package for Comparing Biological Themes Among Gene Clusters. *OMICS: A J. Integr. Biol.* **16**, 284–287 (2012).

82. Gao, C.-H., Yu, G. & Cai, P. ggVennDiagram: An Intuitive, Easy-to-Use, and Highly Customizable R Package to Generate Venn Diagram. *Front. Genet.* **12**, 706907 (2021).

83. Hao, Y. *et al.* Dictionary learning for integrative, multimodal and scalable single-cell analysis. *Nat. Biotechnol.* **42**, 293–304 (2024).